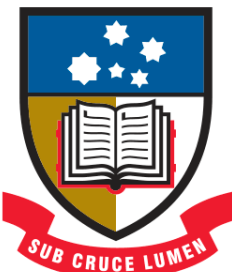


# Centre Vortices in Lattice QCD: Visualisations and Impact on the Gluon Propagator



THE UNIVERSITY  
*of*ADELAIDE

James Biddle

*Supervisors:* Prof. Derek B. Leinweber  
Dr. Waseem Kamleh

Department of Physics  
University of Adelaide

This dissertation is submitted for the degree of

*Master of Philosophy*  
January 2019



# Table of contents

<b>List of figures</b>	xiii
<b>1 Introduction</b>	1
<b>2 Lattice QCD</b>	5
2.1 QCD in the Continuum . . . . .	5
2.1.1 Quarks and Gauge Invariance . . . . .	5
2.1.2 Field Strength Tensor . . . . .	8
2.1.3 Pure Gauge Action . . . . .	10
2.2 Lattice Discretisation . . . . .	11
2.3 Gauge Fixing . . . . .	15
2.3.1 Landau Gauge . . . . .	16
2.4 Lattice units . . . . .	17
<b>3 Topology of the Lattice</b>	19
3.1 Confinement . . . . .	20
3.2 Centre Vortices . . . . .	21
3.2.1 Locating Centre Vortices . . . . .	28
3.2.2 Current Evidence for Centre Vortices . . . . .	33
3.3 Further Topological Quantities . . . . .	35
3.3.1 Topological Charge . . . . .	36
3.3.2 Instantons . . . . .	37
<b>4 Lattice Configurations and the Gluon Propagator</b>	39
4.1 Lattice Definition of the Gluon Propagator . . . . .	39
4.2 Momentum Variables . . . . .	41
4.3 Lattice Parameters and Data Cuts . . . . .	44

<b>5 Smoothing</b>	<b>49</b>
5.1 Smoothing Methods . . . . .	50
5.1.1 Cooling . . . . .	50
5.1.2 Over-Improved Smearing . . . . .	53
5.2 Results from the Gluon Propagator . . . . .	56
<b>6 Gluon Propagator on Vortex-Modified Backgrounds</b>	<b>59</b>
6.1 Preliminary Results . . . . .	59
6.1.1 Partitioning . . . . .	61
6.1.2 Renormalisation . . . . .	64
6.2 Impact of Cooling . . . . .	65
6.3 Summary . . . . .	70
<b>7 Centre Vortex Visualisations</b>	<b>73</b>
7.1 Space-Oriented Vortices . . . . .	73
7.2 Time-Oriented Vortices . . . . .	76
7.3 Topological Charge . . . . .	81
7.4 Summary . . . . .	85
<b>8 Conclusion</b>	<b>87</b>
<b>References</b>	<b>89</b>
<b>Appendix A Gell-Mann matrices</b>	<b>97</b>
<b>Appendix B Taylor expansion of <math>P_{\mu\nu}</math></b>	<b>99</b>
<b>Appendix C Wilson line gauge transformation</b>	<b>101</b>
<b>Appendix D Properties of the adjoint representation</b>	<b>103</b>
<b>Appendix E Evaluation of <math>\text{Re Tr}(F_1(U)^\dagger U)</math></b>	<b>105</b>

I would like to dedicate this thesis to the students of rooms 119 and 123, whose discussions and distractions were invaluable throughout the last two years.



## **Declaration**

I certify that this work contains no material which has been accepted for the award of any other degree or diploma in my name, in any university or other tertiary institution and, to the best of my knowledge and belief, contains no material previously published or written by another person, except where due reference has been made in the text. In addition, I certify that no part of this work will, in the future, be used in a submission in my name, for any other degree or diploma in any university or other tertiary institution without the prior approval of the University of Adelaide and where applicable, any partner institution responsible for the joint-award of this degree.

I give permission for the digital version of my thesis to be made available on the web, via the University's digital research repository, the Library Search and also through web search engines, unless permission has been granted by the University to restrict access for a period of time.

I acknowledge the support I have received for my research through the provision of an Australian Government Research Training Program Scholarship.

James Biddle  
January 2019



## **Acknowledgements**

I would like to acknowledge first and foremost my supervisors Prof. Derek Leinweber and Dr. Waseem Kamleh for their support and



## Abstract

Understanding the structure of the quantum chromodynamic (QCD) vacuum is essential to explaining the properties of the strong nuclear force. In this work, we explore the centre vortex model for confinement, which has shown significant promise in recent years as an explanation for the distinctive long range properties of QCD. Specifically, we investigate the behaviour of the gluon propagator on original, vortex-only and vortex-removed gauge field configurations. We also present novel visualisation techniques that allow for close inspection of the properties of the vortex vacuum. This work further reinforces the significance of centre vortices in a fundamental understanding of QCD vacuum structure.



# List of figures

2.1	An example of a 2D lattice with lattice spacing $a$ . If we have a position $x$ then we can define $x + a\hat{\mu}$ to represent the next lattice site in the $\hat{\mu}$ direction. . . . .	12
3.1	A single centre vortex (dashed line) intersecting a Wilson loop (solid line) in 3 dimensions. The Wilson loop will acquire a centre phase corresponding to the phase of the vortex. . . . .	22
3.2	A plot of the vortex phase distribution of 100 Monte-Carlo generated configurations, as a percentage of the total number of vortices. The method by which vortices are identified will be detailed in Sec. 3.2.1. . . . .	26
3.3	An example of two Wilson loops (dashed lines) lying in a plane, pierced by vortices of finite cross-section (solid lines). <b>Left:</b> The majority of vortices contributing to the phase are fully contained within the large loop, with only a few overlapping at the perimeter. <b>Right:</b> For a small loop, the contribution from overlapping vortices is significant as there are few vortices fully inside the loop. . . . .	27
3.4	A $1 \times 1$ vortex (blue) created by multiplying the centre link (cyan) by a centre phase. Note that there are two more plaquettes in the time direction that have been suppressed, which serve to make the vortex a cube in 4D. . . . .	30
3.5	An example of a $2 \times 1$ vortex, arising from a centre transformation split across two links (cyan). Each $1 \times 1$ plaquette individually will not acquire a centre phase, but the the $2 \times 1$ loop will. . . . .	33
3.6	The four plaquettes that compose the clover combination $C_{\mu\nu}$ . . . . .	36

---

4.1	The scalar gluon propagator is plotted with no tree-level momentum correction (blue crosses) and the Lüscher and Weisz correction (red dots) presented in Eq. 4.26. It is clear that the corrected momentum has improved tree-level behaviour, free from the fanning effect present in the uncorrected case. . . . .	45
4.2	The untouched gluon propagator with all data cuts and correct momentum variables utilised. We observe a substantially cleaner signal when compared to the untouched propagator shown in Fig. 4.1. . . . .	47
5.1	An example $1 \times 1$ staple, with the dashed link indicating the link the staple is relative to. The origin of the name staple is apparent from the shape of the 3 solid links. . . . .	50
5.2	Comparison of the gluon propagator on the untouched configurations after cooling. For clarity we have selected a sample of sweeps between 1 and 8. . . . .	56
5.3	The gluon propagator after cooling or improved smearing. We see that the shape of the plot changes minimally between the smoothing routines. However cooling requires fewer sweeps to produce the same effect when compared to smearing. . . . .	57
6.1	The gluon propagator calculated from the original untouched (red dots), shown with the vortex removed (blue triangles) and vortex only (green open circles) results. Here, the renormalisation factor for the vortex removed and vortex only propagators is chosen to be the same as for the untouched propagator. . . . .	60
6.2	The gluon propagator from the original untouched ensemble as in Fig. 6.1, now shown with the independently renormalised sum (cyan triangles) of the vortex removed and vortex only propagators. The two vortex modified propagators are also shown, but here their renormalisation factor is chosen to be the same as for the summed propagator. . . . .	61
6.3	Calculation of the cross-terms arising from Eq. 6.2 . . . . .	62
6.4	The gluon propagator calculated on the three ensembles after 10 sweeps of cooling. We now observe an improved agreement between the untouched and vortex only propagators. . . . .	66
6.5	The vortex only propagator after different sweeps of cooling. A trend similar to Fig. 5.2 is observed, with enhancement in the infrared and suppression in the UV region. . . . .	67

---

6.6	The average action calculated on the untouched and vortex-only configurations as a function of cooling sweeps, $n$ . The vortex only configurations are initially rougher than the untouched, as evidenced by the higher average action. . . . .	68
6.7	Comparison of the gluon propagator on the untouched and vortex only configurations after tuning the number of cooling sweeps to best match the average plaquette action. This procedure gives a much better agreement in the shape of the gluon propagator from the two configurations. . . . .	69
6.8	The topological charge at the instanton centre, $q(x_0)$ , is plotted against the instanton radius $\rho$ for the vortex modified configurations under 10 and 40 sweeps of cooling. The solid line represents the theoretical distribution. These plots are acquired from Trewartha <i>et al.</i> [39]. . . . .	71
7.1	An example of the plotting convention for vortices located within a 3D time slice. <b>Left:</b> A +1 vortex in the $+\hat{z}$ direction. <b>Right:</b> A -1 vortex in the $-\hat{z}$ direction. . . . .	74
7.2	The $t = 1$ slice with all space-oriented vortices plotted. . . . .	75
7.3	The $t = 2$ slice with all space-oriented vortices plotted. . . . .	75
7.4	<b>Left:</b> Vortices form continuous lines. Note that because of the lattice periodicity, these lines may wrap around to the opposite edge of the lattice. <b>Middle:</b> Vortices must form closed loops to conserve the vortex flux. <b>Right:</b> $SU(3)$ vortices are capable of forming monopoles or branching points where three vortices emerge or converge at a single point. . . . .	76
7.5	<b>Left:</b> A vortex branching point. <b>Right:</b> A vortex monopole. Note that for both figures, the vortex charge is conserved at the vertex. By changing the orientation of the plaquette containing the left-most vortex, these two diagrams can be interchanged. . . . .	77
7.6	<b>Left:</b> A +1 vortex in the forward $x - t$ plane (shaded blue) will be plotted as a cyan arrow in the $+\hat{x}$ direction. <b>Right:</b> A -1 vortex in the forward $x - t$ plane (shaded red) will be plotted as an orange arrow in the $+\hat{x}$ direction. . . . .	77
7.7	The $t = 1$ slice with all space-oriented and time-oriented vortices plotted. . . . .	78
7.8	The $t = 2$ slice with all space-oriented and time-oriented vortices plotted. . . . .	78
7.9	As we step through time we observe the time-oriented arrows change direction, however the phase (colour) of the vortex remains the same. . . . .	79

7.10 An example of time-oriented vortices predicting the motion of the space-oriented vortices. We observe the $-1$ (red) vortex line with no associated time-oriented vortices remain stationary as we transition from $t = 1$ to $t = 2$ . . . . .	80
7.11 A second example of time-oriented vortices predicting the motion of the space-oriented vortices. Here we see the $+1$ (blue) vortex line transition one lattice spacing down as we step from $t = 1$ to $t = 2$ . . . . .	80
7.12 A demonstration of how space-oriented vortices can transition multiple lattice spacings in a single time step. . . . .	81
7.13 The signature of a singular point, in which the vortex surface spans all four directions. The colour and orientation of the vortices is irrelevant, so long as they are parallel. . . . .	82
7.14 Topological charge density overlaying the $t = 1$ slice. . . . .	83
7.15 Topological charge density overlaying the $t = 2$ slice. . . . .	83
7.16 A collection of singular points shown with (left) and without (right) topological charge overlaid. . . . .	84
7.17 The correlation measure for each configuration is shown. The dashed line indicates the average value across all 100 configurations, with the one standard deviation region shown in green. . . . .	85
7.18 The vortex structure and topological charge after eight sweeps of cooling, for $t = 1$ . . . . .	86
7.19 The correlation measure for each configuration after eight sweeps of cooling is shown. The dashed line indicates the average value across all 100 configurations, with the one standard deviation region shown in green.	86

# Chapter 1

## Introduction

The standard model of particle physics is one of the great accomplishments of modern physics, unifying three of the four forces of nature into one coherent theory. However, despite the remarkable power of the standard model, there are still unsolved questions that exist within its framework. In particular, the theory of the strong interaction, Quantum ChromoDynamics (QCD), is notorious for its mathematical intractability. QCD is the theory governing the behaviour of quark colour interactions, mediated by the exchange of the force-carrying gauge boson known as the gluon. This interaction is responsible for binding quarks into baryons (quark triplets) and mesons (quark/anti-quark pairs). Due to the large coupling constant and non-Abelian nature of the  $SU(3)$  gauge group, the techniques of perturbation theory that have proven so successful for performing Quantum ElectroDynamics (QED) calculations cannot be utilised when studying the low-energy behaviour of QCD. Instead, new approaches have been constructed to facilitate an understanding of this fundamental force.

First proposed in 1974 [1], the primary technique used to perform QCD calculations is known as the lattice. Rather than treat spacetime as a set of continuous axes, it is instead discretised into a finite number of points on a four-dimensional hypercube. With spacetime reduced to a finite number of points, it becomes possible to perform first-principles calculations, albeit with the introduction of systematic errors that must be accounted for. Utilising the lattice framework and the continual increase in computing power available to researchers, it has become possible over the last 40 years to simulate the behaviour of QCD. These results have proven invaluable in developing an understanding of QCD and in guiding the direction of experiments.

Experimental observations have found two key low-energy properties of the strong interaction that must somehow arise from the theory of QCD, namely

1. Confinement of quarks, in which quarks are never observed in isolation.
2. Dynamical chiral symmetry breaking, leading to dynamical mass generation that results in hadrons exhibiting a mass greater than the sum of their quark components.

Numerous theories have been proposed to explain how QCD implies the emergence of these properties, and one that has shown particular promise in recent years is the centre vortex model. This model proposes that the vacuum is percolated by topologically non-trivial sheet-like objects known as centre vortices that naturally give rise to confining behaviour. Through lattice calculations it has been possible to investigate the impact of centre vortices on QCD. The results of these calculations have been very promising, suggesting an intimate relationship between centre vortices and the properties of confinement and dynamical chiral symmetry breaking. Continuing this line of investigation, part of this research is devoted to exploring the impact of centre vortices on the gluon propagator. The gauge boson propagator is an essential building block of any gauge theory, and an understanding of its behaviour is key to a full understanding of the theory. The gluon propagator can also be compared to the well understood photon propagator, allowing for a direct comparison to the non-confining theory of QED.

We also present a new approach for studying the centre vortex model. By making use of centre vortex identification techniques and 3D visualisation software, it becomes possible to construct 3D models of centre vortices on the lattice. These models enable us to explore the properties of centre vortices in a hands-on manner, allowing for an intuitive graphical understanding of this theoretical model. They also reveal the geometrical properties of centre vortices, raising interesting questions about the link between vortex geometry and the properties of QCD.

This thesis is structured as follows: Chapter 2 will review QCD in the continuum and demonstrate how this theory can be reformulated on the lattice. Chapter 3 will describe in detail the centre vortex model, vortex identification and a brief discussion of other topological objects. Chapter 4 will detail the calculation of the gluon propagator and the data analysis techniques used in this work. Chapter 5 provides an introduction to the smoothing routines used to study topological objects on the lattice. Chapter 6 contains the results from the gluon propagator on vortex modified backgrounds and

Chapter 7 presents the visualisations of the centre vortex vacuum. Finally, Chapter 8 summarises the findings of this research.



# Chapter 2

## Lattice QCD

Currently, lattice QCD represents the only technique able to perform accurate low-energy QCD calculations. The lattice prescription allows for the explicit calculation of path integrals present in continuum QCD, at the cost of introducing finite-spacing errors that must be systematically accounted for. In this chapter we will discuss the behaviour of QCD in the continuum, and demonstrate how the transition can be made to a finite set of coordinates on a lattice. We will then briefly detail how this formulation can be used to generate simulations of the QCD vacuum. Finally, we use this framework to describe how our generated configurations can be fixed to Landau gauge, one of the two gauge choices used in this research.

### 2.1 QCD in the Continuum

#### 2.1.1 Quarks and Gauge Invariance

QCD is the gauge field theory that describes the interactions of quarks and gluons. Like all gauge theories, it has an internal symmetry group under which the Lagrangian is invariant. In the case of QCD there are three quark colours, which leads to the symmetry group being  $SU(3)$ , the group of  $3 \times 3$  unitary matrices of determinant 1<sup>1</sup>. We can observe this  $SU(3)$  symmetry by inspecting the QCD quark Lagrangian

$$\mathcal{L}_0 = \bar{\psi}(x) (i\cancel{d} - m) \psi(x). \quad (2.1)$$

---

<sup>1</sup>This description of  $SU(3)$  is only true in the fundamental representation of the group, but it is an intuitive way to think of the group as it is clearly the symmetry of the Lagrangian.

where  $\psi(x)$  and  $\bar{\psi}(x)$  contain the three quark and anti-quark fields respectively,  $m$  is the quark mass and  $\not{d} = \partial_\mu \gamma^\mu$ . If we apply an  $SU(3)$  transformation  $\Omega$  to the three colour indices of the quark and anti-quark fields such that

$$\begin{aligned}\psi(x) &\rightarrow \Omega \psi(x) \\ \bar{\psi}(x) &\rightarrow \bar{\psi}(x) \Omega^\dagger,\end{aligned}$$

we see that

$$\begin{aligned}\mathcal{L}_0 \rightarrow \mathcal{L}'_0 &= \bar{\psi}(x) \Omega^\dagger (i\not{d} - m) \Omega \psi(x) \\ &= \bar{\psi}(x) (i\not{d} - m) \psi(x) \Omega^\dagger \Omega \\ &= \bar{\psi}(x) (i\not{d} - m) \psi(x) \\ &= \mathcal{L}_0,\end{aligned}$$

where we have made use of the unitarity property,  $UU^\dagger = I$ . If this symmetry were all we required then  $\mathcal{L}_0$  would be our free Lagrangian and our theory would be pleasantly simple. However, we find that we need our gauge symmetry to be *local*; that is, we demand that our gauge transformation itself be a function of  $x$  [2]. In this case, we find that the derivative in Eq. 2.1 acting on the gauge transformation results in a loss of  $SU(3)$  symmetry. We can write an arbitrary local  $SU(3)$  gauge transformation as an exponential of the eight traceless, Hermitian group generators  $\lambda_a$ , known as the Gell-Mann matrices (see Appendix A for their values), such that

$$\Omega(x) = \exp\left(i\omega^a(x) \frac{\lambda_a}{2}\right). \quad (2.2)$$

Note that we make use of the summation convention to imply a sum over the repeated indices. In this form, the spacial dependence is encapsulated entirely in the eight parameters,  $\omega^a(x)$ . Using this form for  $\Omega(x)$ , we find that under a gauge transformation the Lagrangian is now

$$\begin{aligned}\mathcal{L}_0 \rightarrow \mathcal{L}'_0 &= \bar{\psi}(x) \Omega^\dagger(x) (i\not{d} - m) \Omega(x) \psi(x) \\ &= \bar{\psi}(x) \Omega^\dagger(x) \left[ -\frac{\lambda_a}{2} (\not{d} \omega^a(x)) + i \Omega(x) (\not{d} \psi(x)) - m \Omega(x) \psi(x) \right] \\ &= \mathcal{L}_0 - \bar{\psi}(x) \Omega^\dagger(x) \frac{\lambda_a}{2} (\not{d} \omega^a(x)) \Omega(x) \psi(x).\end{aligned} \quad (2.3)$$

It is apparent then that gauge invariance is lost under a local gauge transformation. To restore gauge invariance, we introduce the notion of the gauge-covariant derivative

$$D_\mu = \partial_\mu - igA_\mu(x), \quad (2.4)$$

where  $A_\mu(x) = A_\mu^a(x) \frac{\lambda_a}{2}$  encapsulates the eight new ‘gauge potentials’ and  $g$  is the strong coupling constant. As the gauge potentials are a linear combination of  $\lambda_a$ , they belong not to the group  $SU(3)$ , but to the Lie algebra  $\mathfrak{su}(3)$ . In the context of QCD, these gauge potentials are also known as the gluon field. For the sake of cleanliness, we will stop explicitly writing the dependence of our fields and gauge transformations on  $x$  from here on, but it should be remembered that all gauge transformations are local unless explicitly stated otherwise. Making the substitution  $\partial_\mu \rightarrow D_\mu$ , we obtain the new Lagrangian

$$\mathcal{L}_{\text{local}} = \bar{\psi} (iD - m) \psi. \quad (2.5)$$

This substitution introduces a new interaction term into the Lagrangian that gives rise to an interaction between our quark and gauge fields.

$$\mathcal{L}_{\text{int}} = g \bar{\psi} A_\mu \psi \quad (2.6)$$

To preserve the gauge invariance of the Lagrangian, we need the gauge transformation property of Eq. 2.6 to counteract the last term of Eq. 2.3. Hence we require that

$$g \bar{\psi} A_\mu \psi \rightarrow g \bar{\psi} A_\mu \psi + \bar{\psi} \Omega^\dagger \frac{\lambda_a}{2} (\partial_\mu \omega^a) \Omega \psi. \quad (2.7)$$

Making use of the transformation properties of  $\psi$  and  $\bar{\psi}$ , this implies that

$$A_\mu \rightarrow \Omega A_\mu \Omega^\dagger - \frac{i}{g} (\partial_\mu \Omega) \Omega^\dagger. \quad (2.8)$$

This transformation property can also be expressed in terms of the covariant derivative. Doing so, we find that

$$\begin{aligned} D_\mu \psi &\rightarrow \left( \partial_\mu - ig \Omega A_\mu \Omega^\dagger - (\partial_\mu \Omega) \Omega^\dagger \right) \Omega \psi \\ &= (\partial_\mu \Omega) \psi + \Omega (\partial_\mu \psi) - ig \Omega A_\mu \psi - (\partial_\mu \Omega) \psi \\ &= \Omega D_\mu \psi. \end{aligned} \quad (2.9)$$

And therefore

$$D_\mu \rightarrow \Omega D_\mu \Omega^\dagger \quad (2.10)$$

Eq. 2.9 tells us that the covariant derivative of a quark field transforms in the same way as the quark field itself. This implies that the covariant derivative can be understood as a connection between two points that may have a different underlying gauge. For example, if we consider an infinitesimal translation in the quark field

$$d\psi(x) = \psi(x + dx) - \psi(x),$$

we note that the gauge at the point  $x$  and at  $x + dx$  in general will differ, so it doesn't make sense to compare the field values through the usual understanding of the derivative, as this ignores the change in local gauge. Instead, the covariant derivative accounts for this underlying gauge structure, ‘transporting’ the field from one position to another. This is entirely analogous to the covariant derivative present in general relativity, however in this case the transport occurs over an internal gauge space, rather than an external curved space-time.

### 2.1.2 Field Strength Tensor

Using local gauge invariance as a guide, we can now seek other gauge invariant terms to insert into the Lagrangian. If we consider the commutator of the covariant derivative, we have

$$\begin{aligned} [D_\mu, D_\nu] &\rightarrow [\Omega D_\mu \Omega^\dagger, \Omega D_\nu \Omega^\dagger] \\ &= \Omega D_\mu D_\nu \Omega^\dagger - \Omega D_\nu D_\mu \Omega^\dagger \\ &= \Omega [D_\mu, D_\nu] \Omega^\dagger. \end{aligned}$$

We therefore define the gluon field strength tensor to be

$$F_{\mu\nu} = \frac{i}{g} [D_\mu, D_\nu]. \quad (2.11)$$

Expanding this definition,  $F_{\mu\nu}$  may also be written

$$F_{\mu\nu} = \partial_\mu A_\nu - \partial_\nu A_\mu - ig[A_\mu, A_\nu]. \quad (2.12)$$

To obtain a gauge invariant quantity, we take the trace of the contracted field strength tensor. This allows us to make use of the cyclic property of the trace to obtain

$$\begin{aligned}\text{Tr}(F_{\mu\nu} F^{\mu\nu}) &\rightarrow -\frac{1}{g^2} \text{Tr}(\Omega [D_\mu, D_\nu] \Omega^\dagger \Omega [D^\mu, D^\nu] \Omega^\dagger) \\ &= -\frac{1}{g^2} \text{Tr}(\Omega^\dagger \Omega [D_\mu, D_\nu] [D^\mu, D^\nu]) \\ &= \text{Tr}(F_{\mu\nu} F^{\mu\nu}).\end{aligned}$$

Thus we define the full gauge invariant QCD Lagrangian to be

$$\mathcal{L}_{\text{QCD}} = \bar{\psi}(x) (iD - m) \psi(x) - \frac{1}{2} \text{Tr}(F_{\mu\nu}(x) F^{\mu\nu}(x)). \quad (2.13)$$

This gluon term is not the only gauge invariant quantity we could construct; for example,  $\bar{\psi} \psi \bar{\psi} \psi$  is clearly gauge invariant. However, it turns out that there is a further condition that must be satisfied by each term in the Lagrangian; each term must be *renormalisable* [2]. A complete discussion of renormalisation is unnecessary for this work, but renormalisability can be quickly summarised by looking at the dimensionality of each term in the Lagrangian. The Lagrangian must have units of (Energy)<sup>4</sup>, which in natural units is (mass)<sup>4</sup>, hereafter referred to as just dimension  $D = 4$ . We therefore require that each term and its accompanying coupling constant give the same dimensionality. The fermion field has dimension  $\frac{3}{2}$ , the gauge potential has dimension 1 and  $\partial_\mu$  has dimension 1. Thus, the terms present in Eq. 2.13 have dimension

$$\begin{aligned}D[\bar{\psi}(x) \gamma^\mu \partial_\mu \psi(x)] &= \frac{3}{2} + 1 + \frac{3}{2} = 4 \\ D[\bar{\psi}(x) \gamma^\mu A_\mu \psi(x)] &= \frac{3}{2} + 1 + \frac{3}{2} = 4 \\ D[m\bar{\psi}(x) \psi(x)] &= 1 + \frac{3}{2} + \frac{3}{2} = 4 \\ D[F_{\mu\nu} F^{\mu\nu}] &= 2 + 2 = 4,\end{aligned}$$

as required. This also tells us that the coupling constant  $g$  is dimensionless. If a new gauge invariant term  $h\bar{\psi} \psi \bar{\psi} \psi$  with coupling constant  $h$  is introduced, we then require that  $h$  have dimension  $-2$ . It turns out that if the dimensionality of the coupling constant is less than 0 then the term is non-renormalisable. This means that integrals

involving this new term will diverge in such a way that they cannot be systematically be made finite through the use of a renormalisation scheme, and hence they cannot form part of any physical theory. By applying the requirements of gauge invariance and renormalisability, it is apparent that Eq. 2.13 is the full QCD Lagrangian.

### 2.1.3 Pure Gauge Action

For the purpose of this research, we are interested in the behaviour of gluons in the absence of any quarks, and as such we need to develop a description of pure gauge fields. In the continuum, a pure gauge field has the Lagrangian [3]

$$\mathcal{L}_{\text{gluon}} = \frac{1}{2} \text{Tr}(F_{\mu\nu} F^{\mu\nu}), \quad (2.14)$$

which we observe to be the last term in Eq. 2.13. This Lagrangian has the corresponding action

$$\mathcal{S} = \int d^4x \mathcal{L}_{\text{gluon}}. \quad (2.15)$$

When considering the path integral formulation of a gauge field theory, integrals such as the generating functional,

$$\mathcal{Z} = \int \mathcal{D}A_\mu \exp(i \mathcal{S}[A_\mu]), \quad (2.16)$$

and others of a similar form appear frequently. This integral closely resembles the partition function found in statistical mechanics,  $Z_{\text{classical}} = \int d^3x d^3p \exp(-\beta H(x, p))$ , with the notable exception of the factor of  $i$  in the exponential. From the statistical mechanics perspective, the  $\exp(\dots)$  term in Eq. 2.16 is a probability weighting for a given gauge potential. However, unlike the classical case, the factor of  $i$  in Eq. 2.16 results in an oscillatory weighting, rendering numerical simulations untenable. To ensure that the weight factor is purely real, it is necessary to perform a Wick rotation into Euclidean space [1, 4]

$$x_0 \rightarrow -ix_0$$

The generating functional now becomes

$$\mathcal{Z}_{\text{Eucl}} = \int \mathcal{D}A_\mu \exp(-\mathcal{S}_{\text{Eucl}}[A_\mu]). \quad (2.17)$$

The Wick rotation also has the consequence of reducing the metric  $g_{\mu\nu}$  to the identity, meaning that there is no longer any differentiation between covariant and contravariant tensor indices.

In Euclidean space, we can make use of the generating functional to write the expectation value of an arbitrary operator  $Q[A_\mu]$  as [5]

$$\langle Q \rangle = \frac{1}{Z} \int \mathcal{D}A_\mu Q[A_\mu] \exp(-S_{\text{Eucl}}[A_\mu]). \quad (2.18)$$

This definition of the expectation value, whilst potentially difficult or even impossible to calculate analytically, has an intuitive interpretation. To calculate the expectation value of some operator, we integrate over every possible configuration of  $A_\mu(x)$ , weighted by the action of that configuration. In the case where the coupling constant  $g$  of the theory is sufficiently small, as is the case for QED or high-energy QCD, it is possible to expand  $\exp(-S_{\text{Eucl}}[A_\mu])$  in terms of the coupling constant, leading to a perturbative expansion. Alternatively, if the only relevant configurations in the theory are those near the classical action satisfying  $\frac{\delta S[A_\mu]}{\delta A_\mu} = 0$ , then the action can be expanded around the classical solution. However, in the case of low-energy QCD, both of these approximations are invalid, and as such it becomes essential to sample possible configurations of  $A_\mu(x)$  and generate a representative finite subset that can be used to approximate the continuum expectation value. Obtaining this subset on which we can perform calculations is one of the key aims of lattice QCD.

## 2.2 Lattice Discretisation

With the continuum understanding developed in the previous section, we can now consider discretising spacetime into a finite lattice. The lattice is a hypercube with  $N_s$  lattice sites in the spacial directions and  $N_t$  sites in the time direction. Each lattice site is separated by a spacing  $a$ , resulting in a total lattice volume  $V = (N_s a)^3 \times N_t a$ . This discretisation is shown in two dimensions in Fig. 2.1. For labelling points on the lattice, the notation  $\hat{\mu}$  is often used.  $\hat{\mu}$  denotes the unit vector in the  $\mu$  direction; for example,  $\hat{y} = (0, 0, 1, 0)$ . We also must impose boundary conditions for the lattice; in this work we choose periodic boundary conditions such that  $x + (N + 1)a\hat{\mu} = x$ .

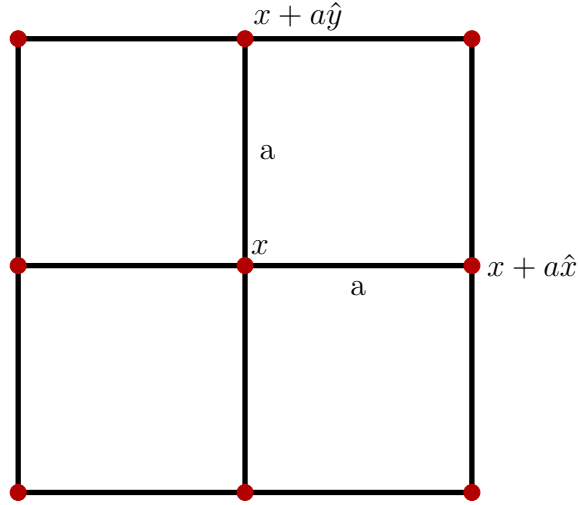


Fig. 2.1 An example of a 2D lattice with lattice spacing  $a$ . If we have a position  $x$  then we can define  $x + a\hat{\mu}$  to represent the next lattice site in the  $\hat{\mu}$  direction.

When spacetime is discretised, it becomes necessary to consider derivatives as finite differences and integrals as finite sums.

$$\partial_\mu f(x) \rightarrow \frac{f(x + a\hat{\mu}) - f(x)}{a}$$

$$\int d^4x f(x) \rightarrow a^4 \sum_x f(x)$$

For example, we can construct the lattice form of Eq. 2.12 as

$$F_{\text{Lat}}^{\mu\nu}(x) = \frac{A_\nu(x + a\hat{\mu}) - A_\nu(x)}{a} - \frac{A_\mu(x + a\hat{\nu}) - A_\mu(x)}{a} - ig[A_\mu(x), A_\nu(x)]. \quad (2.19)$$

The notation  $A_\nu(x + a\hat{\mu})$  denotes the field  $A_\nu$  located at the site one lattice spacing in the  $\hat{\mu}$  direction from  $x$ . We could continue to reformulate our lattice theory by imposing this method of discretisation, and indeed this is historically how the lattice framework was constructed [1]. However, it is useful to instead formulate our lattice theory in terms of gauge *links*. Analogous to how we introduced the covariant derivative to compensate for the fact that the quark field at infinitesimally different points in space has a different underlying gauge, we now want to have a mechanism for comparing gluon fields at some finite separation. This requires us to solve the parallel transport equation of our gauge field [2, 6]

$$\frac{dx^\mu(t)}{dt} D_\mu U(x(t), y) = 0, \quad (2.20)$$

where  $U(x(t), y)$  is an  $SU(3)$  element and  $x(t)$  is some path parametrised by  $t \in [0, 1]$  satisfying  $x(0) = y$ . We further require that  $U(y, y) = I$ , as the parallel transport from  $y \rightarrow y$  is trivial. We can now make use of the explicit parametrisation of the path between two adjacent lattice sites,  $x(t) = x_\mu + a t \hat{\nu}$ , where  $x_\mu$  is a fixed position and  $\nu$  is the direction we are transporting the field. Substituting this into Eq. 2.20 we have

$$\begin{aligned} a \delta_\mu^\nu (\partial_\mu - ig A_\mu) U(x_\mu + a t \hat{\nu}) &= 0 \\ a \partial_\nu U(x_\mu + a t \hat{\nu}) &= i a g A_\nu U(x_\mu + a t \hat{\nu}) \\ \frac{\partial}{\partial t} U(x_\mu + a t \hat{\nu}) &= i a g A_\nu U(x_\mu + a t \hat{\nu}). \end{aligned}$$

For a non-Abelian field, this is precisely the differential equation solved by the path-ordered exponential, known as the Wilson line

$$\begin{aligned} U(x(t), y) &= \mathcal{P} \exp \left( \int_0^t dt' i a g A_\nu(t') \right) \\ &= \mathcal{P} \exp \left( i g \int_{x_\mu}^{x_\mu + at} dx'_\nu A_\nu(x') \right). \end{aligned}$$

Hence, for each direction  $\hat{\mu}$ , we define the gauge links between adjacent lattice sites to be

$$U_\mu(x) = \mathcal{P} \exp \left( i g \int_x^{x+a\hat{\mu}} dx' A_\mu(x') \right). \quad (2.21)$$

From this definition we also see that we can write the gauge link in the opposite direction, i.e. from  $x + a\hat{\mu}$  to  $x$ , as

$$\begin{aligned} \mathcal{P} \exp \left( i g \int_{x+a\hat{\mu}}^x dx' A_\mu(x') \right) &= \mathcal{P} \exp \left( -i g \int_x^{x+a\hat{\mu}} dx' A_\mu(x') \right) \\ &= U_\mu^\dagger(x). \end{aligned}$$

These gauge links have the simple gauge transformation property [7] (see Appendix C)

$$U_\mu(x) \rightarrow \Omega(x + a\hat{\mu}) U_\mu(x) \Omega^\dagger(x). \quad (2.22)$$

Making use of this gauge transformation property, we can construct gauge invariant Wilson loops by taking the trace of the product of the  $U_\mu$ 's around a closed loop. The simplest such loop, the  $1 \times 1$  square, is called the *plaquette*, and is defined as

$$P_{\mu\nu}(x) = U_\mu(x) U_\nu(x + a\hat{\mu}) U_\mu^\dagger(x + a\hat{\nu}) U_\nu^\dagger(x). \quad (2.23)$$

Calculating the Wilson loop by taking the trace of the plaquette we see that by the cyclic property of the trace the Wilson loop is gauge invariant

$$\begin{aligned} \text{Tr}(P_{\mu\nu}(x)) &\rightarrow \text{Tr}\left(\Omega(x) U_\mu(x) \Omega^\dagger(x + a\hat{\mu}) \Omega(x + a\hat{\mu}) U_\nu(x + a\hat{\mu}) \Omega^\dagger(x + a\hat{\mu} + a\hat{\nu}) \right. \\ &\quad \left. \Omega(x + a\hat{\mu} + a\hat{\nu}) U_\mu^\dagger(x + a\hat{\nu}) \Omega^\dagger(x + a\hat{\nu}) \Omega(x + a\hat{\mu}) U_\nu^\dagger(x) \Omega^\dagger(x)\right) \\ &= \text{Tr}(P_{\mu\nu}(x)) . \end{aligned}$$

We now return to the lattice formulation, making use of the gauge links to define our quantities of interest. Firstly, we approximate our gauge links on the lattice by using a midpoint definition, such that

$$U_\mu^{\text{lat}}(x) = \exp\left(iag A_\mu\left(x + \frac{a}{2}\hat{\mu}\right)\right). \quad (2.24)$$

From this definition, we can also recover the midpoint gauge potential [8, 9]

$$A_\mu\left(x + \frac{a}{2}\hat{\mu}\right) = \frac{1}{2iag} (U_\mu(x) - U_\mu^\dagger(x)) - \frac{1}{6iag} \text{Tr}(U_\mu(x) - U_\mu^\dagger(x)) I + \mathcal{O}(a^2). \quad (2.25)$$

We then note that we can write  $F_{\mu\nu}$  in terms of the plaquette by Taylor expanding Eq. 2.23 (see Appendix B) to obtain [10]

$$P_{\mu\nu} = I + ia^2 g F_{\mu\nu} - \frac{a^4 g^2}{2} F_{\mu\nu}^2 + \mathcal{O}(a^6), \quad (2.26)$$

and hence to  $\mathcal{O}(a^2)$

$$\frac{1}{2} \text{Tr}(F_{\mu\nu} F^{\mu\nu}) = \sum_{\mu,\nu} \frac{1}{g^2} \text{Tr}\left(I - \frac{1}{2} (P_{\mu\nu} + P_{\mu\nu}^\dagger)\right). \quad (2.27)$$

We have now arrived at a definition of the contracted field strength tensor that can be used to define our lattice action. As we only sum over the 6 unique plaquettes, we take into account a factor of 2 to arrive at the definition

$$\mathcal{S}_W = \beta \sum_x \sum_{\mu<\nu} \frac{1}{3} \text{Tr}\left(I - \frac{1}{2} (P_{\mu\nu} + P_{\mu\nu}^\dagger)\right), \quad (2.28)$$

where  $\beta = \frac{6}{g^2}$  is the lattice coupling constant. To remove higher order errors from the lattice action, it is possible to take into account terms containing larger Wilson loops,

following procedure similar to the one outlined above [11–13].

For the purpose of this work, the gauge fields were generated using the  $\mathcal{O}(a^2)$ -improved Lüscher and Weisz action [5],

$$\begin{aligned} \mathcal{S}_{LW} = & \sum_x \left[ \frac{5\beta}{9} \sum_{\mu<\nu} \text{Tr} \left\{ 1 - \frac{1}{2} (P_{\mu\nu} + P_{\mu\nu}^\dagger) \right\} \right. \\ & \left. - \frac{\beta}{36u_0^2} \sum_{\text{rect}} \text{Tr} \left\{ 1 - \frac{1}{2} (R_{\mu\nu} + R_{\mu\nu}^\dagger) \right\} \right], \end{aligned} \quad (2.29)$$

where

$$u_0 = \left( \frac{1}{3} \text{Re} \text{Tr} \langle P_{\mu\nu} \rangle \right)^{\frac{1}{4}}, \quad (2.30)$$

and  $R_{\mu\nu}$  is the  $2 \times 1$  rectangle Wilson loop, defined similarly to the plaquette

$$\begin{aligned} R_{\mu\nu}(x) = & U_\mu(x)U_\nu(x + \hat{\mu})U_\nu(x + \hat{\nu} + \hat{\mu})U_\mu^\dagger(x + 2\hat{\nu}) \\ & \times U_\nu^\dagger(x + \hat{\nu})U_\nu^\dagger(x) + U_\mu(x)U_\mu(x + \hat{\mu}) \\ & \times U_\nu(x + 2\hat{\mu})U_\mu^\dagger(x + \hat{\mu} + \hat{\nu})U_\mu^\dagger(x + \hat{\nu})U_\nu^\dagger(x). \end{aligned} \quad (2.31)$$

The presence of the ‘tadpole’ improvement factor  $u_0$  is necessary to modify the coupling constant such that the action has better agreement with the continuum over small distances [14]. This choice of action provides reduced errors in comparison to the Wilson action.

This lattice framework provides the tools necessary to explicitly calculate quantities of interest from a first-principles standpoint. Firstly, the gauge links are generated by monte-carlo methods, using  $\exp(-\mathcal{S})$  as a probability weighting for a given configuration. Once these configurations are generated, gauge fixing can be performed (Sec. 2.3.1, 3.2.1), and quantities of interest such as the gluon propagator (Chapter 4) can be obtained.

## 2.3 Gauge Fixing

The choice of gauge is crucial when performing calculations on the lattice, or, more generally, in any gauge field theory calculation. There are two choices of gauge relevant to this study: Landau gauge and maximal centre gauge. Maximal centre gauge is best explored in the context of centre vortices, and will therefore be detailed in chapter 3.2.1,

however the Landau gauge fixing condition provides a good introduction to the gauge fixing procedure, and as such will be described here.

### 2.3.1 Landau Gauge

In the continuum, Landau gauge corresponds to imposing the condition

$$\partial_\mu A^\mu = 0. \quad (2.32)$$

On the lattice, we can approximate this condition by imposing

$$\Delta(x) = \sum_\mu A_\mu \left( x + \frac{a}{2} \hat{\mu} \right) - A_\mu \left( x - \frac{a}{2} \hat{\mu} \right) = 0. \quad (2.33)$$

Here the fact that we have defined the lattice gauge potential to be at the midpoint of the link produces an improved continuum limit when we consider Eq. 2.33 in momentum space [9]. Performing a discrete Fourier transform, we see that

$$\begin{aligned} \Delta(p) &= \sum_x \Delta(x) e^{-ip \cdot x} \\ &= \sum_{x, \mu} e^{-ip \cdot x} \left( A_\mu \left( x + \frac{a}{2} \hat{\mu} \right) - A_\mu \left( x - \frac{a}{2} \hat{\mu} \right) \right) \\ &= \sum_{x, \mu} e^{ip \cdot \frac{a}{2} \hat{\mu}} e^{-ip \cdot (x + \frac{a}{2} \hat{\mu})} A_\mu \left( x + \frac{a}{2} \hat{\mu} \right) - e^{-ip \cdot \frac{a}{2} \hat{\mu}} e^{-ip \cdot (x - \frac{a}{2} \hat{\mu})} A_\mu \left( x - \frac{a}{2} \hat{\mu} \right) \\ &= \sum_\mu \left( e^{ip \cdot \frac{a}{2} \hat{\mu}} - e^{-ip \cdot \frac{a}{2} \hat{\mu}} \right) A_\mu(p) \\ &= \sum_\mu 2i \sin \left( \frac{a}{2} p_\mu \right) A_\mu(p) = 0. \end{aligned} \quad (2.34)$$

This is to be compared to the momentum space Landau gauge condition that can be obtained from the gauge potential defined on the lattice sites, rather than at the midpoint. If the midpoint definition is not used, the Landau gauge condition has the form has the form [9]

$$\sum_\mu [(\cos(ap_\mu) - 1) - i \sin(ap_\mu)] A'_\mu(p) = 0. \quad (2.35)$$

In the limit as  $a \rightarrow 0$ , it can be seen that Eq. 2.34 exhibits  $\mathcal{O}(a^2)$  improvement, whereas Eq. 2.35 has only  $\mathcal{O}(a)$  improvement.

The Landau Gauge condition is imposed on the Lattice by finding extrema of the functional [15]

$$\mathcal{F} = \frac{4}{3}\mathcal{F}_1 - \frac{1}{12u_0}\mathcal{F}_2, \quad (2.36)$$

where

$$\begin{aligned} \mathcal{F}_1 &= \sum_{\mu,x} \frac{1}{2} \text{Tr} \left\{ U_\mu^G(x) + U_\mu^G(x)^\dagger \right\} \\ \mathcal{F}_2 &= \sum_{\mu,x} \frac{1}{2} \text{Tr} \left\{ U_\mu^G(x) U_\mu^G(x + a\hat{\mu}) + U_\mu^G(x + a\hat{\mu})^\dagger U_\mu^G(x)^\dagger \right\}. \end{aligned}$$

We explicitly write  $U_\mu^\Omega$  to indicate that we are considering gauge links under an as-yet unknown gauge transformation  $\Omega$ . It becomes apparent why we seek the extrema of this particular functional when we take the functional derivative with respect to the free parameters of the gauge transformation,  $\omega^a(x)$  (see Eq. 2.2).

$$\frac{\delta \left\{ \frac{4}{3}\mathcal{F}_1 - \frac{1}{12u_0}\mathcal{F}_2 \right\}}{\delta \omega^a(x)} = ga^2 \sum_\mu \text{Tr} \left\{ \left[ \partial_\mu A_\mu(x) - \frac{4}{360}a^4 \partial_\mu^5 A_\mu(x) + \mathcal{O}(a^6) \right] \frac{\lambda^a}{2} \right\} + \mathcal{O}(g^3 a^4). \quad (2.37)$$

If Eq. 2.37 is at an extrema, then

$$\sum_\mu \partial_\mu A_\mu(x) = \sum_\mu \frac{4}{360}a^4 \partial_\mu^5 A_\mu(x) + \mathcal{O}(a^6) + \mathcal{O}(g^3 a^4).$$

Hence at order  $\mathcal{O}(a^4)$ , finding the extrema of Eq. 2.37 is equivalent to satisfying the continuum Landau gauge condition given in Eq. 2.32.

## 2.4 Lattice units

In the previous sections we have explicitly detailed how a variety of lattice quantities are constructed. For clarity, it is useful to remove extraneous constants by utilising so-called ‘lattice units’. Transforming to lattice units is done by multiplying physical quantities by relevant factors of the lattice spacing  $a$  to obtain a dimensionless quantity. Some examples of lattice units are

$$\begin{aligned} x_{\text{lat}} &= a^{-1} x_{\text{phys}} \\ p_{\text{lat}} &= a p_{\text{phys}} \\ A(x)_{\text{lat}} &= a A(x)_{\text{phys}}. \end{aligned}$$

Furthermore, it is also conventional to remove factors of  $g$  by setting  $g = 1$ . These conventions have the effect of removing factors of  $a$  and  $g$ , such that

$$\begin{aligned} A_\mu \left( x + \frac{a}{2} \hat{\mu} \right) &\rightarrow A_\mu \left( x + \frac{\hat{\mu}}{2} \right) \\ U_\mu(x) &\rightarrow \exp \left( i A_\mu \left( x + \frac{\hat{\mu}}{2} \right) \right) \\ P_{\mu\nu}(x) &\rightarrow U_\mu(x) U_\nu(x + \hat{\mu}) U_\mu^\dagger(x + \hat{\nu}) U_\nu^\dagger(x) \end{aligned}$$

These conventions will be adopted for the remainder of the remainder of the thesis unless stated otherwise.

# Chapter 3

## Topology of the Lattice

QCD presents two key properties that distinguish it from the other forces of nature:

1. Confinement of quarks, resulting in the absence of isolated quarks.
2. Dynamical chiral symmetry breaking, leading to dynamical generation of mass.  
This results in a substantial discrepancy between the mass of hadrons and the sum of the masses of the quarks that comprise them.

These properties have been observed experimentally, however the question of how they arise from the gauge theory of QCD outlined in the preceding chapter is still the subject of intense investigation. It is believed that both these properties are connected by some underlying topological structure of the QCD vacuum. Proposed candidates include Abelian monopoles [16–23], instantons [4, 24–28] and centre vortices [28–34]. With the advent of lattice simulations, the most promising of these appears to be the centre vortex model. Numerical evidence from the lattice has been amassed that indicates that topological objects known as centre vortices are tied to both confinement and dynamical chiral symmetry breaking [35–47]. It is therefore the subject of this research to further extend the investigation into the properties of centre vortices, specifically in the gluonic sector of QCD.

As dynamical chiral symmetry breaking is primarily concerned with quarks, we will omit a detailed discussion of this property and instead begin this chapter outlining the confinement property exhibited by the strong force. We will then introduce centre vortices and motivate how they provide a potential explanation for confinement in QCD. From here we will describe how it is that we can identify centre vortices on the lattice, and survey the lattice results found in current literature pertaining to

centre vortices. Finally we will briefly describe instantons and topological charge, in preparation for later chapters that draw on these concepts.

### 3.1 Confinement

The confinement property of QCD, and the accompanying notion of asymptotic freedom, is one of the defining low-energy features of the theory of the strong interaction. After Gell-mann and Zweig's concurrent proposal of quarks as the elementary constituents of baryons and mesons [48, 49], it was natural to then attempt to observe these new particles in isolation. However, efforts to observe quarks proved impossible. Early experiments testing the behaviour of electron-proton collisions demonstrated that protons scatter elastically, behaving as though they are finite-sized particles recoiling electromagnetically from the incident electron [50]. These experiments indicated no further substructure to the proton, inconsistent with the quark model. As accelerator energies improved, later experiments [51, 52], using electron energies of 7 and 10 GeV found that inelastic scattering effects became dominant, with electrons behaving as though they were scattering off of loosely bound constituent particles. To explain this behaviour, Feynman proposed what is known as the 'parton' model [53], treating the proton as being comprised of non-interacting electrically charged particles in the limit that the incident electron energy tends towards infinity. This is precisely the notion of asymptotic freedom; at large distance scales the partons are tightly bound, whereas at short distances they behave as free particles. It did not take long for the separate theories of quarks and partons to recognise as complementary, and by the early 70's the quark-parton model of hadrons accurately explained the the experimental results observed in particle colliders.

These experimental and theoretical results led in part to the development of the non-Abelian gauge field theory of QCD, as introduced in Chapter 2. The proof that non-Abelian gauge theories are asymptotically free was discovered in 1973 [54], and experimental evidence of the existence of 3 quark colours through study of the cross section of  $e^+e^-$  collisions supports the initial  $SU(3)$  colour symmetry anticipated by Gell-Mann and Zweig. At high energies, QCD has consistently explained the behaviour of hadronic matter, and has become the accepted theory of the strong nuclear interaction. However, the question of whether QCD is indeed a confining theory still remains. As confinement is a low-momentum property of QCD, it is apparent that any analytic proof of confinement must take place far from the asymptotic limit. To date, no such

analytic proof has been found.

Lattice calculations are currently the only method by which it is possible to investigate low-energy QCD phenomena from first-principles. Calculations of the static potential between two massive quarks, both recent and old [55–58], have shown that the potential rises linearly at sufficiently large separation distances. This behaviour is precisely what is expected of a colour confining theory. Other confinement mechanisms have also been proposed on the lattice, including mechanisms based on the behaviour of the gluon propagator at  $q = 0$  [59] and the behaviour of the pion mass and Polyakov loop at light quark masses [60]. All lattice results so far have indicated that QCD is in fact a confining theory at low energy.

There is good evidence that confinement has its roots in the topological properties of the QCD vacuum. It is well understood that the QCD vacuum, unlike the QED vacuum, admits non-trivial instanton solutions: solutions of the vacuum field configurations that are all minima of the classical action, yet are distinguished from one another by a topological quantum number [24]. The presence of instanton solutions was significant in resolving the  $U(1)$  anomaly [61], and provides an excellent method of calculating the ground state hadron spectrum [4]. The non-trivial topology of the QCD vacuum, and the success of topological features in resolving QCD anomalies, motivates the search for a topological explanation of confinement.

## 3.2 Centre Vortices

Originally proposed by 't Hooft in 1978 [29, 30], centre vortices are closed two-dimensional surfaces present in four-dimensional Euclidean space that carry colour-magnetic flux. The key property of a centre vortex is that in three dimensions, where the vortices appear as closed tubes, any Wilson loop (see Sec. 2.2) that encloses a vortex will acquire a centre phase, such that

$$W(C) \rightarrow z W(C), \quad (3.1)$$

where  $z$  is a non-trivial element of  $Z(3)$ , the centre of  $SU(3)$ . The centre of a group is the subgroup that contains all the elements of the group that commute with all other

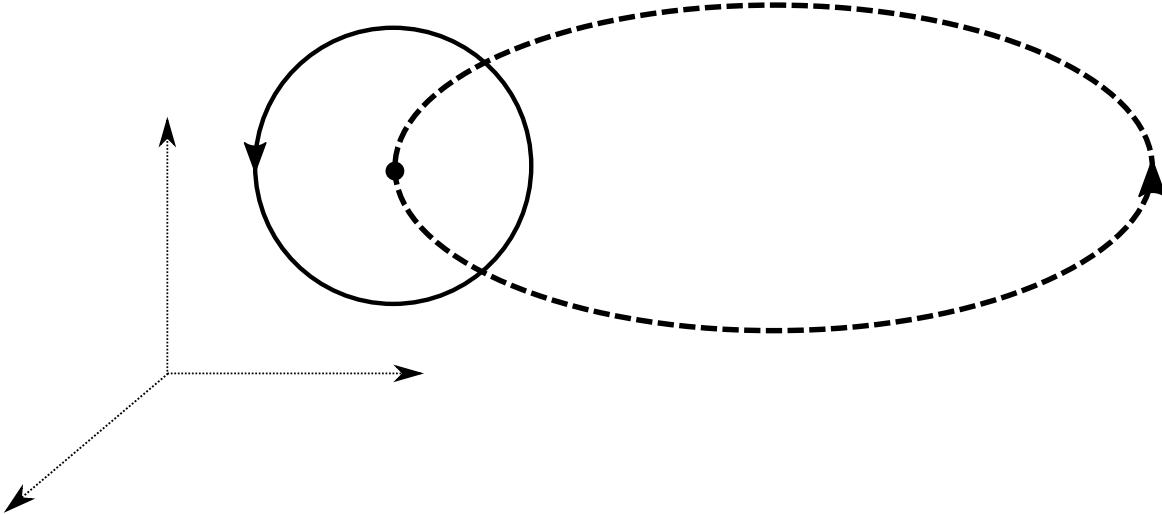


Fig. 3.1 A single centre vortex (dashed line) intersecting a Wilson loop (solid line) in 3 dimensions. The Wilson loop will acquire a centre phase corresponding to the phase of the vortex.

elements. In the case of  $SU(3)$  this corresponds to

$$Z(3) = \left\{ \exp\left(\frac{m2\pi i}{3}\right) I \mid m = 0, \pm 1 \right\}. \quad (3.2)$$

Thus, the non-trivial elements of  $Z_3$  are  $z = \exp\left(\frac{\pm 2\pi i}{3}\right) I$ . In the centre vortex model, it is therefore natural to refer to a vortex as being a ‘+1’ or ‘−1’ vortex, corresponding to the sign of the centre phase. When considering the value of any given Wilson loop, the centre vortex model suggests that

$$W(C) = \prod_i z_i \times W_0(C), \quad (3.3)$$

where the  $z_i$  correspond to the phases of the centre vortices intersecting the loop  $C$ , and  $W_0(C)$  encapsulates the short-distance physics. A simple visualisation of this idea is shown in Fig. 3.1. It is not immediately apparent why this form of the Wilson loop is related to confinement, however a simple  $SU(3)$  calculation motivates the relevance of this model [62]. To understand the significance of this calculation it is worth first deviating slightly to detail the relationship between the Wilson loop and the potential energy between two massive (static) quarks.

Follwing the argument presented in Ref. [63], consider a Wilson loop calculated around a rectangle in the  $x - t$  plane with dimensions  $R \times T$ . As the Wilson loop

is gauge invariant, we are free to select a convenient gauge in which to perform the calculation. To this end, we choose the fields to be in axial gauge, such that  $A_0(x) = 0 \implies U_0(x) = 1 \forall x$ . So the Wilson loop becomes

$$W(R \times T) = \text{Tr} \left( U_1(0) U_1^\dagger(T) \right). \quad (3.4)$$

We can insert a complete set of energy eigenstates,  $\sum_n |n\rangle \langle n| = 1$  to obtain

$$\begin{aligned} W(R \times T) &= \text{Tr} \left( \sum_n \langle U_1(0) | n \rangle \langle n | e^{-E_n(R)T} | U_1(0) \rangle \right) \\ &= \sum_n \text{Tr} \left( |\langle U_1(0) | n \rangle|^2 \right) e^{-E_n(R)T}. \end{aligned}$$

As  $T \rightarrow \infty$ , the only surviving contribution will be the lowest energy,  $E_0(R)$ . This means that

$$\lim_{T \rightarrow \infty} W(R \times T) \propto e^{-E_0(R)T}. \quad (3.5)$$

The quantity  $E_0(R)$  is the static quark potential, and if it is linear than its slope is referred to as the ‘string tension’,  $\sigma$ .

With Eq. 3.5 in mind, we return to the aforementioned  $SU(3)$  confinement model. Consider a two-dimensional plane of area  $L^2$ , with  $2N$  vortices piercing the plane. Assuming an even distribution of vortices, the total vortex density is  $\rho = \frac{2N}{L^2}$ . As there are two  $SU(3)$  vortex types, corresponding to the two non-trivial phases,  $z = \exp\left(\frac{\pm 2\pi i}{3}\right)$ , we assume that there is an equal distribution of vortex phases, i.e. there are  $N$  vortices of each type. The probability of finding  $n$  vortices of a given phase in some region of the plane  $A \subset L^2$  is equal to the probability that exactly  $n$  vortices are in  $A$ , multiplied by the probability that exactly  $N - n$  vortices are outside of  $A$ , multiplied by a combinatoric factor. Expressed mathematically, this is

$$P_N(n) = \binom{N}{n} \left(\frac{A}{L^2}\right)^n \left(1 - \frac{A}{L^2}\right)^{N-n}. \quad (3.6)$$

The expectation value of the Wilson loop around the perimeter of  $A$  can be written as

$$\langle W(\partial A) \rangle = \sum_{m,n=0}^N \left(\exp\left(\frac{2\pi i}{3}\right)\right)^n P_N(n) \left(\exp\left(-\frac{2\pi i}{3}\right)\right)^m P_N(m). \quad (3.7)$$

If we assume the vortex phases are uncorrelated, then we can make use of the following property of uncorrelated random variables  $X$  and  $Y$ ,

$$E[XY] = E[X] E[Y], \quad (3.8)$$

to write

$$\langle W(\partial A) \rangle = \sum_{n=0}^N \left( \exp\left(\frac{2\pi i}{3}\right) \right)^n P_N(n) \sum_{m=0}^N \left( \exp\left(\frac{2\pi i}{3}\right) \right)^m P_N(m). \quad (3.9)$$

We consider just the first sum in Eq. 3.9 and calculate

$$\begin{aligned} \sum_{n=0}^N \left( \exp\left(\frac{2\pi i}{3}\right) \right)^n P_N(n) &= \left( 1 - \frac{A}{L^2} \right)^N \sum_{n=0}^N \binom{N}{n} \left( \exp\left(\frac{2\pi i}{3}\right) \frac{A}{L^2} \left( 1 - \frac{A}{L^2} \right)^{-1} \right)^n \\ &= \left( 1 + \left( \exp\left(\frac{2\pi i}{3}\right) - 1 \right) \frac{A}{L^2} \right)^N, \end{aligned}$$

where we have made use of the binomial series to evaluate the sum. Hence the total expectation value is

$$\begin{aligned} \langle W(\partial A) \rangle &= \left( 1 + \left( \exp\left(\frac{2\pi i}{3}\right) - 1 \right) \frac{A}{L^2} \right)^N \left( 1 + \left( \exp\left(\frac{-2\pi i}{3}\right) - 1 \right) \frac{A}{L^2} \right)^N \\ &= \left( 1 - 3 \frac{A}{L^2} + 3 \left( \frac{A}{L^2} \right)^2 \right)^N \\ &= \left( \left( \frac{A}{L^2} \right)^3 + \left( 1 - \frac{A}{L^2} \right)^3 \right)^N. \end{aligned} \quad (3.10)$$

Rewriting Eq. 3.10 in terms of the vortex density  $\rho$ , we have

$$\langle W(\partial A) \rangle = \left( \left( \frac{A\rho}{2N} \right)^3 + \left( 1 - \frac{A\rho}{2N} \right)^3 \right)^N. \quad (3.11)$$

Now we take the limit as  $N, L^2 \rightarrow \infty$ , keeping  $\rho$  constant. Taking the limit, we find

$$\langle W(\partial A) \rangle = \exp\left(-\frac{3}{2}\rho A\right) \quad (3.12)$$

Letting  $A = R \times T$  as in Eq. 3.5, we see that  $E_0(R) = \frac{3}{2}\rho R$ , so the static quark potential rises linearly with string tension  $\sigma = \frac{3}{2}\rho$ , exactly as it should in a confining theory. Eq. 3.12 demonstrates an *area law* behaviour of the Wilson loop; this is often taken as a requirement for confinement [44, 64]. We see then that we have, from a set

of simple assumptions, constructed a model that exhibits confinement.

It is important to highlight the assumptions and simplifications made in the above argument. Most easily addressed is the assumption that there is an equal number of +1 and -1 vortices. By identifying vortices in Monte-Carlo generated configurations and plotting the distribution of phases in Fig. 3.2, we see that there is little deviation from an even distribution, especially in the ensemble average. This is an expected result, as vortices are tubes of chromo-magnetic flux, and thus must satisfy the Bianchi identity. In the absence of spontaneous symmetry breaking, this requirement is analogous to the electrodynamics condition  $\nabla \cdot B = 0$ , so we see that the flux line cannot terminate, and thus the tubes must be closed. Hence, over all space, we would expect that every +1 vortex is accompanied by a -1 vortex arising from the tube piercing the same plane in the opposite direction. On the lattice we observe a slight deviation from this idealised condition due to vortices being closed by lattice periodicity, but it is apparent that on average there is no preferred phase.

The assumption that the vortex density is constant is, however, less well motivated. So far we have treated vortices as infinitesimally thin sheets in 4D, which is not physically motivated. An infinitely thin vortex introduces a singularity in the action, as the vortex flux must be constrained to an infinitely thin cross-section. Rather, physical vortices are ‘thick’; they have a finite cross-section in the direction perpendicular to the vortex sheet. If the vortex is contained entirely within the area  $A$  it contributes the centre phase as described above. However, as  $A$  approaches the size of the vortex cross section, one must account for vortices that are only partially inside  $A$ , and thus not necessarily contributing a pure centre phase. Although this consideration spoils the elegance of the above confinement mechanism for small Wilson loops, it does potentially save the model from a previously noted pitfall related to the Casimir scaling of the Wilson loop expectation value [36, 65], as will be described in more detail in Sec. 3.2.2. Finally, it is worth noting that this issue is only relevant to Wilson loops of similar size to the vortex cross-section. As the Wilson loop increases in size, the majority of the vortices will be contained entirely within the loop, with a diminishing number of thick vortices overlapping the perimeter of the loop, as shown in Fig. 3.3.

The final assumption is that the vortex locations are random and uncorrelated from one another. This is perhaps the most significant assumption made in the above picture, as can be seen from the following calculation [66]. As vortices must form

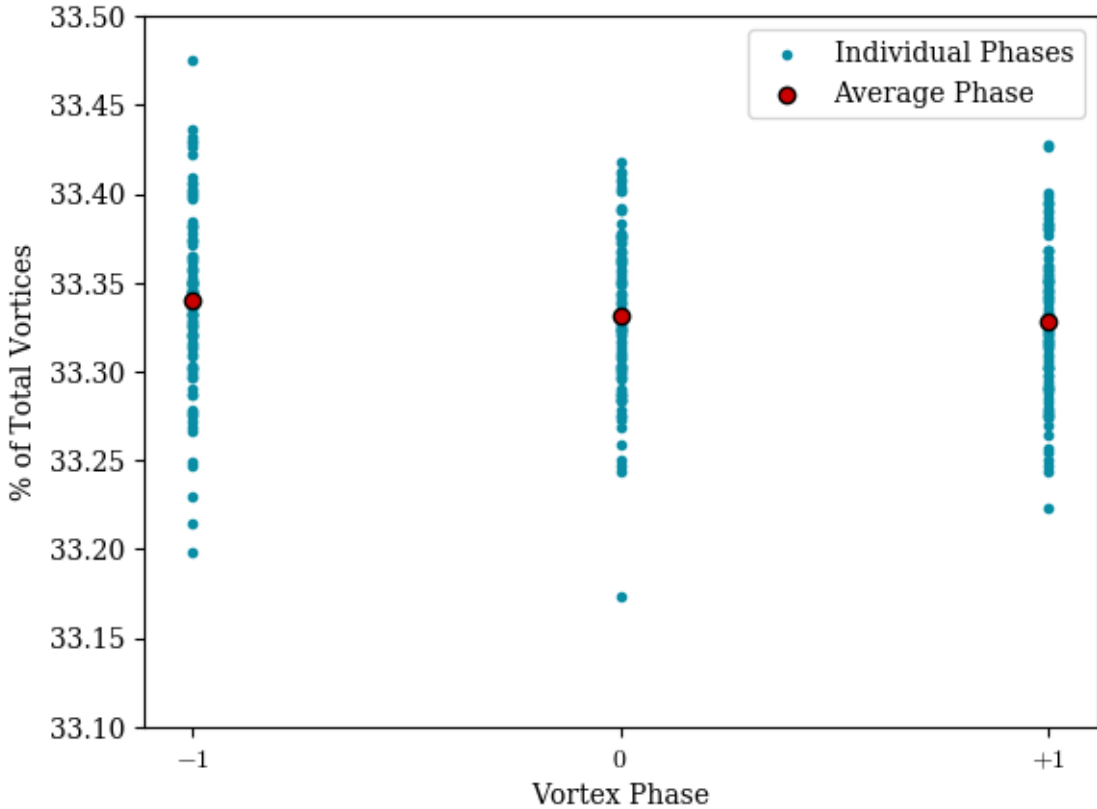


Fig. 3.2 A plot of the vortex phase distribution of 100 Monte-Carlo generated configurations, as a percentage of the total number of vortices. The method by which vortices are identified will be detailed in Sec. 3.2.1.

closed lines in 3D, let us suppose that instead of being randomly distributed, the vortices come in pairs separated by a maximum distance  $d$ . This corresponds to requiring that vortex lines form a closed loop of some maximum diameter  $d$ . If this vortex line pierces the Wilson loop in both directions, then the product of the phases,  $\exp\left(\frac{2\pi i}{3}\right) \times \exp\left(-\frac{2\pi i}{3}\right) = 1$ , results in no contribution to the Wilson loop. Hence, the only vortices capable of contributing a non-trivial phase to the Wilson loop are those contained within a strip of width  $d$  about the perimeter of the loop. Note that not every vortex within this strip will contribute a non-trivial phase, as the vortex may be smaller than  $d$  or oriented such that the vortex flows in direction of  $\partial A$  and thus still pierces twice. We will take the most generous case, however, and assume that every vortex piercing this strip contributes a non-trivial phase. To first order, the area of relevance to the expectation value of the Wilson loop is now  $A_{\text{strip}} = \partial A d$ . The

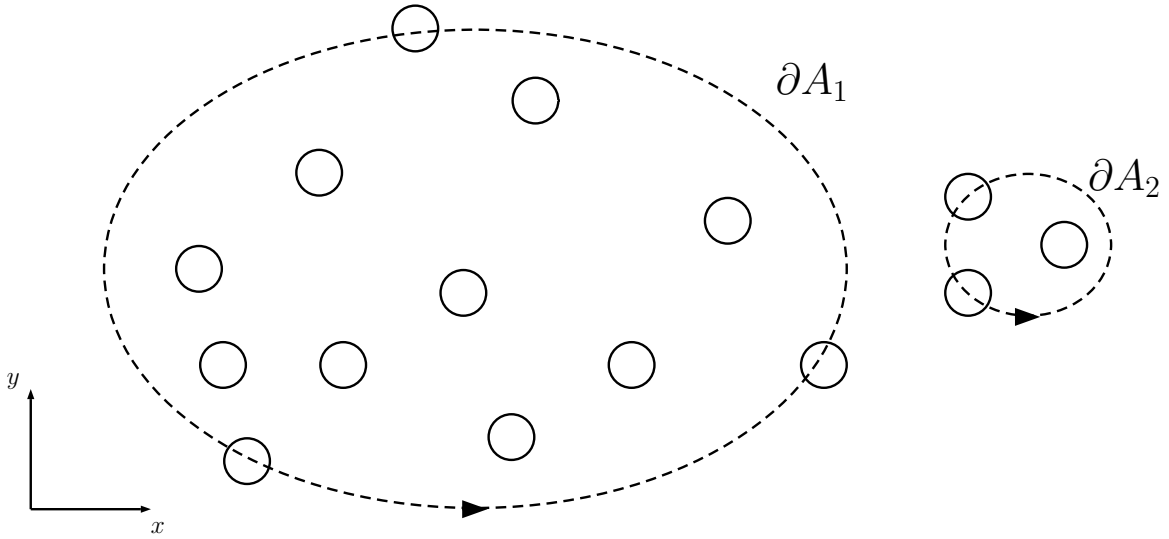


Fig. 3.3 An example of two Wilson loops (dashed lines) lying in a plane, pierced by vortices of finite cross-section (solid lines). **Left:** The majority of vortices contributing to the phase are fully contained within the large loop, with only a few overlapping at the perimeter. **Right:** For a small loop, the contribution from overlapping vortices is significant as there are few vortices fully inside the loop.

probability to find  $N$  vortices lying within this strip is

$$P_N(n) = \binom{N}{n} \left( \frac{\partial Ad}{L^2} \right)^n \left( 1 - \frac{\partial Ad}{L^2} \right)^{N-n}. \quad (3.13)$$

By following the same steps used to arrive at Eq. 3.12, we find

$$\langle W(\partial A) \rangle = e^{-\frac{3}{2}\rho d \partial A}. \quad (3.14)$$

So we see that instead of an area law, we now have a perimeter law for the Wilson loop, dependent on the upper bound for the vortex size. This implies that if there is some upper limit on the size of a vortex, we can no longer expect to see confining behaviour. We therefore deduce that to obtain a confining theory, it is necessary to allow the vortex size to be potentially infinite. In the language of the vortex model, this is called *vortex percolation*. Conversely, the presence of an upper bound on the vortex size would imply a deconfined phase. This suggests that the size of vortices can be used as an *order parameter* for confinement [37], with two distinct phases:

1. Vortex percolation  $\implies$  confinement.
2. Loss of vortex percolation  $\implies$  deconfinement.

### 3.2.1 Locating Centre Vortices

Now that we have motivated the case for the centre vortex model, we wish to consider how it is that we identify vortices on a lattice configuration. The guiding principle behind the method we employ is that we wish to find some way to distinguish between a configuration containing vortices, and the same configuration with the vortices removed. Note that the vortex-free configuration is not necessarily trivial; it will still contain all the short distance physics we wish to ignore. We should therefore discuss how it is that a vortex can be inserted into a configuration to first build up a picture of what it is that separates a configuration containing vortices from one that does not.

We know from the previous section that our vortex insertion must result in a transformation of the Wilson loop containing the vortex such that

$$W(C) \rightarrow zW(C), \quad z = \exp\left(\frac{\pm 2\pi i}{3}\right). \quad (3.15)$$

It should be apparent that this behaviour is not possible from an ordinary gauge transformation, as the Wilson loop is a gauge invariant quantity. There is an infinite class of gauge transformations that can result in this behaviour, but the key property connecting them is that they are *singular* [29]. This means that the transformations associate the same point in space with two different values. For example, consider a gauge potential  $A_\mu$  undergoing a gauge transformation  $\Omega$  around a closed circle  $C$ . Let  $\theta$  be the angular coordinate, and define the gauge transformation

$$\Omega(\theta) = \exp(-i\theta Q), \quad \theta \in [0, 2\pi], \quad (3.16)$$

where

$$Q = \frac{1}{2}\lambda_3 + \frac{1}{2\sqrt{3}}\lambda_8 = \frac{1}{3} \text{diag}(2, -1, -1) \quad (3.17)$$

As  $\Omega(0) \neq \Omega(2\pi)$ , the transformation is singular. According to Eq. 2.22 the gauge link around the path,  $U(x(\theta), \theta = 0)$ , then becomes

$$U(x(\theta), \theta = 0) \rightarrow \Omega(2\pi) U(x(\theta), \theta = 0) \Omega(0), \quad (3.18)$$

with the corresponding Wilson loop

$$W_0(C(\theta)) \rightarrow \text{Tr} (\Omega(2\pi) U(x(\theta), \theta = 0) \Omega(0)) \quad (3.19)$$

$$= \text{Tr} \left( \exp \left( \frac{2\pi i}{3} \right) U(x(\theta), \theta = 0) \right) \quad (3.20)$$

$$= \exp \left( \frac{2\pi i}{3} \right) W_0(C(\theta)). \quad (3.21)$$

We see that through the use of a singular centre transformation we have introduced a centre vortex to the configuration. Note that the transformation in Eq. 3.16 is not unique, and if written in Cartesian coordinates the singular nature is replaced by a pole at the centre of the circle. The literature makes use of both these definitions of the vortex gauge transformation [29, 67]. As our vortex depends only on the angular coordinate, this vortex is infinitely thin, as any size Wilson loop will acquire the vortex flux. Transformations creating thick vortices by adding a radial profile to the singular gauge transformation have been explored in Ref. [36]. On the lattice, this gauge transformation corresponds to multiplying a single link  $U_\mu(x)$  by the centre phase  $\exp \left( \frac{2\pi i}{3} \right)$ , such that the plaquettes associated with this link are multiplied by the same centre phase, creating in 3D a  $1 \times 1$  vortex, as seen in Fig. 3.4. Larger vortices are created by multiplying more links by the same centre phase. This suggests that we can consider our gauge links to be of the form

$$U_\mu(x) = Z_\mu(x) R_\mu(x), \quad (3.22)$$

where  $Z_\mu(x)$  is the ‘vortex-only’ field consisting of centre elements, and  $R_\mu(x)$  is the background ‘vortex-removed’ field.

With the understanding that a configuration containing vortices differs from one that doesn’t by a singular gauge transformation, we should consider the *adjoint representation* of  $SU(3)$ , as it has the property of being invariant under centre transformations. The adjoint representation is defined such that any  $SU(3)$  element in this representation can be written in the form  $U_\mu^A(x) = \exp(i\omega_k(x)f^k)$ , where  $f^k$  are the  $8 \times 8$   $SU(3)$  structure constants. These constants are given by the Lie algebra relationship

$$\left[ \frac{\lambda_i}{2}, \frac{\lambda_j}{2} \right] = i \sum_k f_{ij}^k \frac{\lambda_k}{2}. \quad (3.23)$$

To transform the gauge links  $U_\mu(x)$  from the fundamental representation to the adjoint representation, it is necessary to find a mapping  $D : SU(3)^F \rightarrow SU(3)^A$  that preserves

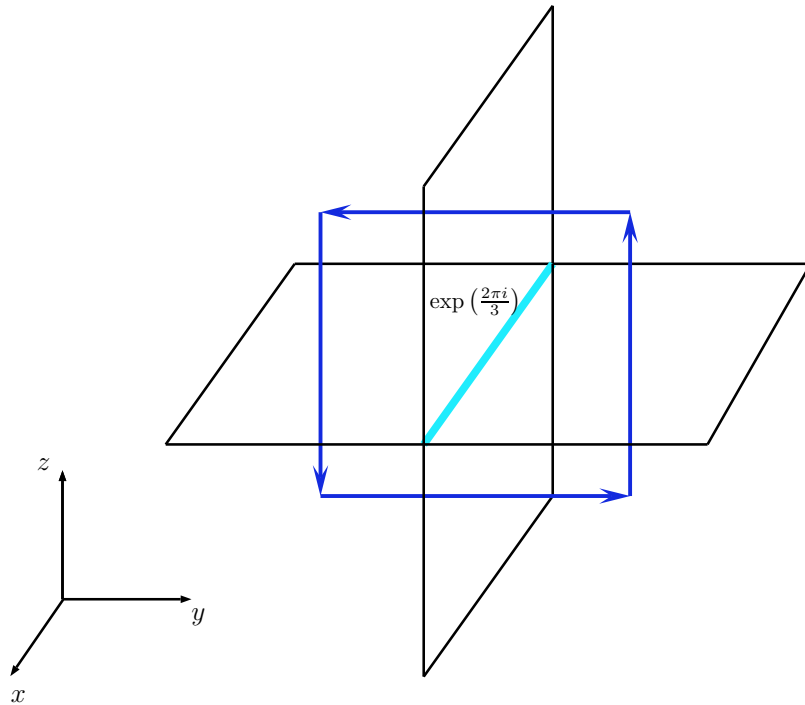


Fig. 3.4 A  $1 \times 1$  vortex (blue) created by multiplying the centre link (cyan) by a centre phase. Note that there are two more plaquettes in the time direction that have been suppressed, which serve to make the vortex a cube in 4D.

the group operation. This means that for any  $U, V \in SU(3)^F$ , then we require that

$$D(UV) = D(U)D(V). \quad (3.24)$$

Consider the mapping

$$\left[ U_\mu^A(x) \right]_{ij} = [D(U_\mu(x))]_{ij} = \frac{1}{2} \text{Tr} \left( \lambda_i U_\mu(x) \lambda_j U_\mu(x)^\dagger \right). \quad (3.25)$$

This mapping satisfies Eq. 3.24 (see Appendix D), and it is easy to see that if  $U_\mu(x) \rightarrow Z_\mu(x) U_\mu(x)$  for  $Z_\mu \in Z_3$  then  $U_\mu^A(x)$  is unchanged. This means that the adjoint representation is invariant under singular centre transformations (or, more generally, any centre transformation) and is therefore insensitive to the presence of vortices in a given configuration. Considering the decomposition of  $U_\mu(x)$  into vortex-only and vortex-removed components presented in Eq. 3.22, we see that in the adjoint representation,

$$U_\mu^A = R_\mu^A. \quad (3.26)$$

It is then clear that the adjoint representation can be utilised to isolate the background vortex-removed field. This property is key to the vortex identification procedure described below.

### Maximal Centre Gauge

We now turn to the choice of gauge used to identify vortices in the fundamental representation. Known as maximal centre gauge, this gauge serves to bring each gauge link on the lattice as close as possible to a centre element, such that

$$\left\| U_\mu^\Omega(x) - Z_\mu(x) \right\| , \quad (3.27)$$

is minimised. There are numerous implementations of this gauge [68, 69], however we choose to implement it by maximising the “mesonic” functional [46]

$$R = \frac{1}{VN_{\text{dim}} n_c^2} \sum_{x,\mu} \left| \text{Tr } U_\mu^G(x) \right|^2 , \quad (3.28)$$

where  $VN_{\text{dim}}$  is the number of links on the lattice, and  $n_c = 3$  is the number of colours. At first glance it is unclear why this gauge would assist in isolating vortices. To elucidate the connection, we consider the trace of the adjoint gauge link  $U_\mu^A(x)$  obtained from Eq. 3.25,

$$\text{Tr} \left( U_\mu^A(x) \right) = |\text{Tr} (U_\mu(x))|^2 - 1 . \quad (3.29)$$

The details of the above expression are given in Appendix D. We see therefore that maximising Eq. 3.28 is equivalent to maximising

$$R^A = \frac{1}{VN_{\text{dim}} n_c^2} \sum_{x,\mu} \left( \text{Tr } U_\mu^{A,G}(x) \right) . \quad (3.30)$$

$R^A$  is clearly maximised when  $U_\mu^A(x) = I$ , which requires that  $U_\mu(x) \in Z_3$ . Thus, maximising  $R^A$  is equivalent to bringing the vortex-removed field  $R_\mu(x)$  as close as possible to the identity, which in the idealised case would take  $U_\mu(x) \rightarrow Z_\mu(x)$ . Of course, it is in general not possible to fully gauge-away the  $R_\mu(x)$  field, but we assume that once  $R$  is maximised the trace is sufficiently close to the centre phase  $Z_\mu(x)$  that it identifies the centre element associated with this link. To then construct the vortex-only field, we simply project onto this nearest centre element. This projection step is not a gauge rotation, and naturally removes all the short-range physics, as we

have essentially enforced a trivial background configuration. This projection gives us our three sets of configurations:

1. Original ‘untouched’ fields,  $U_\mu(x)$ ,
2. Projected vortex-only fields,  $Z_\mu(x)$ ,
3. Vortex-removed fields,  $R_\mu(x) = Z_\mu^\dagger(x) U_\mu(x)$ .

These three sets will be collectively referred to as our vortex-modified configurations for the remainder of this research.

There are two primary assumptions related to this vortex identification method [67]. The first is due to the degeneracy in the maxima of  $R$ , the so-called Gribov copy issue. This degeneracy results in it being unclear whether a given maxima is the global maxima, or merely local. If it is local, and far from the global maxima, then it is entirely possible that vortices will be misidentified. This is because the background vortex-removed field contribution could be far from the identity, resulting in an incorrect centre phase being obtained when the configuration is projected onto  $Z_3$ .

The second assumption is that the partitioning of  $U_\mu(x)$  into  $Z_\mu(x)$  and  $R_\mu(x)$  is valid. In other words, we assume that the physical thick vortices are sufficiently small such that they can be defined by a series of single-link centre transformations on the lattice, like that shown in Fig. 3.4, rather than by a larger multiple-link transformation, as shown in Fig. 3.5. This is equivalent to the discontinuity related to the vortex being larger than a single plaquette. If the vortices are too large, the MCG procedure becomes unable to contract their thickness such that they are identified by a single link.

Although these assumptions are potentially strict, numerical evidence has shown that if a vortex is inserted into a configuration by hand, then the above MCG procedure is capable of consistently identifying its location [67, 68]. This suggests that the required assumptions are valid to a fair degree, and thus we are motivated to continue to employ this vortex identification method. Furthermore, efforts to improve the obtained value of  $R$  through use of simulated annealing [70] or preconditioning [71] have found that the amount of identified vortices actually decreases as  $R$  is increased, and the resulting phenomenology is worse overall. The proposed reasoning for this is that these improvement techniques have the property of increasing the size of vortices, resulting

in an amplification of the issue raised above, in which the MCG procedure fails to identify large vortices. Hence, based on these prior findings, we do not attempt to escape the first Gribov region the MCG procedure finds itself in, as in the study of centre vortices it is appropriate to remain near this local maxima.

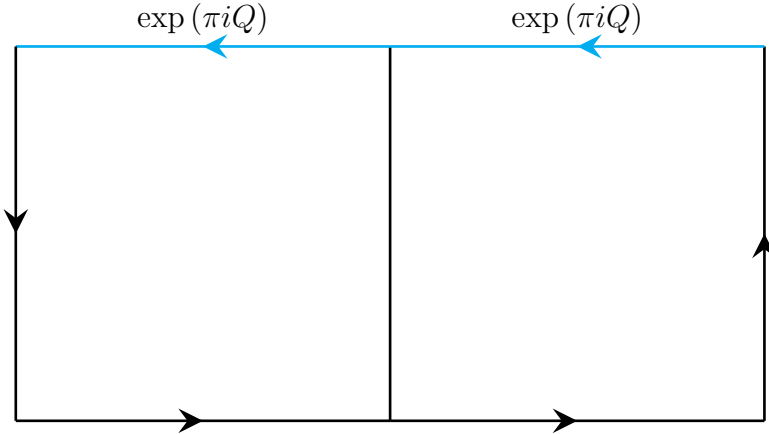


Fig. 3.5 An example of a  $2 \times 1$  vortex, arising from a centre transformation split across two links (cyan). Each  $1 \times 1$  plaquette individually will not acquire a centre phase, but the the  $2 \times 1$  loop will.

### 3.2.2 Current Evidence for Centre Vortices

Now that we have developed an understanding of centre vortices and how they are located, we can summarise briefly the current lattice evidence surrounding vortices and their relationship to various calculable quantities.

#### String Tension

As discussed previously, the string tension is the slope of the linear potential observed between two massive, static quarks. In  $SU(2)$  studies, it has been shown that vortex removal results in a complete loss of the string tension, and on vortex only configurations it is possible to fully replicate it [71]. In  $SU(3)$  the picture is less clear. Without smoothing (see Chapter 5), it is only possible to regain  $\sim 62\%$  of the original string tension on the vortex only configurations [46]; however, under vortex removal the string tension vanishes just as in the  $SU(2)$  case. Under smoothing, it is possible to achieve  $\sim 97\%$  agreement, however the overall string tension on both the untouched and vortex only configurations is reduced to approximately 37% of the original un-smoothed string tension [39].

## Hadron Spectrum

The low-lying hadron spectrum provides an excellent probe of the presence of dynamical chiral symmetry breaking. By comparing the masses of hadrons that would have degenerate mass if chiral symmetry is restored, we can observe whether dynamical mass generation effects are present. Through use of the overlap fermion action, it has been possible to show in  $SU(3)$  that the vortex-only spectrum under a small amount of cooling closely follows the trends of the untouched hadron spectrum [41]. The slight discrepancy can be attributed to the necessity of cooling when considering the vortex only configurations. On the vortex removed configurations, dynamical mass generation vanishes and hadrons with the same quark content once again become degenerate [41]. This is a clear signal of the restoration of chiral symmetry.

## Mass Function

The mass function,  $M(p)$ , represents the observed mass of a quark as a function of momentum. Dynamical mass generation presents itself as an amplification of the low-momentum mass function, indicating an observed long-range mass that is greater than the bare mass of the quark. After 10 sweeps of cooling this amplification is indeed observed on both the vortex only and untouched mass function of  $SU(3)$  configurations, whereas on the vortex removed mass function this amplification is greatly suppressed [40]. In  $SU(2)$ , similar behaviour has also been observed [38].

## Casimir Scaling

Casimir scaling refers to the behaviour of the  $SU(N)$  string tension in different representations (see e.g. the adjoint representation introduced in Sec. 3.2.1). As  $N$  becomes increasingly large, it is found that the fundamental string tension  $\sigma_F$  is related to the adjoint string tension  $\sigma_A$  by  $\sigma_A = 2\sigma_F$  [65]. Given our prior discussion of the adjoint representation, this should at first glance appear a surprising result, as we stressed that the adjoint representation is insensitive to the presence of vortices and thus the centre vortex model would suggest a vanishing string tension in the adjoint representation. However, numerical evidence shows that this is certainly not the case, even for  $SU(2)$  and  $SU(3)$  [72–74]. This apparent contradiction can be resolved by considering vortices of finite thickness, as done in Ref. [36]. This finite thickness manifests as a Wilson loop acquiring a vortex contribution of the form

$$G(x) = \Omega \exp(i\alpha_C(x) Q) \Omega^\dagger \quad (3.31)$$

where  $\Omega \in SU(3)$ ,  $Q$  is as defined in Eq. 3.17 and  $\alpha_C \in [0, 2\pi]$  is a function satisfying

$$\alpha_C(x) = \begin{cases} 0, & \text{Vortex lies entirely outside the Wilson loop of perimeter } C \\ 2\pi, & \text{Vortex lies entirely inside the Wilson loop of perimeter } C \end{cases} . \quad (3.32)$$

Clearly for  $\alpha_C(x) = 0, 2\pi$  we recover the thin vortex behaviour, however the structure of  $\alpha_C(x)$  away from these cases encodes a generalised vortex thickness. This thickness appears to resolve the Casimir scaling contradiction, and give the appropriate scaling behaviour for other representations of  $SU(N)$  as well [36].

### Gluon Propagator

The gluon propagator,  $D(p^2)$ , (see Chapter 4) serves as an indicator of confinement. Similar to the mass function, low-momentum enhancement indicates non-perturbative behaviour. In both  $SU(2)$  and  $SU(3)$  it has been shown that vortex removal indicates a loss of this enhancement, suggesting a loss of confinement [47, 75, 76]. However, vortex only results have not been previously calculated; these results are one of the main accomplishments of this research, and are presented in Chapter 6.

## 3.3 Further Topological Quantities

Although not the primary focus of this work, it is informative to provide a definition for topological charge and introduce the notion of an instanton. Both these quantities provide a useful measure of the topological structure of the lattice, especially when we come to consider smoothing routines in Chapter 5. Topological charge provides a simple numerical measure of the contribution of all topological objects. Furthermore, there is a connection between the location of topological charge and the geometry of centre vortices, specifically the intersection, touching and writhing points of centre vortices [77, 78]. Instantons are often used as the reference topological object in the literature [39, 79], with preservation of the instanton content of the lattice equated to a preserved topological structure.

### 3.3.1 Topological Charge

The total topological charge is the ‘degree’ of a particular field configuration, counting how many times  $A_\mu$  covers the Lie algebra  $\mathfrak{su}(3)$ . Numerically, it is given by [80]

$$Q = \int d^4x \frac{1}{16\pi^2} \epsilon_{\mu\nu\rho\sigma} \text{Tr} (F_{\mu\nu} F_{\rho\sigma}) \in \mathbb{Z}. \quad (3.33)$$

The term in the integrand is known as the topological charge density, denoted  $q(x)$ . From Eq. 2.26 it is clear we could evaluate  $F_{\mu\nu}$  by taking the imaginary part of  $P_{\mu\nu}$ . However, it is common to make use of the clover leaf definition,

$$q_{\text{clov}}(x) = \frac{1}{16\pi^2} \epsilon_{\mu\nu\rho\sigma} \text{Tr} (C_{\mu\nu} C_{\rho\sigma}), \quad (3.34)$$

where

$$C_{\mu\nu} = \frac{1}{4} \text{Im} (P_{\mu\nu}(x) P_{\mu\nu}(x - \hat{\mu}) P_{\mu\nu}(x - \hat{\nu}) P_{\mu\nu}(x - \hat{\mu} - \hat{\nu})). \quad (3.35)$$

The clover-leaf loop combination is shown in Fig. 3.6. Much like the Lüscher and Weisz action, we can expand this clover definition with larger combinations of loops to remove higher order errors. In our calculation of topological charge in Sec. 7.3, we employ a 5-loop improved topological charge, taking into account a linear combination of  $1 \times 1$ ,  $2 \times 1$ ,  $2 \times 2$ ,  $2 \times 3$  and  $3 \times 3$  clover loops [81].

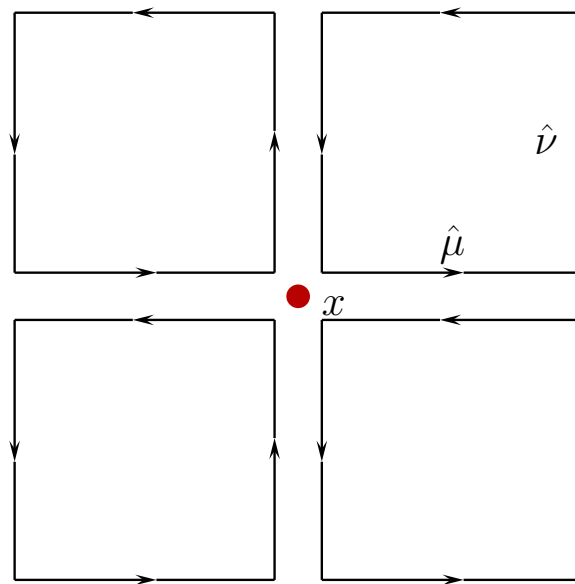


Fig. 3.6 The four plaquettes that compose the clover combination  $C_{\mu\nu}$ .

### 3.3.2 Instantons

The QCD vacuum is a non-trivial state, existing as a superposition of an infinite number of degenerate solutions enumerated by a topological quantum number. These solutions can be expressed as a gauge rotation from the trivial  $A_\mu = 0$  solution, such that

$$A_\mu = i(\partial_\mu \Omega) \Omega^\dagger. \quad (3.36)$$

These are the so-called ‘pure gauge’ configurations. For these vacuum configurations, the topological charge defined in Eq. 3.33 has a slightly modified interpretation; it now counts how many times the gauge transformation  $\Omega(x)$  covers the group  $SU(3)$ . If we require that as  $|x| \rightarrow \infty$ ,  $A_\mu \rightarrow 0$ , then Eq. 3.33 becomes an integral of a total divergence and reduces to the Pontryagin number, calculated as an integral over the boundary of Euclidean space  $S^3$  [3]

$$Q = \frac{1}{24\pi^2} \oint_{S^3} \epsilon_{\mu\nu\rho\sigma} \hat{\mu} \text{Tr} \left( (\Omega^\dagger \partial_\nu \Omega) (\Omega^\dagger \partial_\rho \Omega) (\Omega^\dagger \partial_\sigma \Omega) \right) \quad (3.37)$$

We wish to consider the potential tunnelling between different vacuum states, with a difference in topological charge  $\Delta Q = 1$ . If we impose the condition

$$\int d^3x (q(t = \infty) - q(t = -\infty)) = 1, \quad (3.38)$$

we can construct the gauge potential for a configuration inhabiting one vacuum at  $t = \infty$ , and another vacuum at  $t = -\infty$ . This solution for  $A_\mu$  given these conditions is known as an instanton solution [4]. Unfortunately, there is no known analytic solution for an instanton in  $SU(3)$ . However, there is a known  $\Delta Q = 1$  instanton in  $SU(2)$ , known as the Belavin-Polyakov-Schwartz-Tyupkin (BPST) instanton solution [24]. It has the form

$$A_\mu(x) = \frac{2\eta_{a\mu\nu} x_\nu}{x^2 + \rho^2} \frac{\sigma^a}{2}, \quad (3.39)$$

where

$$\eta_{a\mu\nu} = \begin{cases} \epsilon_{a\mu\nu}, & \mu, \nu = 1, 2, 3 \\ \delta_{a\mu}, & \nu = 4 \\ -\delta_{a\nu}, & \mu = 4 \end{cases}, \quad (3.40)$$

$\sigma^a$  are the Pauli matrices and  $\rho$  is an arbitrary parameter known as the instanton radius. An anti-instanton solution corresponding to  $\Delta Q = -1$  can be obtained by substituting  $\eta$  with  $\bar{\eta}$ , where  $\bar{\eta}$  is the same as Eq. 3.40 but with a factor of  $-1$  in the

last two cases. The action associated with this configuration is

$$S_0 = \frac{8\pi^2}{g^2}, \quad (3.41)$$

and the field strength tensor is given by [4]

$$(F_{\mu\nu}^a)^2 = \frac{192\rho^2}{(x^2 + \rho^2)^4}. \quad (3.42)$$

Despite not being an  $SU(3)$  instanton, the BPST solution can be embedded in  $SU(3)$ . This allows for the identification of instanton-like objects on the lattice, as performed in Refs. [39, 82].

# Chapter 4

## Lattice Configurations and the Gluon Propagator

Now that we have developed the required background understanding of lattice QCD and the topological objects of interest to this research, we can detail how our calculations are performed. This chapter will first describe how we calculate the primary quantity of interest in the first part of this research, the Landau gauge gluon propagator, on the lattice. We will then motivate our choice of momentum variables, before proceeding to a description of the lattice parameters and data cuts utilised in this work.

### 4.1 Lattice Definition of the Gluon Propagator

In a gauge field theory the position-space propagator,  $D_{\mu\nu}(x, y)$ , of the gauge boson is the two-point correlation function. In the case of QCD this can be interpreted as the probability amplitude of a gluon being created at the space-time point  $x$ , propagating to  $y$ , and then being annihilated. The propagator therefore serves as a useful measure of the behaviour of gluons as a function of distance; or, correspondingly, as a function of momentum in the momentum-space representation. In this section we detail how the momentum-space Landau gauge gluon propagator is calculated on the lattice. We begin with the definition of the coordinate space propagator as a two-point correlator [59, 75, 83].

$$D_{\mu\nu}^{ab}(x) = \langle A_\mu^a(x) A_\nu^b(0) \rangle. \quad (4.1)$$

The propagator in momentum space is simply related by the discrete Fourier transform,

$$D_{\mu\nu}^{ab}(p) = \sum_x e^{-ip \cdot x} \langle A_\mu^a(x) A_\nu^b(0) \rangle. \quad (4.2)$$

Noting that the coordinate space propagator  $D_{\mu\nu}^{ab}(x - y)$  only depends on the difference  $x - y$ , such that

$$\langle A_\mu^a(x) A_\nu^b(0) \rangle = \langle A_\mu^a(x + y) A_\nu^b(y) \rangle, \quad (4.3)$$

we can make use of translational invariance to average over the four-dimensional volume to obtain the form for the momentum space propagator.

$$\begin{aligned} D_{\mu\nu}^{ab}(p) &= \frac{1}{V} \sum_{x,y} e^{-ip \cdot x} \langle A_\mu^a(x + y) A_\nu^b(y) \rangle \\ &= \frac{1}{V} \sum_{x,y} \langle e^{-ip \cdot (x+y)} A_\mu^a(x + y) e^{+ip \cdot y} A_\nu^b(y) \rangle \\ &= \frac{1}{V} \langle A_\mu^a(p) A_\nu^b(-p) \rangle. \end{aligned} \quad (4.4)$$

Hence we find that the momentum space gluon propagator on a finite lattice with four-dimensional volume  $V$  is given by

$$D_{\mu\nu}^{ab}(p) \equiv \frac{1}{V} \langle A_\mu^a(p) A_\nu^b(-p) \rangle. \quad (4.5)$$

In the continuum, the Landau-gauge momentum-space gluon propagator has the following form [8, 84]

$$D_{\mu\nu}^{ab}(p) = \left( \delta_{\mu\nu} - \frac{p_\mu p_\nu}{p^2} \right) \delta^{ab} D(p^2), \quad (4.6)$$

where  $D(p^2)$  is the scalar gluon propagator. Contracting Gell-Mann index  $b$  with  $a$  and Lorentz index  $\nu$  with  $\mu$  one has

$$D_{\mu\mu}^{aa}(p) = (4 - 1)(n_c^2 - 1) D(p^2), \quad (4.7)$$

such that the scalar function can be obtained from the gluon propagator via

$$D(p^2) = \frac{1}{3(n_c^2 - 1)} D_{\mu\mu}^{aa}(p), \quad (4.8)$$

where  $n_c = 3$  is the number of colours.

As the lattice gauge links  $U_\mu(x)$  naturally reside in the  $3 \times 3$  fundamental representation of  $SU(3)$ , we now wish to work in the matrix representation of  $A_\mu(x)$ , as introduced in Eq. 2.4. Using the orthogonality relation  $\text{Tr}(\lambda_a \lambda_b) = 2\delta_{ab}$  for the

Gell-Mann matrices, it is straightforward to see that

$$2 \operatorname{Tr}(A_\mu A_\mu) = A_\mu^a A_\mu^a, \quad (4.9)$$

which can be substituted into equation 4.8 to obtain the final expression for the lattice scalar gluon propagator,

$$D(p^2) = \frac{2}{3(n_c^2 - 1)V} \langle \operatorname{Tr} A_\mu(p) A_\mu(-p) \rangle. \quad (4.10)$$

To calculate Eq. 4.10 on the lattice, we need to define  $A_\mu(p)$ . As defined in Eq. 2.25, we make use of the midpoint definition of the coordinate-space gauge potential in terms of the lattice link variables. Once the link variables are fixed to Landau gauge following the procedure described in Sec. 2.3.1, we can obtain the momentum-space gauge potential by performing a Fourier transform,

$$A_\mu(p) = \sum_x e^{-ip \cdot (x + \hat{\mu}/2)} A_\mu(x + \hat{\mu}/2). \quad (4.11)$$

We have now constructed a workable lattice definition to calculate the Landau gauge scalar gluon propagator within the lattice framework established in Chapter 2.

## 4.2 Momentum Variables

As discussed in Sec. 3.1, it is understood that at QCD is asymptotically free. With this understanding, we expect that at high momentum the Landau gauge gluon propagator will tend towards the Landau gauge photon propagator [3]

$$D_\gamma(p^2) = \frac{1}{p^2}. \quad (4.12)$$

However, lattice discretisation errors cause a deviation from this idealised behaviour that we would like to systematically account for. To do this, we follow the work of Refs. [12, 13, 85–87] and consider the behaviour of the photon propagator on the lattice. We therefore consider for this section only an Abelian theory. The field strength tensor is then simplified to

$$F_{\mu\nu} = \partial_\mu A_\nu - \partial_\nu A_\mu \quad (4.13)$$

We consider this Abelian field to be on a lattice generated using the Wilson action (see Eq. 2.28). From Eq. 2.27 we know that the Wilson action can be written as

$\mathcal{S}_W = a^4 \frac{1}{2} \sum_x F_{\mu\nu} F^{\mu\nu} + \mathcal{O}(a^4)$ . As we are interested in the momentum-space propagator, we write the field strength tensor at the plaquette midpoint  $\tilde{x}$  as

$$\begin{aligned} F_{\mu\nu}(\tilde{x}) &= \sum_p e^{ip\tilde{x}} \left( \frac{A_\nu(\tilde{x} + a\hat{\frac{\mu}{2}}) - A_\nu(\tilde{x} - a\hat{\frac{\mu}{2}})}{a} - \frac{A_\mu(\tilde{x} + a\hat{\frac{\nu}{2}}) - A_\mu(\tilde{x} - a\hat{\frac{\nu}{2}})}{a} \right) \\ &= \frac{1}{a} \sum_p e^{ip\tilde{x}} \left( \tilde{A}_\nu(p) e^{-iap\hat{\frac{\mu}{2}}} - \tilde{A}_\nu(p) e^{iap\hat{\frac{\mu}{2}}} - \tilde{A}_\mu(p) e^{-iap\hat{\frac{\nu}{2}}} + \tilde{A}_\mu(p) e^{iap\hat{\frac{\nu}{2}}} \right) \\ &= -\frac{1}{a} \sum_p e^{ip\tilde{x}} \left( 2i \sin\left(\frac{ap_\mu}{2}\right) \tilde{A}_\nu(p) - 2i \sin\left(\frac{ap_\nu}{2}\right) \tilde{A}_\mu(p) \right) \\ &= -\sum_p e^{ip\tilde{x}} \tilde{f}_{\mu\nu}(p), \end{aligned}$$

where

$$\tilde{f}_{\mu\nu}(p) = i \left( \hat{k}_\mu \tilde{A}_\nu(p) - \hat{k}_\nu \tilde{A}_\mu(p) \right), \quad \hat{k}_\mu = \frac{2}{a} \sin\left(\frac{ap_\mu}{2}\right). \quad (4.14)$$

The Wilson action can therefore be written as

$$\begin{aligned} \mathcal{S}_W &= a^4 \frac{1}{2} \sum_{\tilde{x}} \sum_{p, p'} e^{i\tilde{x}(p+p')} \tilde{f}_{\mu\nu}(p) \tilde{f}^{\mu\nu}(p') \\ &= a^4 \frac{1}{2} \sum_{p, p'} \delta(p + p') \tilde{f}_{\mu\nu}(p) \tilde{f}^{\mu\nu}(p') \\ &= a^4 \frac{1}{2} \sum_p \tilde{f}_{\mu\nu}(p) \tilde{f}^{\mu\nu}(-p) + \mathcal{O}(a^4). \end{aligned} \quad (4.15)$$

We are now in a position to consider the propagator. Equivalent to the two-point correlator definition, the propagator is also the Green's function of the equations of motion,  $M_{\mu\nu}$ , satisfying

$$M_{\mu\nu} D^{\nu\lambda}(p) = \delta_\mu^\lambda. \quad (4.16)$$

In the continuum, we can write the Abelian Lagrangian in terms of momentum space variables as

$$\begin{aligned} \mathcal{L} &= \frac{1}{2} \tilde{F}_{\mu\nu} \tilde{F}^{\mu\nu} \\ &= \frac{1}{2} (k_\mu \tilde{A}_\nu - k_\nu \tilde{A}_\mu) (k^\mu \tilde{A}^\nu - k^\nu \tilde{A}^\mu) \\ &= (k^2 \delta_{\mu\nu} - k_\mu k_\nu) \tilde{A}^\mu \tilde{A}^\nu, \end{aligned}$$

and hence

$$M_{\mu\nu} = (k^2 \delta_{\mu\nu} - k_\mu k_\nu). \quad (4.17)$$

However, it is understood that in the continuum the equations of motion are not invertible unless an additional gauge fixing term is added, with a gauge fixing parameter  $\alpha$ . Hence, the equations of motion for the photon field in momentum space are given by Eq. 4.17 with an additional gauge fixing term [3]

$$M_{\mu\nu} = k^2 \delta_{\mu\nu} - \left(1 - \frac{1}{\alpha}\right) k_\mu k_\nu . \quad (4.18)$$

By inspection, we see that Eq. 4.15 will have the same equations of motion, with the substitution  $k_\mu \rightarrow \hat{k}_\mu$ . In turn, this gives the propagator

$$D_{\mu\nu}(p) = \frac{1}{\hat{k}^2} \left[ \delta_{\mu\nu} + (\alpha - 1) \frac{\hat{k}_\mu \hat{k}_\nu}{\hat{k}^2} \right] . \quad (4.19)$$

Landau gauge corresponds to setting  $\alpha = 0$ , so we find that

$$D_{\mu\mu}(p) = \frac{3}{\hat{k}^2} , \quad (4.20)$$

and therefore by comparison with Eq. 4.8 we see that

$$D(p^2) = \frac{1}{\hat{k}^2} . \quad (4.21)$$

This suggests that for the Wilson action we should make the substitution  $p_\mu \rightarrow q_\mu = \hat{k}_\mu = \frac{2}{a} \sin\left(\frac{ap_\mu}{2}\right)$  so that at tree-level we observe the expected behaviour of the gluon propagator.

A similar analysis can be performed for the Lüscher and Weisz action, taking into account the contributions from the rectangle terms. The Lüscher and Weisz action written in the same form as Eq. 4.15 is [85]

$$\mathcal{L}_{\text{LW}} = a^4 \frac{1}{2} \sum_p \left( 1 + \frac{1}{12} a^2 \hat{k}^2 \right) \tilde{f}_{\mu\nu}(p) \tilde{f}^{\mu\nu}(-p) + \mathcal{O}(a^6) . \quad (4.22)$$

The equations of motion then become

$$M_{\mu\nu} = \left( \hat{k}^2 + \frac{1}{12} a^2 \hat{k}^4 \right) \delta_{\mu\nu} - \left( 1 - \frac{1}{\alpha} \right) \left( \sqrt{\hat{k}_\mu^2 + \frac{1}{12} a^2 \hat{k}_\mu^4} \right) \left( \sqrt{\hat{k}_\nu^2 + \frac{1}{12} a^2 \hat{k}_\nu^4} \right) . \quad (4.23)$$

Therefore the propagator is

$$D_{\mu\nu}(p) = \frac{1}{q^2} \left[ \delta_{\mu\nu} + (\alpha - 1) \frac{q_\mu q_\nu}{q^2} \right], \quad (4.24)$$

with

$$q_\mu = \sqrt{\hat{k}_\mu^2 + \frac{1}{12}a^2\hat{k}_\mu^4} = \frac{2}{a} \sqrt{\sin^2\left(\frac{p_\mu a}{2}\right) + \frac{1}{3}\sin^4\left(\frac{p_\mu a}{2}\right)}. \quad (4.25)$$

In Landau gauge, this suggests the tree-level form for the scalar propagator is

$$D(p^2) = \frac{a^2}{4\sin^2\left(\frac{p_\mu a}{2}\right) + \frac{1}{3}\sin^4\left(\frac{p_\mu a}{2}\right)} = \frac{1}{q^2}. \quad (4.26)$$

For this work, we make the variable substitution  $p_\mu \rightarrow q_\mu$  to ensure that at high momentum where we expect the gluon propagator to tend towards tree level we observe that  $q^2 D(q^2) = 1$ . The momentum variables chosen for both the Wilson and Lüscher and Weisz action have been numerically verified to provide better tree level agreement in Refs. [84, 88], and we present a comparison of the Lüscher and Weisz and uncorrected variables in Fig. 4.1. We plot  $k^2 D(k^2)$  (where  $k_\mu$  is the momentum variable for the given case under consideration) such that the tree-level propagator appears as  $k^2 D(k^2) = 1$ , shown as the black dashed line. We can clearly see that at high momenta the corrected gluon propagator tends towards the expected tree-level behaviour, whereas the uncorrected propagator fans out considerably. This fanning is the result of asymmetry between the spacial and temporal components of the propagator, which is accounted for in the tree-level correction [88]. The results presented in Fig. 4.1 clearly motivate the need for tree-level correction when calculating the gluon propagator on the lattice.

### 4.3 Lattice Parameters and Data Cuts

We calculate the gluon propagator on 100 configurations of a  $20^3 \times 40$   $SU(3)$  lattice with spacing  $a = 0.125$  fm, as used in Refs. [40, 45]. When considering the gluon propagator it is useful to maintain the plotting convention introduced in Fig. 4.1 of considering  $q^2 D(q^2)$  against  $qa$ . This has the twofold benefit of both aiding in visualisation of the tree-level behaviour, and enabling clearer analysis of the infrared properties of the

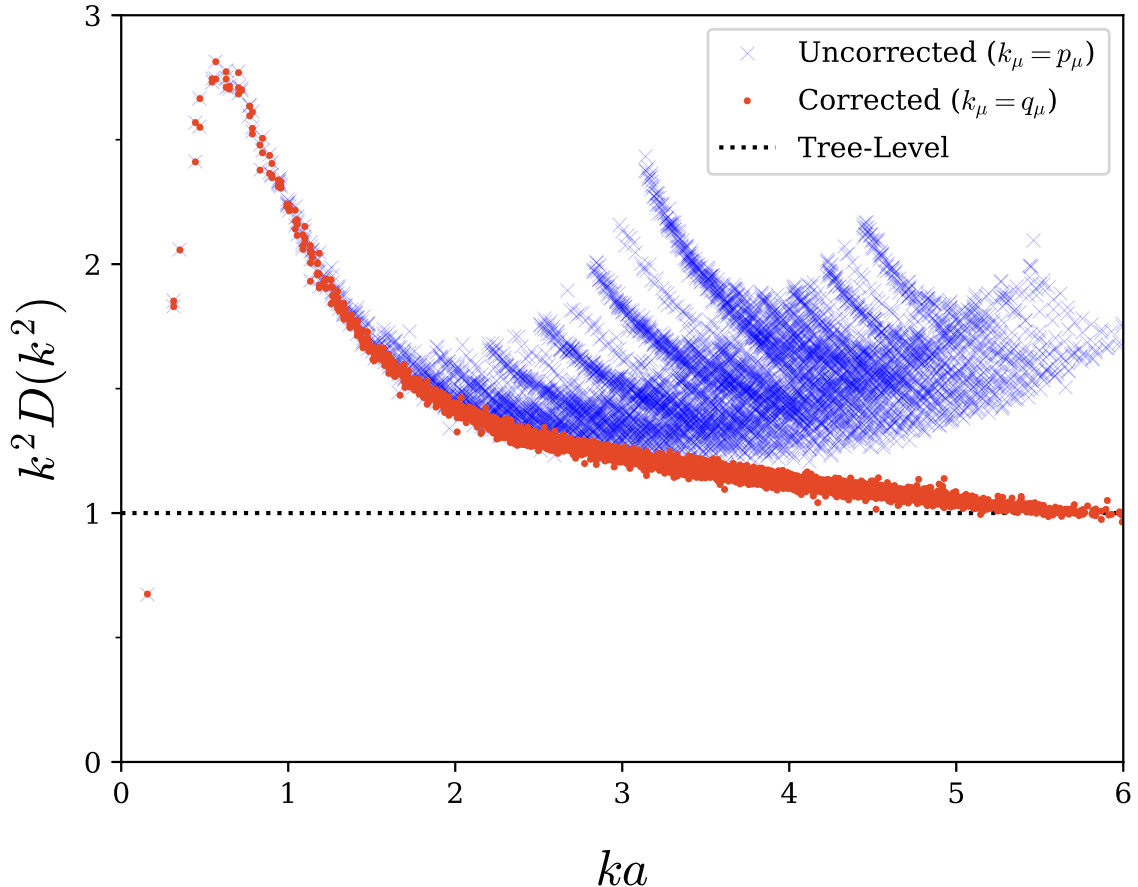


Fig. 4.1 The scalar gluon propagator is plotted with no tree-level momentum correction (blue crosses) and the Lüscher and Weisz correction (red dots) presented in Eq. 4.26. It is clear that the corrected momentum has improved tree-level behaviour, free from the fanning effect present in the uncorrected case.

propagator by suppressing the low- $qa$  region. Following the procedure of Ref. [8, 84] all results are plotted after a momentum half-cut. The momentum half-cut corresponds to only considering lattice momenta in the range

$$p_\mu = \frac{2\pi n_\mu}{aN_\mu}, \quad n_\mu \in \left(-\frac{N_\mu}{4}, \frac{N_\mu}{4}\right]. \quad (4.27)$$

This cut limits the positive range of the kinematically corrected  $q_\mu$  to

$$q_\mu \in \left[0, \frac{2\sqrt{21}}{3a}\right] \approx \left[0, \frac{3.06}{a}\right]. \quad (4.28)$$

Furthermore, a cylinder cut of radius  $pa = 2$  lattice units is performed such that we only consider points within two lattice units of the diagonal. This cut is implemented by considering points satisfying

$$|pa|^2 \sin(\theta_c) \leq 2, \quad (4.29)$$

where

$$\theta_c = \cos^{-1} \left( \frac{pa \cdot \hat{n}}{|pa|} \right), \quad (4.30)$$

and  $\hat{n} = \frac{1}{2}(1, 1, 1, 1)$  is the unit vector along the diagonal. This is performed so that all directions are equally sampled, whilst omitting points where one direction dominates the signal. This assists in filtering out high-momentum systematic errors. Finally, we can take advantage of the rotational symmetry of the scalar propagator to perform  $Z(3)$  averaging over the Cartesian coordinates. This means that we average over all points with the same Cartesian radius; for example, we would average across the points  $(n_x, n_y, n_z) = (2, 1, 1), (1, 2, 1)$  and  $(1, 1, 2)$ . These choices of cuts assist in producing a cleaner signal that accurately represents the behaviour of the continuum propagator.

With these cuts implemented, the gluon propagator on the untouched configurations appears as Fig. 4.2. We observe the expected tree-level behaviour at high momenta, with an infrared enhancement indicative of amplified low-momentum propagation. Due to the cuts we have made, we observe a much cleaner signal, particularly in the region  $qa \geq 1.5$ , in agreement with the results of Ref. [84]. It should be noted that the difference in peak height observed between Fig. 4.1 and Fig. 4.2 is due to a different renormalisation constant. This issue will be discussed in detail in Sec. 6.1.2.

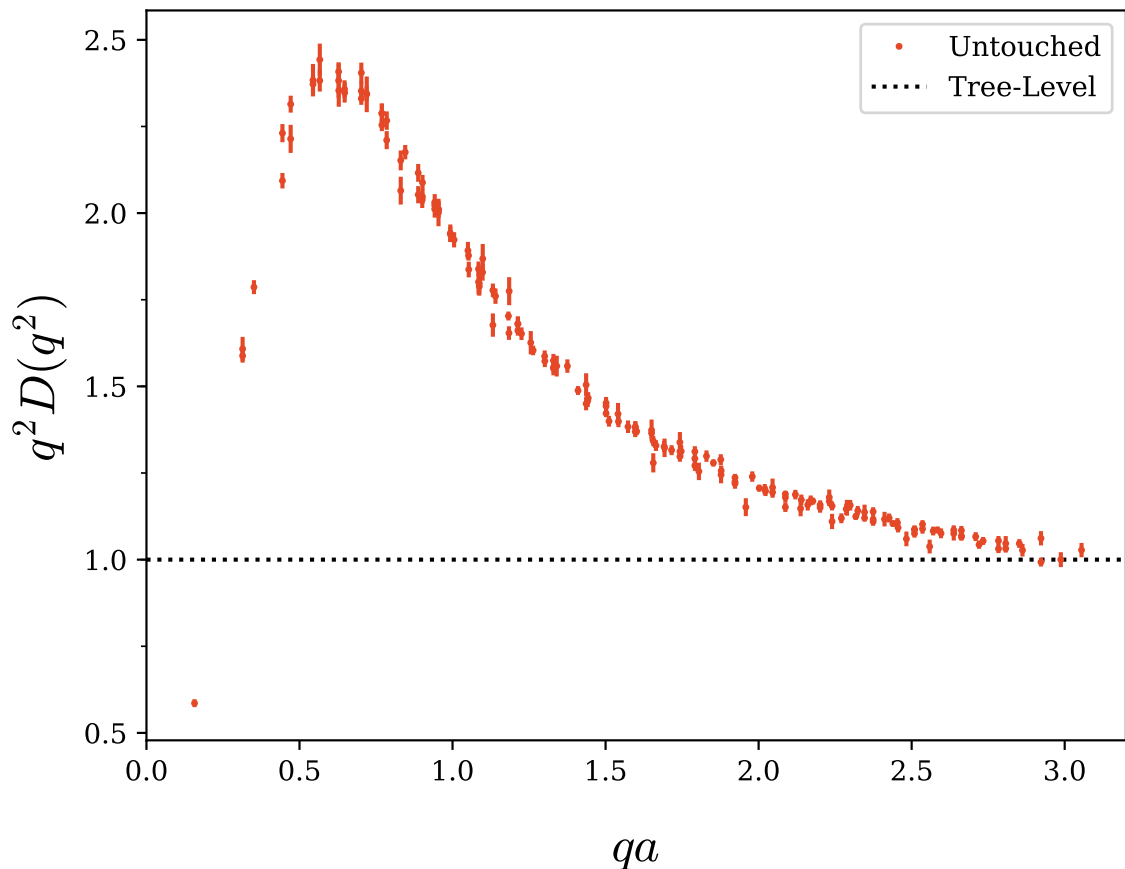


Fig. 4.2 The untouched gluon propagator with all data cuts and correct momentum variables utilised. We observe a substantially cleaner signal when compared to the untouched propagator shown in Fig. 4.1.



# Chapter 5

## Smoothing

Lattice definitions of topological objects are plagued by random fluctuations originating from the Monte-Carlo generation of lattice configurations and as a result they can give inaccurate or even nonsensical results. Hence, when considering the behaviour of topological objects on the lattice, it has been proven to be necessary to remove the high frequency fluctuations in the gauge fields [89]. Furthermore, when investigating the long range behaviour of the lattice it is also beneficial to filter off the short distance fluctuations to better reveal the physics in the domain of interest [79]. This filtering process is known as smoothing, and it forms an important step in any study of lattice topological objects and long range behaviour. For example, it has previously been shown that smoothing is necessary to obtain agreement between the untouched and vortex only string tension, mass function and instanton content [39–41]. The process of removing these fluctuations is known as smoothing, which in turn falls into two sub-categories: cooling and smearing.

The purpose of both these methods is similar, however, the algorithms used to implement them differ. Cooling assesses each link in turn, replacing the existing link with one that locally minimises some choice of action (see e.g. the Wilson action, Eq. 2.28). Rather than explicitly minimising a given action, smearing instead replaces each link with a weighted average of its nearest neighbours. Once every link in the lattice has been updated according to one of these methods, the configuration is said to have had one sweep of smoothing applied. The process can then be repeated to an arbitrary number of sweeps to achieve the desired degree of smoothness. Due to the differences in the routines, it is important to compare the results from both to observe how they each perform and quantitatively observe how they alter the measured quantities.

## 5.1 Smoothing Methods

### 5.1.1 Cooling

Cooling is the original method devised for smoothing lattice gauge fields, first utilised in an analysis of the topological susceptibility of simplified lattice models [90]. It was shown early on that the process of cooling can be used to distinguish between 'genuine' topological charge representative of classical minima of the action, and background Monte-Carlo topological charge brought about by random fluctuations created during the generation of the lattice configuration. Under cooling, the former is preserved whilst the latter is annihilated. The process of cooling according to the simplest Wilson action is based on the method outlined by Cabibbo and Marinari [91, 92], and is performed as follows:

We first consider the Wilson action associated with a single link  $U_\mu$ ,

$$S(U_\mu) = 3 - \text{Re Tr}(U_\mu \bar{U}), \quad (5.1)$$

which is a different, but completely equivalent, form of Eq. 2.28.  $\bar{U}$  is defined as the sum of the 'staples' associated with  $U_\mu$ . A staple is the product of all the link variables around a chosen loop, except for the link being cooled. For example, the  $1 \times 1$  plaquette staple associated with  $U_\mu$  is

$$\tilde{U}_{\mu\nu}^{1\times 1}(x) = U_\nu(x + \hat{\mu})U_\mu^\dagger(x + \hat{\nu})U_\nu^\dagger(x). \quad (5.2)$$

Graphically, this can be seen as in Fig. 5.1. Larger staples are defined similarly; for

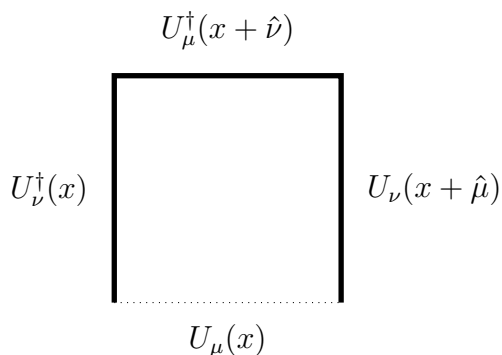


Fig. 5.1 An example  $1 \times 1$  staple, with the dashed link indicating the link the staple is relative to. The origin of the name staple is apparent from the shape of the 3 solid links.

example a  $2 \times 2$  staple corresponds to the product of seven of the eight links in the  $2 \times 2$  square, with  $U_\mu(x)$  omitted. For the Wilson action, the six unique  $1 \times 1$  staples are the only ones required. Once all relevant staples are calculated, they are summed to obtain

$$\bar{U} = \sum_{\alpha=1}^6 \tilde{U}_\alpha, \quad (5.3)$$

where  $\alpha$  enumerates the staples, not the Lorentz index.

The objective of cooling is to select a new  $SU(3)$  matrix to replace  $U_\mu$  with some  $U'_\mu$  that minimises Eq. 5.1, or equivalently, maximises

$$R = \text{Re Tr}(U'_\mu \bar{U}). \quad (5.4)$$

Naively, it would seem that  $U'_\mu = \bar{U}^{-1}$  would be the ideal choice. However,  $\bar{U}$  is a sum of  $SU(3)$  matrices, and  $SU(3)$  is only closed under multiplication, not addition. Hence,  $\bar{U}$ , and by extension  $\bar{U}^{-1}$ , are not necessarily in  $SU(3)$ , making  $\bar{U}^{-1}$  an invalid substitute for  $U_\mu$ . However, any  $SU(2)$  element can be written in the form  $U = a_0 I + i\vec{a} \cdot \vec{\sigma}$ , where  $\vec{\sigma}$  are the Pauli matrices and  $a \in \mathbb{R}^4$  satisfies  $a^2 = 1$ . Hence, a sum of  $SU(2)$  elements will be proportional to another  $SU(2)$  element. We can exploit this fact to construct a new  $SU(3)$  element from three  $SU(2)$  subgroups. To this end, we wish to find a  $U'$  of the form

$$U'_\mu = a_3 a_2 a_1 U_\mu, \quad (5.5)$$

where the  $a_i$  are each in different a  $3 \times 3$  representation of  $SU(2)$ . We define the following three functions,  $F_i(V)$ , such that  $F_i : SU(3) \rightarrow SU(2)$ :

$$\begin{aligned} F_1(V) &= \frac{1}{k_1} \begin{pmatrix} \frac{1}{2} (V_{11} + V_{22}^*) & \frac{1}{2} (V_{12} - V_{21}^*) & 0 \\ \frac{1}{2} (V_{21} - V_{12}^*) & \frac{1}{2} (V_{11}^* + V_{22}) & 0 \\ 0 & 0 & k_1 \end{pmatrix}, \\ F_2(V) &= \frac{1}{k_2} \begin{pmatrix} \frac{1}{2} (V_{22} + V_{33}^*) & 0 & \frac{1}{2} (V_{23} - V_{32}^*) \\ 0 & k_2 & 0 \\ \frac{1}{2} (V_{32} - V_{23}^*) & 0 & \frac{1}{2} (V_{22}^* + V_{33}) \end{pmatrix}, \\ F_3(V) &= \frac{1}{k_3} \begin{pmatrix} k_3 & 0 & 0 \\ 0 & \frac{1}{2} (V_{11} + V_{33}^*) & \frac{1}{2} (V_{13} - V_{31}^*) \\ 0 & \frac{1}{2} (V_{31} - V_{13}^*) & \frac{1}{2} (V_{11}^* + V_{33}) \end{pmatrix}, \end{aligned}$$

where  $k_i^2$  is the determinant of the  $2 \times 2$   $SU(2)$  sub-block. The  $\frac{1}{k_i}$  factor therefore fixes the determinant such that  $\det(F_i(V)) = 1$ . We now wish to find a suitable  $V$  to define our  $a_i$ 's. Consider the first case,  $U_\mu^{(1)} = a_1 U_\mu$ , and let  $a_1 = F_1(U_\mu \bar{U})^\dagger$ . It is worth stating explicitly that it is this step where the fact that a sum of  $SU(2)$  matrices is proportional to an  $SU(2)$  matrix is utilised. Despite the fact that  $U_\mu \bar{U} \notin SU(3)$ ,  $U_\mu \tilde{U}_\alpha \in SU(3)$ , which implies that  $F_i(U_\mu \tilde{U}_\alpha) \in SU(2)$ . Then we have, for example,

$$\begin{aligned} F_1(U_\mu \bar{U}) &= \frac{1}{k_1} \sum_{\alpha} \begin{pmatrix} \frac{1}{2} ((U_\mu \tilde{U}_\alpha)_{11} + (U_\mu \tilde{U}_\alpha)_{22}^*) & \frac{1}{2} ((U_\mu \tilde{U}_\alpha)_{12} - (U_\mu \tilde{U}_\alpha)_{21}^*) & 0 \\ \frac{1}{2} ((U_\mu \tilde{U}_\alpha)_{21} - (U_\mu \tilde{U}_\alpha)_{12}^*) & \frac{1}{2} ((U_\mu \tilde{U}_\alpha)_{11}^* + (U_\mu \tilde{U}_\alpha)_{22}) & 0 \\ 0 & 0 & k_1 \end{pmatrix} \\ &= \frac{1}{k_1} \sum_{\alpha} \begin{pmatrix} k_{1,\alpha} (F_1(U_\mu \tilde{U}_\alpha))_{11} & k_{1,\alpha} (F_1(U_\mu \tilde{U}_\alpha))_{12} & 0 \\ k_{1,\alpha} (F_1(U_\mu \tilde{U}_\alpha))_{21} & k_{1,\alpha} (F_1(U_\mu \tilde{U}_\alpha))_{22} & 0 \\ 0 & 0 & k_1 \end{pmatrix} \\ &= \frac{1}{k_1} \sum_{\alpha} \left( \begin{array}{c|c} k_{1,\alpha} F_1(U_\mu \tilde{U}_\alpha)_{2 \times 2} & 0 \\ \hline 0 & k_1 \end{array} \right) \end{aligned} \quad (5.6)$$

The  $2 \times 2$  block in Eq. 5.6 is a sum over terms proportional to  $SU(2)$  matrices, and hence the result is proportional to an  $SU(2)$  matrix. Thus with the appropriate normalisation from the  $k_1$  factor, we see that  $F_1(U_\mu \bar{U}) \in SU(2)$ . The same results holds true for  $F_2$  and  $F_3$ .

With this definition of  $a_1$ , the functional Eq. 5.4 we are seeking to maximise evaluates to

$$\text{Re Tr}(F_1(U_\mu \bar{U})^\dagger U_\mu \bar{U}) = 2k_1 + \text{Re}((U_\mu \bar{U})_{33}) . \quad (5.7)$$

The proof of this is given in Appendix E. By the matrix structure of  $F_1(V)$  it is apparent that  $\text{Re}(U_\mu \bar{U})_{33}$  is invariant under pre-multiplication by  $a_1$ , so it is clear that Eq. 5.7 represents the maximum attainable value for this form of  $U_\mu^{(1)}$ . Similarly, we let  $a_2 = F_2(U_\mu \bar{U})^\dagger$  and  $a_3 = F_3(U_\mu \bar{U})^\dagger$  to obtain the final value of  $U'_\mu$  according to Eq. 5.5. The above procedure is repeated over all three  $SU(2)$  subgroups 12 times per lattice link to effectively minimise the local action. One sweep of cooling then constitutes applying this procedure to every link on the lattice.

As detailed in Ref. [89], this process can be thought of as locally minimising the Wilson action of the three  $SU(2)$  subgroups, which collectively minimises the Wilson action of the full  $SU(3)$  link. It is then simple to extend this procedure to different actions by expanding the size and shape of the staples considered in the construction

of  $\bar{U}$ . As all of the quantities utilised in the cooling procedure are gauge invariant, cooling can be performed in any gauge to arrive at the same cooled configuration. Cooling also maintains the Boltzmann distribution of the lattice links [91], indicating that the new links can be considered a thermalised distribution. However, cooling is not a gauge transformation, and as such it represents a deviation from the original physical configuration. We therefore need to be careful when selecting the action used for the cooling routine to ensure that we are not removing the physics that we are interested in. To best study instantons and topological charge on a periodic lattice, it has been shown that a  $\mathcal{O}(a^4)$  three-loop improved action is most suitable [93]. This choice of action combines both computational efficiency with an effective stabilisation of instantons and an accurate preservation of the topological charge under repeated cooling sweeps. This action is dubbed a ‘three-loop’ action as it consists of a linear combination of  $1 \times 1$ ,  $2 \times 2$  and  $3 \times 3$  Wilson loops.

### 5.1.2 Over-Improved Smearing

Despite the accurate results obtained from cooled lattice configurations, cooling presents certain computational inefficiencies. Given that the staples,  $\bar{U}_\alpha$  must remain constant while updating a given link  $U_\mu$ , there are limitations to how parallelised the algorithm can be, especially for larger combinations of loops such as those used in the chosen three-loop improved action. To avoid these issues, a different type of smoothing was developed, known as ‘smearing’. Rather than locally minimising the action by direct substitution of each link, the initial APE smearing [94, 95] routine replaces each link with a weighted average of its nearest neighbours, according to

$$U' = (1 - \alpha) U_\mu + \frac{\alpha}{6} \bar{U}^\dagger, \quad (5.8)$$

where  $\bar{U}$  is the sum of the staples given in Eq. 5.3 and  $\alpha$  is some weighting parameter. However, as stated in the previous section, a linear combination of  $SU(3)$  matrices is not necessarily in  $SU(3)$ , so APE smearing is dependent on a choice of projection into the  $SU(3)$  group. To remove the need for this projection step, the method of stout-link smearing was developed [96].

We will first develop the stout-link smearing algorithm, then extend this to the over-improved stout-link smearing employed in this research. To begin, we define

$$\Sigma_\mu = \rho_{\text{sm}} (U_\mu \bar{U})^\dagger, \quad (5.9)$$

where  $\rho_{\text{sm}}$  is a smearing constant chosen to remain fixed for all lattice sites and  $\bar{U}$  is the sum of the relevant staples depending on the choice of action. Using this definition we construct

$$Q_\mu = \frac{i}{2} (\Sigma_\mu^\dagger - \Sigma_\mu) - \frac{i}{6} \text{Tr} (\Sigma_\mu^\dagger - \Sigma_\mu) I. \quad (5.10)$$

By construction,  $Q_\mu$  is Hermitian ( $Q_\mu = Q_\mu^\dagger$ ) and traceless, so it belongs to the  $SU(3)$  Lie algebra. It can therefore be exponentiated to obtain an element of  $SU(3)$ . We then define the new smeared link by

$$U'_\mu = \exp(iQ_\mu) U_\mu. \quad (5.11)$$

This definition effectively corresponds to a complex sum of neighbouring link combinations, however it has numerically been demonstrated to give similar results to the previous APE smearing technique, provided that the smearing parameter  $\rho_{\text{sm}}$  is selected appropriately [96]. For this work, we choose  $\rho_{\text{sm}} = 0.06$  [79]. As in the case of cooling, the choice of staples used to define  $\bar{U}$  has significant impact on the behaviour of topological objects under smearing. To this end, work has been done to tune the smearing algorithm so that it preserves instanton-like objects under repeated smearing sweeps, leading to the development of over-improved stoutlink smearing [79].

To quantitatively measure the effect of smearing on topological objects, it is common to calculate the instanton action in terms of the instanton radius. The error terms in the instanton action then give an indication of how the instanton radius will change as the action decreases under smearing. If the Baker-Campbell-Hausdorff plaquette expansion given in Appendix B is instead truncated at  $\mathcal{O}(a^4)$  rather than  $\mathcal{O}(a^2)$ , the Wilson action becomes [97]

$$\mathcal{S}_W = a^4 \sum_x \sum_{\mu, \nu} \text{Tr} \left[ \frac{1}{2} F_{\mu\nu}^2 + \frac{a^2}{24} \left\{ (D_\mu F_{\mu\nu}(x))^2 + (D_\nu F_{\mu\nu}(x))^2 \right\} + \mathcal{O}(a^4) \right]. \quad (5.12)$$

Substituting in the instanton potential (Eq. 3.39) and field strength tensor (Eq. 3.42), we find that the Wilson action goes like

$$S_W^{\text{Inst}} = \frac{8\pi^2}{g^2} \left\{ 1 - \frac{1}{5} \left( \frac{a}{\rho} \right)^2 + \mathcal{O} \left( \frac{a}{\rho} \right)^4 \right\}, \quad (5.13)$$

where  $\rho$  is the instanton radius. We note then that as the Wilson action is minimised, the  $-\frac{1}{5} \left( \frac{a}{\rho} \right)^2$  term must become increasingly negative, implying that the instanton

radius decreases. This is precisely the effect we wish to avoid, as the instanton radius will shrink under smearing to the point where the instanton-like objects ‘fall through’ the lattice as  $\rho \rightarrow a$ . A similar calculation can be done for the Lüscher and Weisz action, showing that [97]

$$S_{\text{LW}}^{\text{Inst}} = \frac{8\pi^2}{g^2} \left\{ 1 - \frac{17}{210} \left( \frac{a}{\rho} \right)^4 + \mathcal{O} \left( \frac{a}{\rho} \right)^6 \right\}. \quad (5.14)$$

In both cases, the leading error term is negative, resulting in a suppression of the instanton radius. To counteract this, we modify the action by taking a linear combination of  $S_{\text{W}}$  and  $S_{\text{LW}}$  and introducing a parameter  $\epsilon$  that interpolates between them [79]. This modified action is given as

$$S(\epsilon) = \beta \sum_x \sum_{\mu>\nu} \left[ \frac{5-2\epsilon}{3} (1 - P_{\mu\nu}(x)) - \frac{1-\epsilon}{12} ((1 - R_{\mu\nu}(x)) + (1 - R_{\nu\mu}(x))) \right]. \quad (5.15)$$

We see that  $S(1) = S_{\text{W}}$  and  $S(0) = S_{\text{LW}}$ . Expanding  $S(\epsilon)$  in terms of the instanton solution, we have

$$S^{\text{Inst}}(\epsilon) = \frac{8\pi^2}{g^2} \left[ 1 - \frac{\epsilon}{5} \left( \frac{a}{\rho} \right)^2 + \frac{14\epsilon - 17}{210} \left( \frac{a}{\rho} \right)^4 + \mathcal{O} \left( \frac{a}{\rho} \right)^6 \right]. \quad (5.16)$$

The parameter  $\epsilon$  can now be tuned so as to preserve instantons under smearing. The natural choice may be to follow Ref. [97] and set  $\epsilon = -1$  to ensure that the leading error term is positive. However, one then runs the risk of unphysically growing the instanton size such that it annihilates with anti-instantons present on the lattice. Furthermore, we wish to smear such that the instantons are minimally distorted as they undergo the smearing process. To this end, we follow the results of Ref. [79] and choose  $\epsilon = -0.25$ . We then choose the corresponding staple parameter  $\bar{U}$  to be the sum over the  $1 \times 1$  and  $(2 \times 1) + (1 \times 2)$  loops with  $U_\mu$  omitted, with respective weightings  $\frac{5-2\epsilon}{3}$  and  $-\frac{1-\epsilon}{12}$ . With this definition of the smearing action, we can now utilise smearing to filter out the short distance physics, isolating the topological objects of interest.

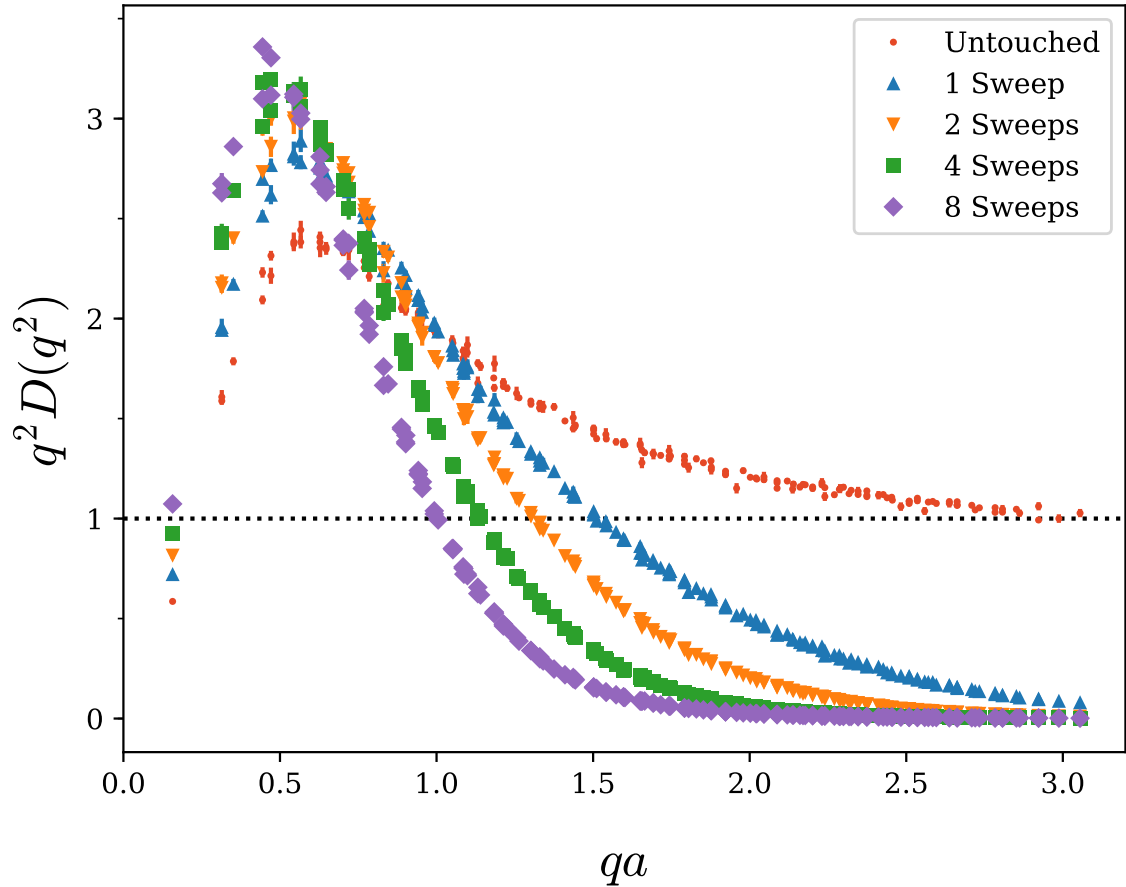


Fig. 5.2 Comparison of the gluon propagator on the untouched configurations after cooling. For clarity we have selected a sample of sweeps between 1 and 8.

## 5.2 Results from the Gluon Propagator

Making use of the smoothing methods defined above, we now wish to compare their effect on the gluon propagator. Summarising the previous sections, we employ  $\mathcal{O}(a^4)$ -improved three-loop cooling and over-improved stoutlink smearing with smearing parameters  $\rho_{\text{sm}} = 0.06$  and  $\epsilon = -0.25$ . We first plot the untouched propagator after 0, 1, 2, 4 and 8 sweeps of cooling in Fig. 5.2. In gauge fixing to Landau gauge, each sweep has been preconditioned by the Landau gauge transformation of the prior sweep in descending order (i.e. the transformation for sweep 10 preconditions sweep 9). This preconditioning is done to ensure that the Landau gauge functional is near the same local minima for each cooling sweep. We observe the expected removal of short distance fluctuations that is typical of smoothing, resulting in a suppressed propagator at large  $q$ . This is complemented by an amplification in the infra-red region which can be

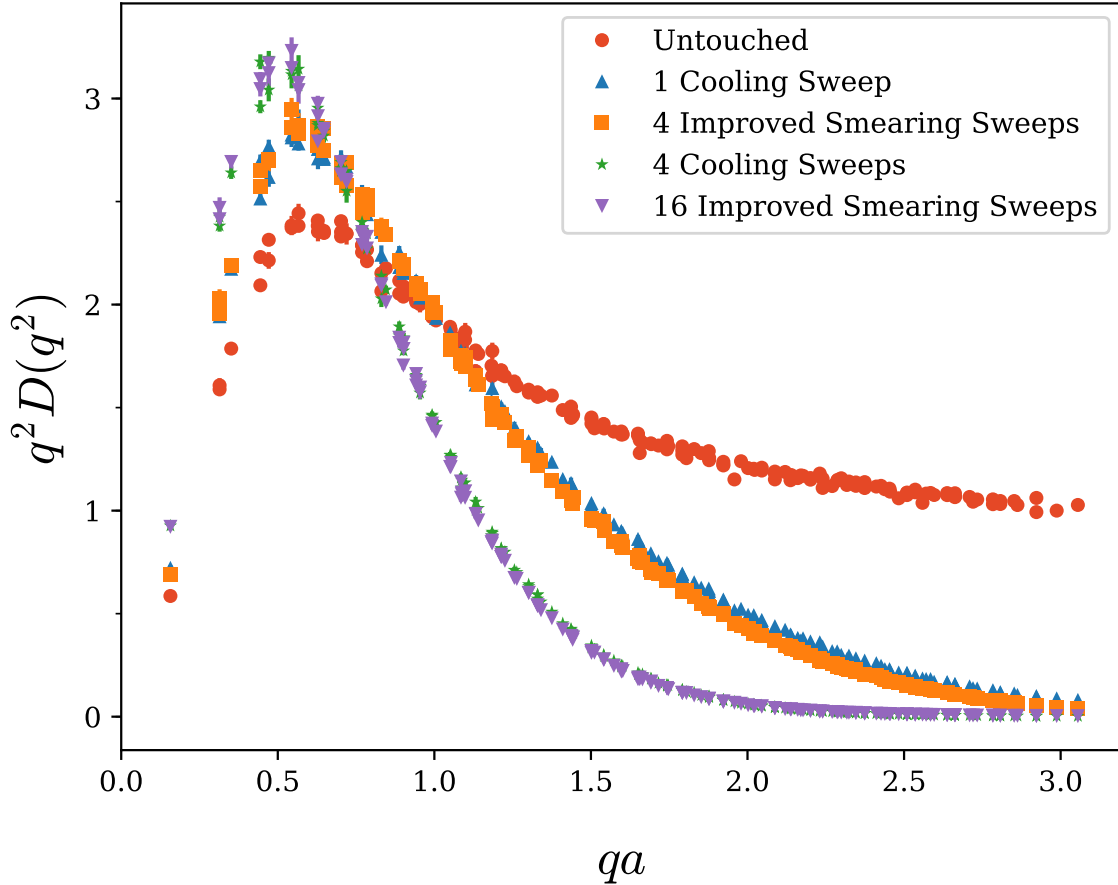


Fig. 5.3 The gluon propagator after cooling or improved smearing. We see that the shape of the plot changes minimally between the smoothing routines. However cooling requires fewer sweeps to produce the same effect when compared to smearing.

attributed to the increase in low momentum modes arising from the smoothing of the gauge fields.

To compare the effects of cooling and over-improved smearing, the untouched gluon propagator is plotted in Fig. 5.3 after either over-improved smearing or cooling. By comparing the smeared and cooled propagator we can see that cooling has a more rapid effect, related to the well-known fast removal of action from the lattice. The qualitative shape of the propagator remains the same however, and it can be seen that, for example, 4 smearing sweeps produces a propagator remarkably similar to 1 cooling sweep. More generally, we observe that in regards to the shape of the propagator,  $n_{\text{sm}} \approx 4 n_{\text{cool}}$ . Following the observation made in Ref. [98] that the number of over-improved stoutlink

smearing sweeps is related to the gradient flow time by

$$t \approx \rho n_{\text{sm}} , \quad (5.17)$$

we deduce that the relationship between gradient flow time and cooling is

$$t \approx 0.24 n_{\text{cool}} . \quad (5.18)$$

It is well understood that smoothing alters the vortex background, and based on previous work [39, 44, 71] we anticipate that the vortices identified on smoothed configurations would differ to those identified on the unsmoothed configurations. We therefore perform vortex identification only on the original configurations, with smoothing then being performed independently on the untouched, vortex-only and vortex-removed configurations. We choose to use cooling as the smoothing algorithm for the results presented in this research, however it is worth noting that similar results can be obtained with the use of over-improved smearing.

# Chapter 6

## Gluon Propagator on Vortex-Modified Backgrounds

### 6.1 Preliminary Results

Here we present the results from the gluon propagator, calculated according to method outlined in Chapter 4, on our three vortex-modified configurations. Calculating the scalar propagator on untouched, vortex-removed and vortex only configurations gives the results illustrated in Fig. 6.1. To make contact with the tree-level propagator at large  $q^2$ , we renormalise such that  $q^2 D(q^2) = 1$  for  $qa = 3.0$  on the original configurations, and apply this same renormalisation factor to the vortex removed and vortex only propagators. The vortex removed configurations display the expected behaviour, with vortex removal corresponding to significant infrared suppression of the propagator when compared to the untouched propagator, in agreement with the results of Ref. [47]. The increased roughness of the gauge fields after vortex removal is evidenced by the enhancement of the propagator at large  $q$ . This reflects the increase in short-distance fluctuations that have been introduced to the gauge fields by the vortex removal procedure.

It is interesting to note that the vortex only propagator retains approximately two thirds of the untouched propagator's peak strength. This is comparable to previous work showing partial recovery of the string tension on vortex only configurations [39, 41, 46, 99]. Despite only recovering a portion of the original strength, the infrared peak is still considerably greater than the peak observed in the vortex removed propagator. The loss of strength is most likely in part because of the known imperfections in the vortex identification algorithm (see Sec. 3.2.1) that results in

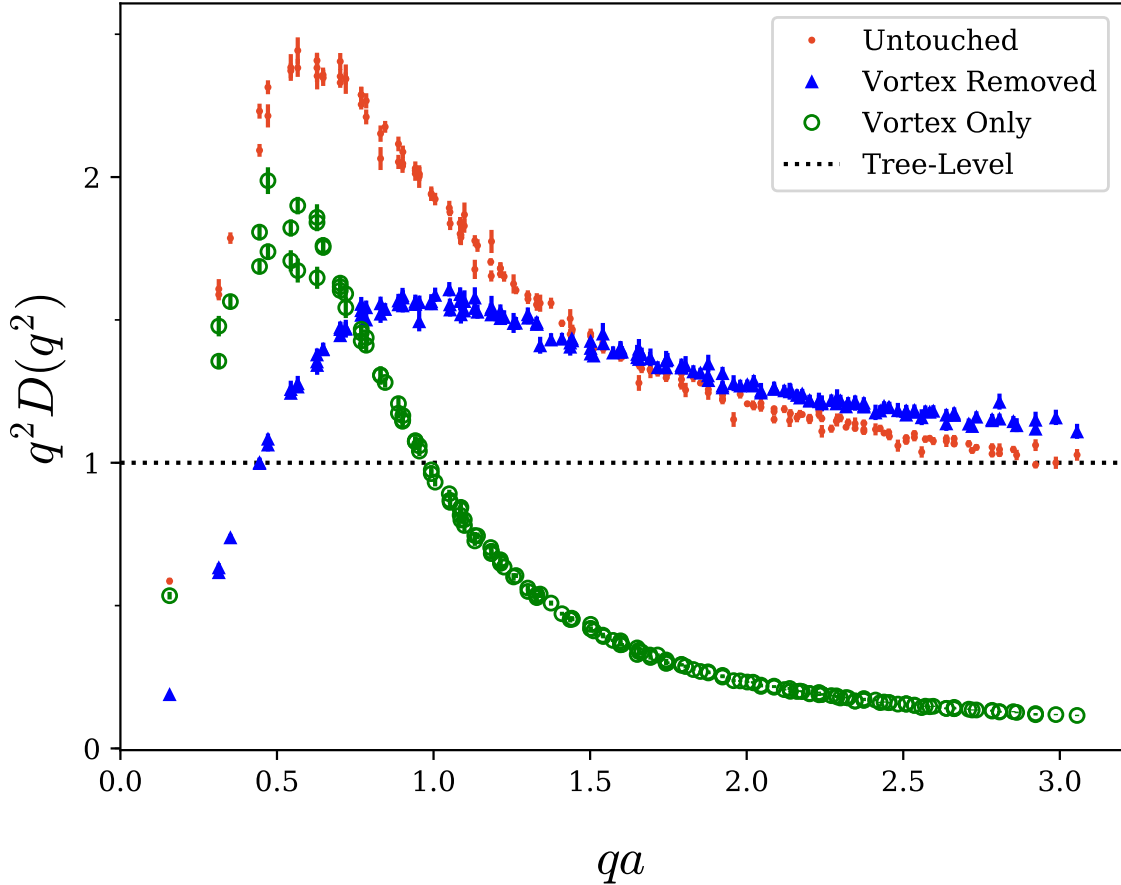


Fig. 6.1 The gluon propagator calculated from the original untouched (red dots), shown with the vortex removed (blue triangles) and vortex only (green open circles) results. Here, the renormalisation factor for the vortex removed and vortex only propagators is chosen to be the same as for the untouched propagator.

some vortex matter remaining in the vortex removed configurations. The vortex only configurations also exhibit a loss of short range strength, due to the absence of the high frequency modes that are instead contained within the vortex removed field.

If we sum the vortex only and vortex removed propagators and independently renormalise such that  $q^2 D(q^2) = 1$  at  $qa = 3.0$ , we obtain the result shown in Fig. 6.2. Here we observe agreement between the untouched and summed propagators. This indicates that vortex modification effectively partitions the lattice configuration into short range physics on the vortex removed configurations and long range physics on the vortex only configurations, up to errors in the vortex identification procedure.

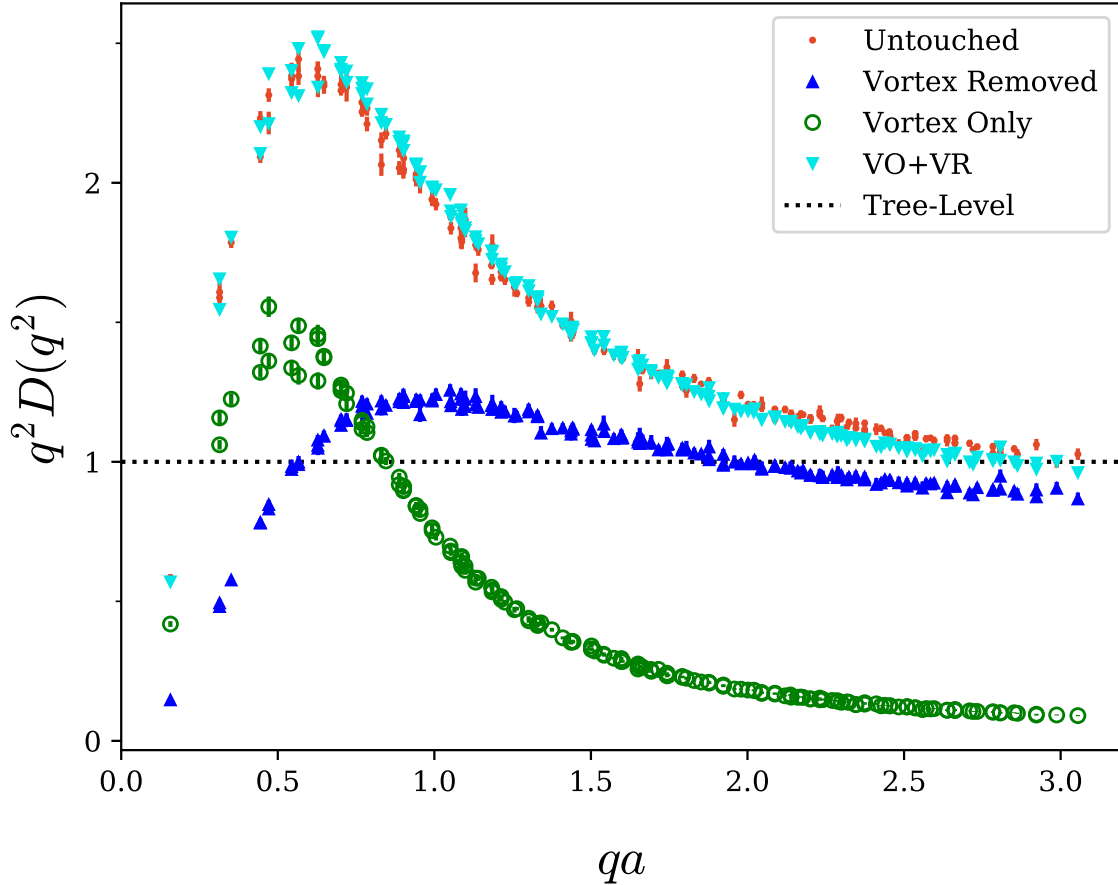


Fig. 6.2 The gluon propagator from the original untouched ensemble as in Fig. 6.1, now shown with the independently renormalised sum (cyan triangles) of the vortex removed and vortex only propagators. The two vortex modified propagators are also shown, but here their renormalisation factor is chosen to be the same as for the summed propagator.

### 6.1.1 Partitioning

This partitioning is expected if the vortex removed and vortex only configurations are orthogonal. To see how this behaviour emerges, suppose that we can decompose the gluon field  $A_\mu$  into two independent fields as follows

$$A_\mu(p) = B_\mu(p) + C_\mu(p). \quad (6.1)$$

In the context of this work, we associate  $B_\mu$  with the background field of short-range gluon fluctuations and  $C_\mu$  with the centre vortex field. Note also that if  $B$  and  $C$  are in Landau gauge then so is  $A$ . Using this partitioning it follows that the gluon propagator

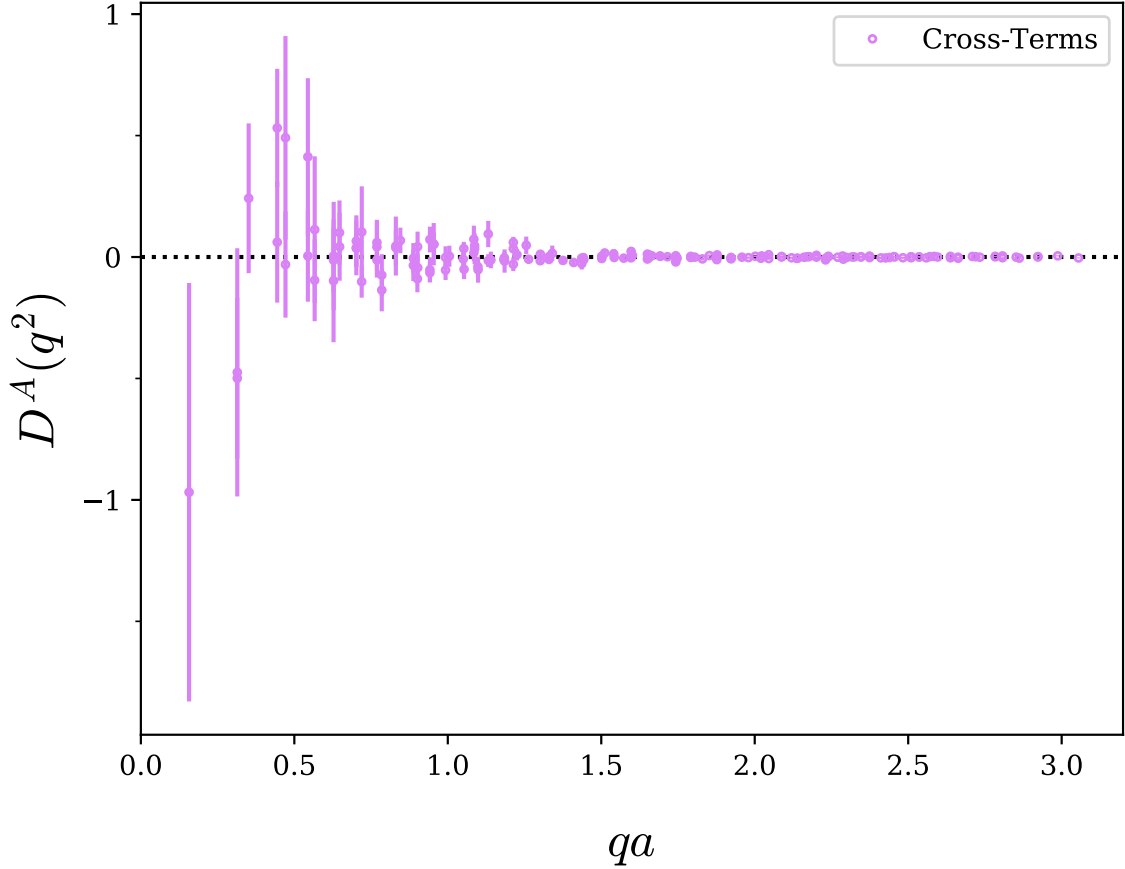


Fig. 6.3 Calculation of the cross-terms arising from Eq. 6.2

for  $A$  can be written as the sum of the respective gluon propagators for  $B$  and  $C$ ,

$$\begin{aligned}
 D_{\mu\nu}^A(p) &= \frac{1}{V} \langle A_\mu(p) A_\nu(-p) \rangle \\
 &= \frac{1}{V} \left( \langle B_\mu(p) B_\nu(-p) \rangle + \langle C_\mu(p) C_\nu(-p) \rangle \right. \\
 &\quad \left. + \langle B_\mu(p) C_\nu(-p) + C_\mu(p) B_\nu(-p) \rangle \right) \\
 &= D_{\mu\nu}^B(p) + D_{\mu\nu}^C(p),
 \end{aligned} \tag{6.2}$$

where we have made use of the fact that  $B$  and  $C$  represent orthogonal degrees of freedom in the gauge field and hence in the ensemble average the cross-correlations should vanish. These cross-correlations are explicitly calculated by evaluating

$$D_{\text{cross-terms}}(p^2) = \frac{2}{3(n_c^2 - 1)V} \langle \text{Tr}(B_\mu(p)C_\mu(-p) + C_\mu(p)B_\mu(-p)) \rangle, \tag{6.3}$$

analogous to the scalar gluon propagator derived in Chapter 4. The results of this calculation are shown in Fig. 6.3. As can be clearly seen, in the ensemble average Eq. 6.3 vanishes, indicating that the vortex only and vortex removed configurations truly do represent orthogonal degrees of freedom.

To elucidate the connection to the unitary formulation of the lattice gauge links, we suppose that we can transform  $A$  to an “ideal centre gauge” such that in lattice units the field  $C$  consists purely of centre phases,

$$C_\mu(x) = k \frac{2\pi}{3} I, \quad k \in \{-1, 0, +1\}. \quad (6.4)$$

As  $A = B + C$  it immediately follows that we can write

$$U_\mu(x) = e^{iB_\mu(x+\hat{\mu}/2)} e^{iC_\mu(x+\hat{\mu}/2)}, \quad (6.5)$$

noting that in our ideal centre gauge  $[B, C] = 0$  so the Baker-Campbell-Haussdorff relation is trivial. Identifying

$$Z_\mu(x) = e^{iC_\mu(x+\hat{\mu}/2)} \quad (6.6)$$

as the vortex-projected field, and

$$R_\mu(x) = e^{iB_\mu(x+\hat{\mu}/2)} \quad (6.7)$$

as the background remainder field we thus recover the decomposition of the links used herein,

$$U_\mu(x) = Z_\mu(x) \cdot R_\mu(x). \quad (6.8)$$

In practise, on the lattice the maximal centre gauge fixing that is implemented will differ from the ideal centre gauge postulated here due to apparent numerical difficulties in simultaneously identifying all vortex matter within an  $SU(3)$  gauge field. What this means is that the projected field  $Z$  may not capture all of the vortex matter such that there is some non-trivial topological structures that remain in the background field  $R$ . The infrared enhancement in the vortex removed results in Fig. 6.1 suggests this is the case.

### 6.1.2 Renormalisation

In Fig. 6.2 it proved necessary to independently renormalise the untouched and summed propagators such that they agree at  $qa = 3.0$ . The necessity of this renormalisation is worth discussing, as it is important to motivate why comparison between the original and reconstructed propagators is valid. To do this, it is beneficial to first consider the renormalised gluon propagator in the continuum. The renormalised propagator at any loop order,  $D_R^C(q^2)$  can be related to the bare propagator,  $D^C(q^2)$  via the relationship

$$D^C(q^2) = Z_3^C D_R^C(q^2). \quad (6.9)$$

Typically  $Z_3^C$  and  $D^C(q)$  are infinite, whereas  $D_R^C(q)$  is finite. The renormalised propagator is not independent of the renormalisation scheme, and the expression for  $Z_3^C$  depends on the renormalisation scheme employed. For example, in the minimal subtraction (MS) scheme at one-loop order with no quark fields,  $Z_3^C = 1 + \frac{5g^2}{8\pi^2\epsilon}$  [3], where the quantity  $\epsilon$  is introduced during the analytic continuation to  $d = 4 - \epsilon$  dimensions as part of the dimensional regularisation procedure. However, regardless of the chosen renormalisation scheme, the renormalised propagator can always be expressed in the form shown in Eq. 6.9 [100].

On the lattice, we can explicitly calculate the now finite bare dimensionless propagator  $D^L(q^2)$ , as the lattice introduces an explicit momentum cutoff of  $\frac{\pi}{a}$ . In the language of the continuum, this can be thought of as an approximation of the continuum bare propagator to all loop orders. Similarly, the lattice renormalisation constant  $Z_3(\mu, a)$  is also finite. On the lattice, Eq. 6.9 becomes

$$a^2 D^L(q^2) = Z_3(\mu, a) D_R(q^2), \quad (6.10)$$

where the  $a^2$  factor restores the dimensionality of the left-hand side of the equation. Despite the finiteness of  $D^L(q^2)$  and  $Z_3(\mu, a)$ , it is still necessary to enforce a renormalisation scheme to be able to draw meaningful comparisons between propagators. As such, we employ the momentum space subtraction (MOM) scheme [84, 101, 102], which requires that for some sufficiently large  $\mu$

$$D_R(q^2) \Big|_{q^2=\mu^2} = \frac{1}{\mu^2}. \quad (6.11)$$

This sets the value of the renormalisation constant to be

$$Z_3(\mu, a) = a^2 \mu^2 D^L(\mu^2), \quad (6.12)$$

such that

$$D_R(q^2) = \frac{D^L(q^2)}{\mu^2 D^L(\mu^2)}. \quad (6.13)$$

This renormalised propagator is what we plot in e.g. Fig. 6.2. The value of  $\mu$  is arbitrary, however it is necessary that it is sufficiently large such that it is outside the infrared region where the gluon propagator exhibits substantial deviation from tree-level behaviour. Furthermore,  $\mu$  must be away from the momentum cutoff, as the renormalisation constant is only independent of the cutoff in the limit that the cutoff tends towards infinity [84, 103]. Given the momentum range of  $qa \in [0, 4.6]$ , arising from the momentum variables described in Sec. 4.2, a choice of  $\mu = 3.0$  satisfies both conditions. Additionally, it also falls below the maximum momentum of  $qa = 3.06$  imposed by the momentum half-cut described in Sec. 4.3. Once the renormalisation scheme has been imposed, it is then possible to connect the lattice results with those obtained from perturbation theory by connecting the renormalisation constant with those obtained from the MS or modified minimal subtraction ( $\overline{\text{MS}}$ ) schemes.

This discussion of renormalisation has motivated why it is acceptable to compare the untouched and summed propagators in Fig. 6.2; it is the renormalised propagator, not the bare propagator, that carries the physical meaning. Hence, the fact that the untouched and summed propagators agree after renormalisation is an important result indicating the effective partitioning of the gluon propagator under vortex modification. The final point worth discussing is the renormalisation applied to the vortex only and vortex removed propagators. Given that we don't have an *a priori* expectation of the tree-level behaviour, imposing the MOM condition lacks meaning. Instead, to facilitate comparisons, we make use of the original  $Z_3(\mu, a)$  obtained for the untouched propagator unless specified otherwise. Maintaining this consistency is sufficient to comment on the qualitative shape of the propagator, which is the most significant point of interest in this research.

## 6.2 Impact of Cooling

After performing 10 sweeps of cooling on the untouched, vortex-removed and vortex-only ensembles, we obtain the results shown in Fig. 6.4. As is typical of cooling, the

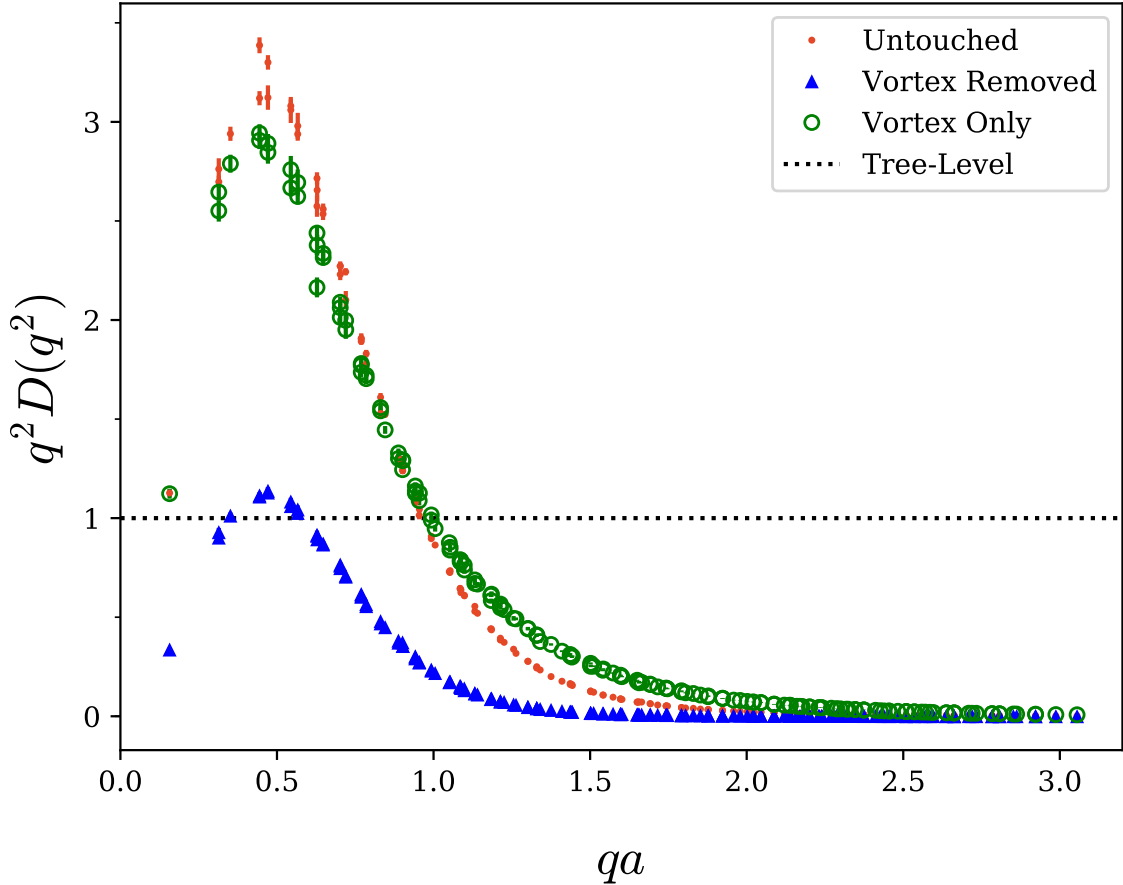


Fig. 6.4 The gluon propagator calculated on the three ensembles after 10 sweeps of cooling. We now observe an improved agreement between the untouched and vortex only propagators.

removal of short range structures means that all three ensembles tend to zero as  $q \rightarrow \infty$ . There is now a noticeable improvement in the agreement between the untouched and vortex only configurations; however there is still a difference present, especially in the  $qa \approx 0.5$  and  $qa \approx 1.5$  regions.

We perform the same analysis of the vortex only propagator under cooling as performed in Sec. 5.2 on the untouched propagator. Once again in gauge fixing, each sweep is preconditioned by the Landau gauge transformation of the previous sweep in descending order. The result of this analysis is shown in Fig. 6.5. This figure shows a similar change in the vortex only propagator when compared to the untouched propagator in Fig. 5.2, with an enhancement in the infrared and suppression in the UV modes. The UV suppression is less noticeable in this case due to the prior removal

of short range effects brought about by the vortex identification.

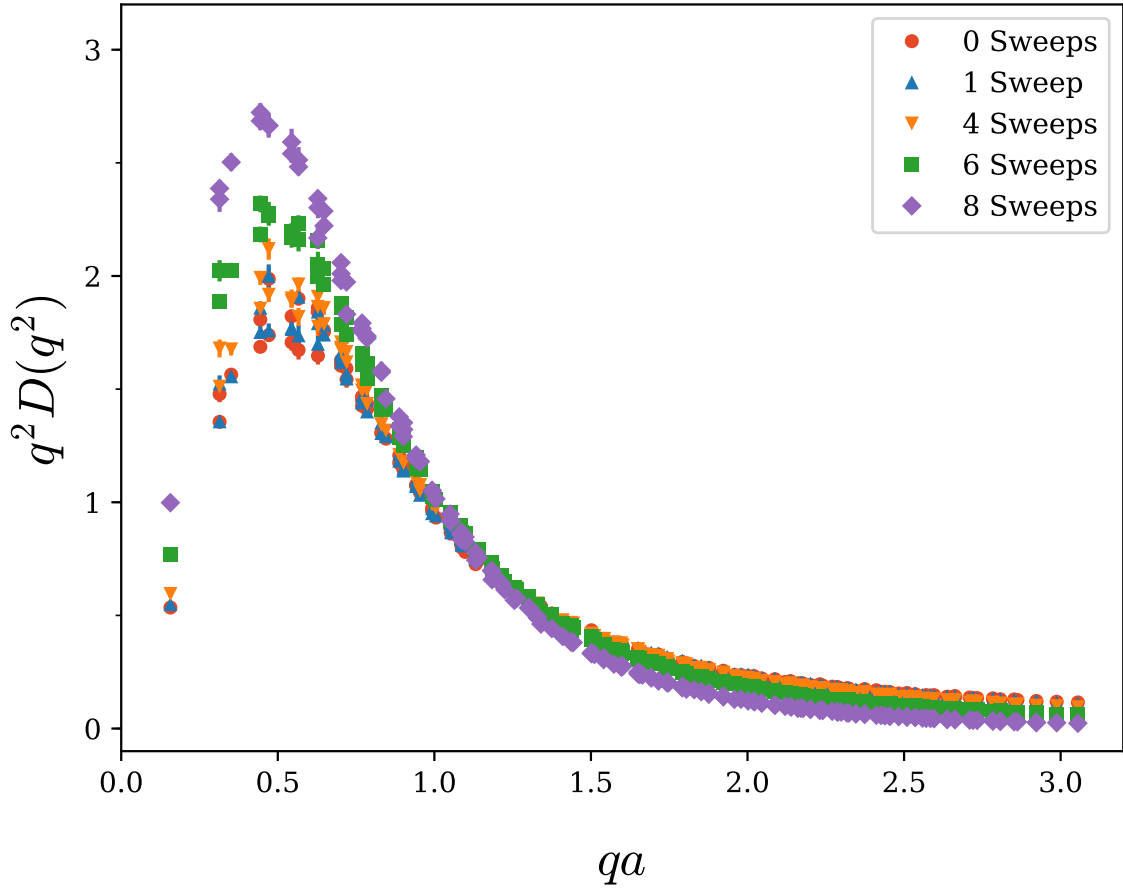


Fig. 6.5 The vortex only propagator after different sweeps of cooling. A trend similar to Fig. 5.2 is observed, with enhancement in the infrared and suppression in the UV region.

We observe that the vortex only and untouched propagators in Fig. 6.4 resemble the gluon propagator under a differing number of sweeps of cooling, as shown in Fig. 5.2 and Fig. 6.5. The vortex only propagator has a peak that sits below the untouched propagator, and the untouched propagator is further suppressed in the  $qa \approx 1.5$  region. Following the trend in Fig. 5.2 and Fig. 6.5, this indicates that further cooling on the vortex only propagator would align it with the untouched propagator. This follows from an understanding that the vortex-only configurations are initially much rougher than their untouched counterparts [40], and should therefore require additional cooling to obtain agreement with the untouched configurations.

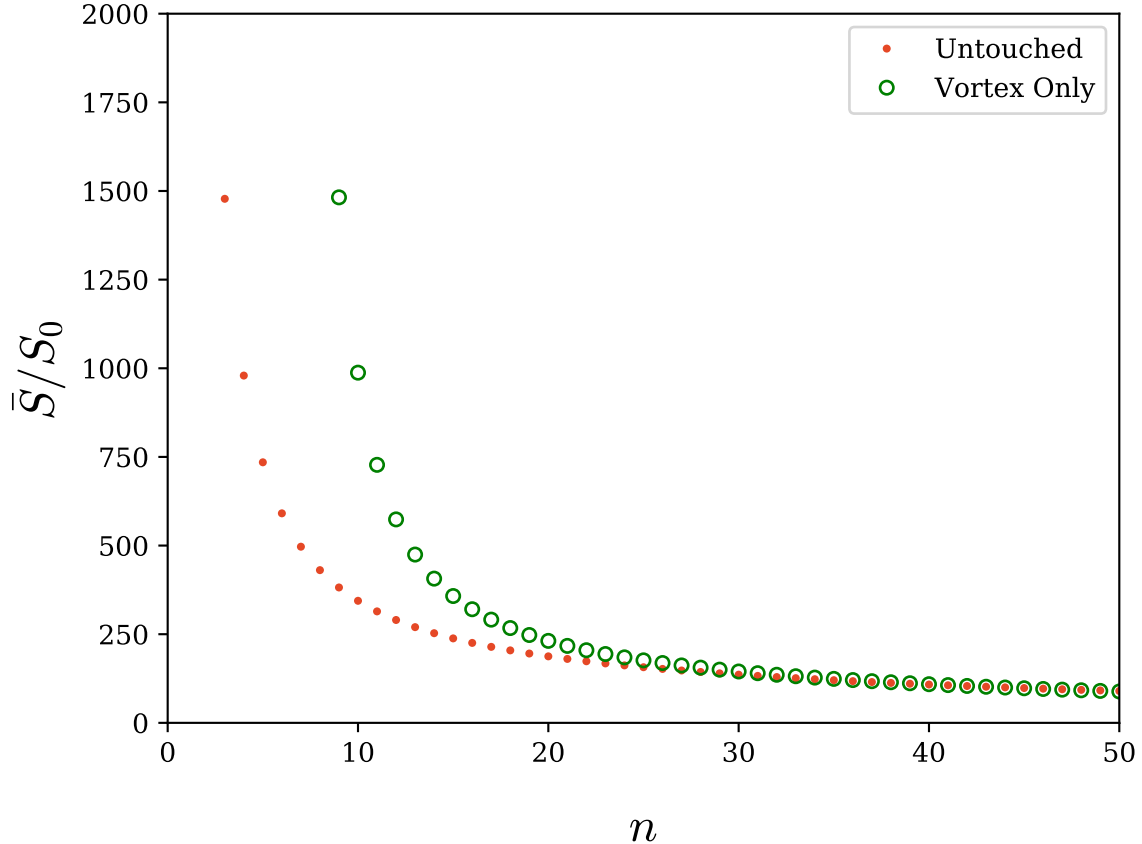


Fig. 6.6 The average action calculated on the untouched and vortex-only configurations as a function of cooling sweeps,  $n$ . The vortex only configurations are initially rougher than the untouched, as evidenced by the higher average action.

Table 6.1 Comparison of the number of cooling sweeps on the untouched ( $n_U$ ) and vortex only ( $n_{VO}$ ) configurations required to match the average action.

$n_U$	$\bar{S}/S_0$	$n_{VO}$	$\bar{S}/S_0$
5	734.83	11	727.67
10	344.22	15	357.68
15	238.21	20	231.19
20	187.55	24	184.68
25	156.92	28	155.72
30	135.91	32	135.61
35	120.29	36	120.66
40	107.08	40	109.02

We take the average  $\mathcal{O}(a^4)$  three-loop improved action of the lattice divided by the single instanton action  $S_0 = \frac{8\pi^2}{g^2}$ , denoted  $\bar{S}/S_0$ , to be a measure of roughness.

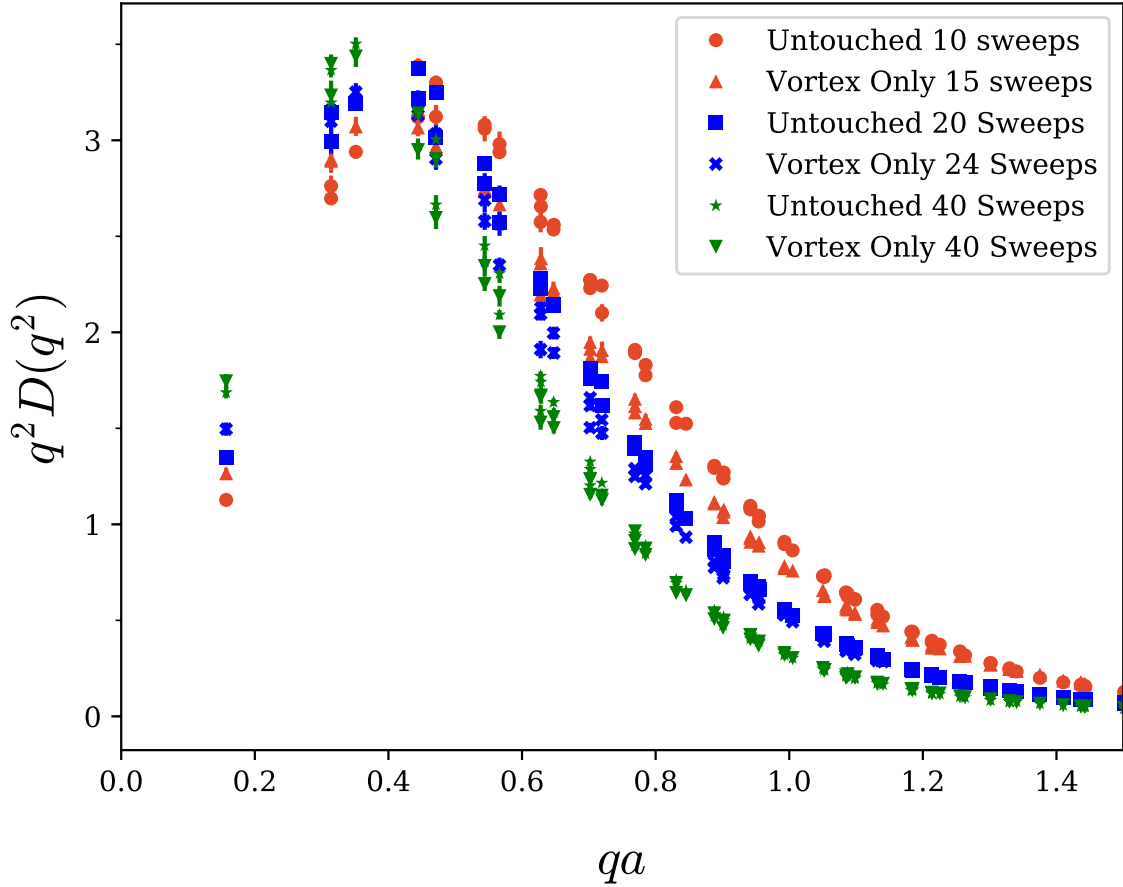


Fig. 6.7 Comparison of the gluon propagator on the untouched and vortex only configurations after tuning the number of cooling sweeps to best match the average plaquette action. This procedure gives a much better agreement in the shape of the gluon propagator from the two configurations.

We observe that for  $n < 20$  cooling sweeps the vortex-only configurations have a significantly higher action than their untouched counterparts after the same number of sweeps of cooling, as illustrated in Fig. 6.6. We therefore seek to find the number of sweeps required to best match the action between the vortex-only and untouched configurations. The results of this procedure are shown in Table 6.1. If we now plot these matched configurations, we obtain the results shown in Fig. 6.7. Here we have truncated the plot at large  $qa$  to better show the agreement in the mid- $qa$  region. By matching the actions as closely as possible with an integer number of cooling sweeps, we see that there is a better agreement between the untouched and vortex-only gluon propagators.

## 6.3 Summary

The results presented above concur with the now significant body of evidence that centre vortices contain the essential degrees of freedom of the Yang-Mills vacuum, such that the application of smoothing enables the recreation of the major features of QCD [39–41, 44, 104]. We have shown that vortex identification partitions the gluon propagator into low and high momentum modes, with the vortex only configurations encapsulating the majority of the infrared strength. Cross-correlation between the vortex only and vortex removed propagators can be seen to vanish in the ensemble average. By cooling the configurations, we observe that the vortex only configurations are continuously suppressed, while the infrared peak in the untouched and vortex only propagator acquires better agreement. By tuning the number of cooling sweeps to best match the average action of the vortex only and untouched configurations, we can effectively match the gluon propagators obtained from each of these configurations.

Noting that sufficient smoothing of a vortex-only field generates a topological background of instanton-like objects, we can regard the thin centre vortices as the seeds of instantons. The smoothing process that is applied on the vortex-only configurations raises a question regarding the precise role of vortices in the restoration of the infrared propagator; is it simply the presence of (sufficiently smoothed) vortices or is it more indirectly the reformation of the instanton background? If we examine Fig. 6.4, we see that after the application of 10 sweeps of cooling the vortex-only propagator has the appropriate qualitative infrared behaviour. Comparing with previous work, in particular Fig. 7 within Ref. [39] (replicated in Fig. 6.8) which shows the typical distribution of the instanton radius against the topological charge at the centre, we can see that after only 10 sweeps of cooling the vortex-only distribution still deviates significantly from the ideal theoretical instanton relationship. This suggests that it is the smoothed centre vortices that are directly responsible for the infrared structure of the gluon propagator.

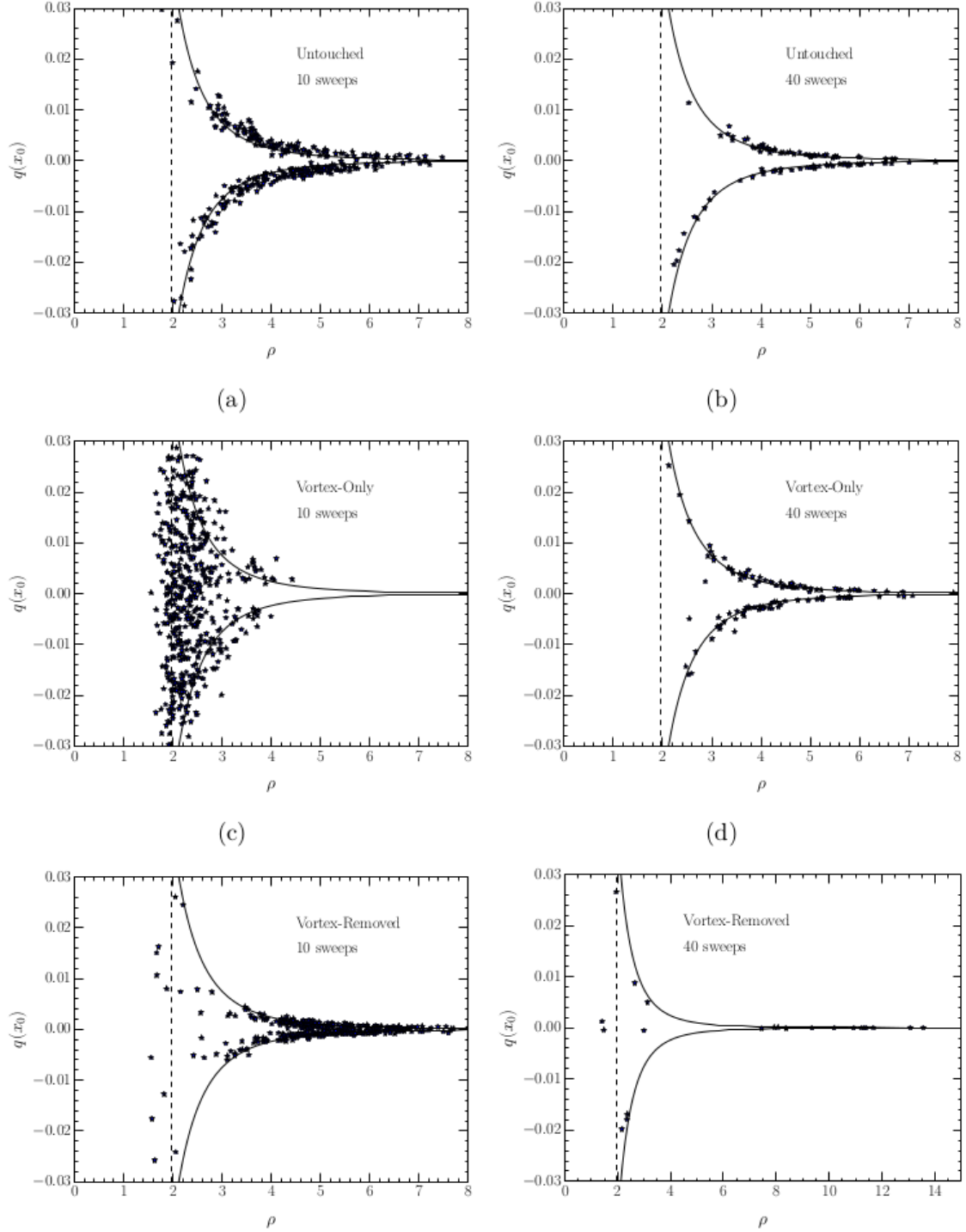


Fig. 6.8 The topological charge at the instanton centre,  $q(x_0)$ , is plotted against the instanton radius  $\rho$  for the vortex modified configurations under 10 and 40 sweeps of cooling. The solid line represents the theoretical distribution. These plots are acquired from Trewartha *et al.* [39].



# Chapter 7

## Centre Vortex Visualisations

In previous chapters we have motivated the significance of centre vortices in QCD through the calculation of the gluon propagator. Although we can predict many of the properties of vortices through calculation, these properties can also be explored through visualisations of the lattice. To this end, in this chapter we present a novel visualisation technique that allows us to view thin centre vortices on the lattice through the use of 3D models<sup>1</sup>. These models allow for a highly interactive exploration of the vortex structure of the QCD vacuum.

### 7.1 Space-Oriented Vortices

As the lattice is a four-dimensional hypercube, we visualise the centre vortices on a set of 3D slices. The choice of dimension to take slices along is irrelevant in Euclidean space, so we choose to take slices along the  $x$ -axis, resulting in  $N_x$  slices each with dimensions  $N_y \times N_z \times N_t$ . This choice of axis to slice along allows for the largest volume per slice. However, the transition between slices is most intuitively thought of as ‘stepping though time’, so we re-label our coordinates such that each slice is considered to be a snapshot at fixed  $t$ , with local coordinates  $(x, y, z)$ . Within each slice we can visualise all vortices associated with an  $x - y$ ,  $x - z$  or  $y - z$  plaquette by calculating  $P_{xy}(\mathbf{x})$ ,  $P_{yz}(\mathbf{x})$  and  $P_{zx}(\mathbf{x})$  for all  $\mathbf{x}$  in the slice. These vortices will be referred to as the ‘space-oriented’ vortices, as they are fixed in time. The plaquettes are evaluated on a centre projected configuration, so  $P_{\mu\nu} \in \{-1, 0, +1\}$ . For a  $+1$  vortex, a blue jet is plotted piercing the centre of the plaquette, and for a  $-1$  vortex a

---

<sup>1</sup>All 3D models have been generated using Advanced Visual Systems (AVS) Express Visualisation Edition, version 8.4.1.

red jet is plotted. The direction of the jet is set according to a right-hand rule, such that

- $P_{xy} = \pm 1 \implies \pm \hat{z}$  direction.
- $P_{yz} = \pm 1 \implies \pm \hat{x}$  direction.
- $P_{xz} = \pm 1 \implies \mp \hat{y}$  direction,

An example of this plotting convention is shown in Fig. 7.1.

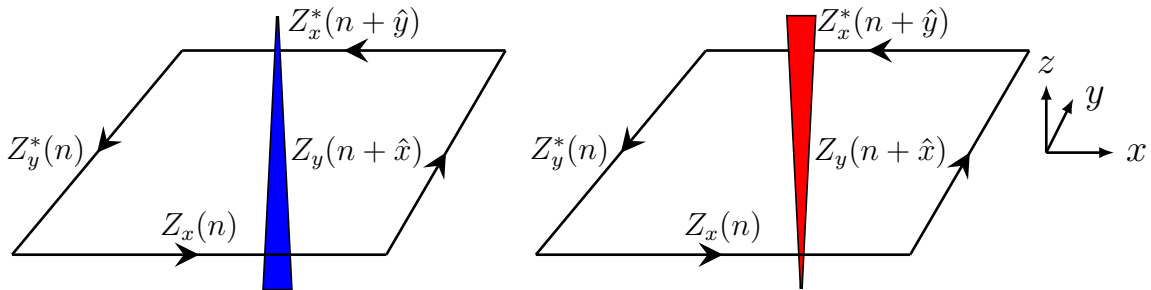


Fig. 7.1 An example of the plotting convention for vortices located within a 3D time slice. **Left:** A  $+1$  vortex in the  $+\hat{z}$  direction. **Right:** A  $-1$  vortex in the  $-\hat{z}$  direction.

The 3D slices for  $t = 1, 2$  with the space-oriented vortices plotted appear as in Figs. 7.2, 7.3. At first glance the vortex structure appears highly complex, and it is difficult to identify the significant features. As such, we make use of the 3D models to hone in and isolate the important features present in these slices. We present some of these features in Fig. 7.4.

It is an excellent sanity check to see that the vortices do indeed form closed lines, as they must to conserve the centre flux and satisfy the Bianchi identity [77, 105]. We also observe that with the exception of the  $1 \times 1$  vortex loops (see the middle image in Fig. 7.4) which can be readily attributed to incorrectly identified centre phases, the vortex loops are large and rarely form isolated loops within the 3D volume. This agrees with the observation made of  $SU(2)$  vortices in Refs. [66, 106] that below the critical deconfinement temperature,  $T_C$ , almost all vortices identified had the maximum possible extent. It will be the subject of future work to investigate whether as the temperature increases the  $SU(3)$  vortices begin to shrink and cease to percolate, indicating a transition to the deconfining phase.

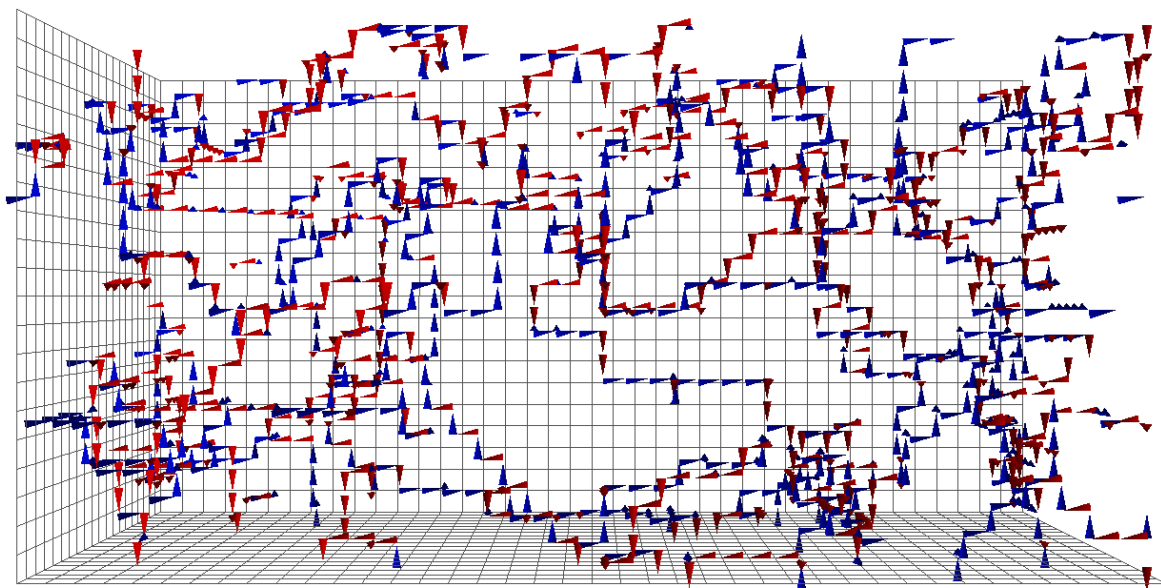


Fig. 7.2 The  $t = 1$  slice with all space-oriented vortices plotted.

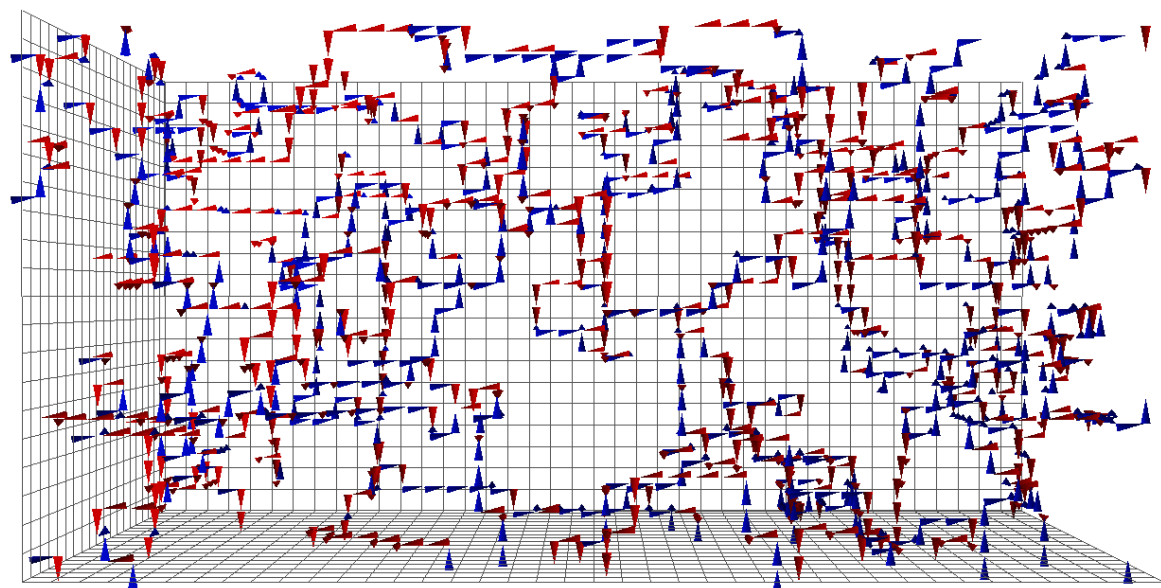


Fig. 7.3 The  $t = 2$  slice with all space-oriented vortices plotted.

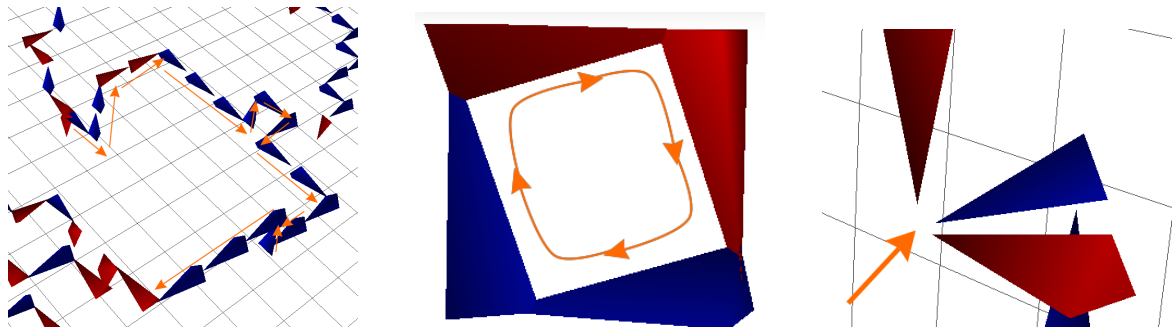


Fig. 7.4 **Left:** Vortices form continuous lines. Note that because of the lattice periodicity, these lines may wrap around to the opposite edge of the lattice. **Middle:** Vortices must form closed loops to conserve the vortex flux. **Right:**  $SU(3)$  vortices are capable of forming monopoles or branching points where three vortices emerge or converge at a single point.

The presence of branching/monopole points is of particular interest, as previous studies have primarily focussed on  $SU(2)$  theory which is free from these structures. This is because it is only in  $SU(3)$  (or more generally,  $SU(N)$  with  $N > 2$ ) that it is possible to conserve the centre flux at the intersection of 3 vortices, as shown in Fig. 7.5. It is clear from our visualisations that these points occur frequently in the confining phase, in agreement with the findings of Ref. [77]. The ambiguity between monopoles and branching points arises from the lack of definite orientation for the vortex line. As  $P_{\nu\mu} = P_{\mu\nu}^\dagger$ , the ordering by which the plaquette is calculated will invert the sign of the vortex, and as such the choice of ordering can change a monopole into a branching point, or vice-versa. The lack of definite orientation for vortices is an important property, as it permits non-vanishing topological charge, and is indeed a key property of the vortex model [107, 108]. The presence of these points may also enforce an integer topological charge when they are considered to be ‘nexus’ solutions, as described in Refs. [109, 110].

## 7.2 Time-Oriented Vortices

For each link in a given 3D slice there are two additional plaquettes that lie in the  $x_i - t$  plane, pointing in the positive and negative time directions. Vortices associated with time-oriented plaquettes contain information of how the line-like vortices evolve with time, or equivalently, how the vortex surfaces appear in four dimensions. In a given 3D slice we only have access to one link associated with a time-oriented vortex,

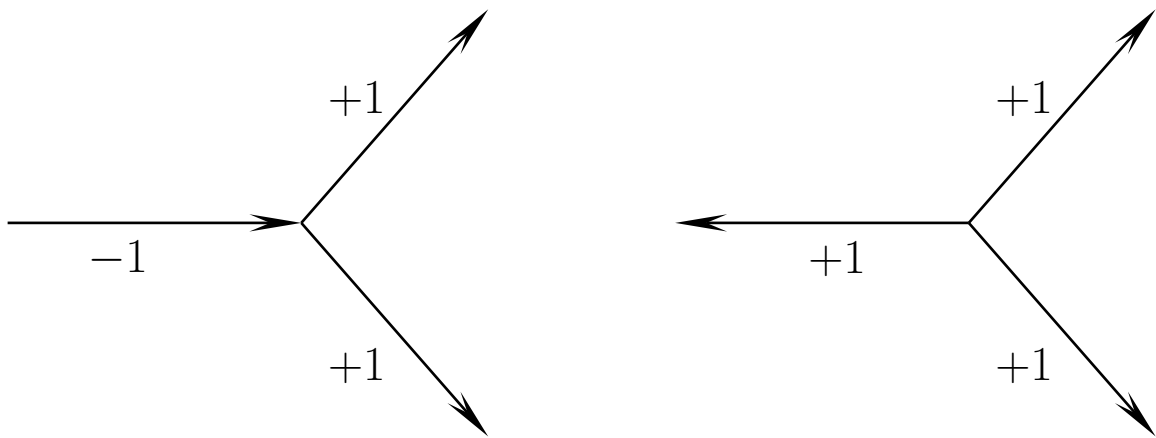


Fig. 7.5 **Left:** A vortex branching point. **Right:** A vortex monopole. Note that for both figures, the vortex charge is conserved at the vertex. By changing the orientation of the plaquette containing the left-most vortex, these two diagrams can be interchanged.

and as such we plot an arrow along this link to indicate its association with this vortex. We adopt the following plotting convention for these time-oriented vortices:

- +1 vortex, forward in time  $\Rightarrow$  cyan arrow, positively oriented.
- +1 vortex, backward in time  $\Rightarrow$  cyan arrow, negatively oriented.
- -1 vortex, forward in time  $\Rightarrow$  orange arrow, positively oriented.
- -1 vortex, backward in time  $\Rightarrow$  orange arrow, negatively oriented.

An example of these conventions is shown in Fig. 7.6. Utilising these conventions, we see that the first two time slices now appear as Figs. [7.7, 7.8]

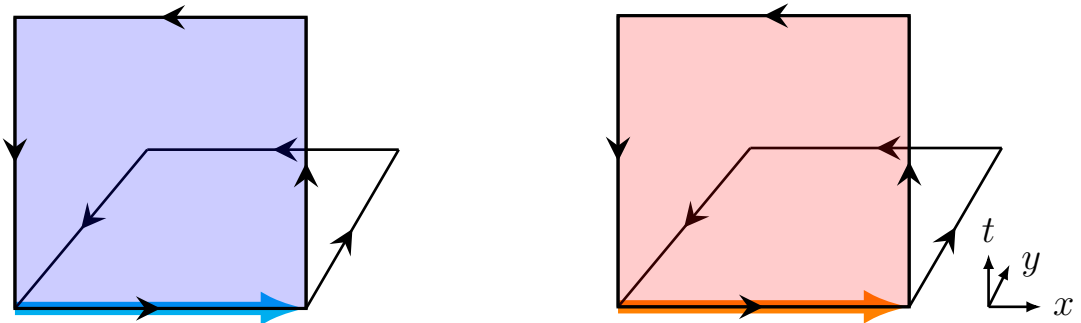


Fig. 7.6 **Left:** A +1 vortex in the forward  $x - t$  plane (shaded blue) will be plotted as a cyan arrow in the  $+\hat{x}$  direction. **Right:** A -1 vortex in the forward  $x - t$  plane (shaded red) will be plotted as an orange arrow in the  $+\hat{x}$  direction.

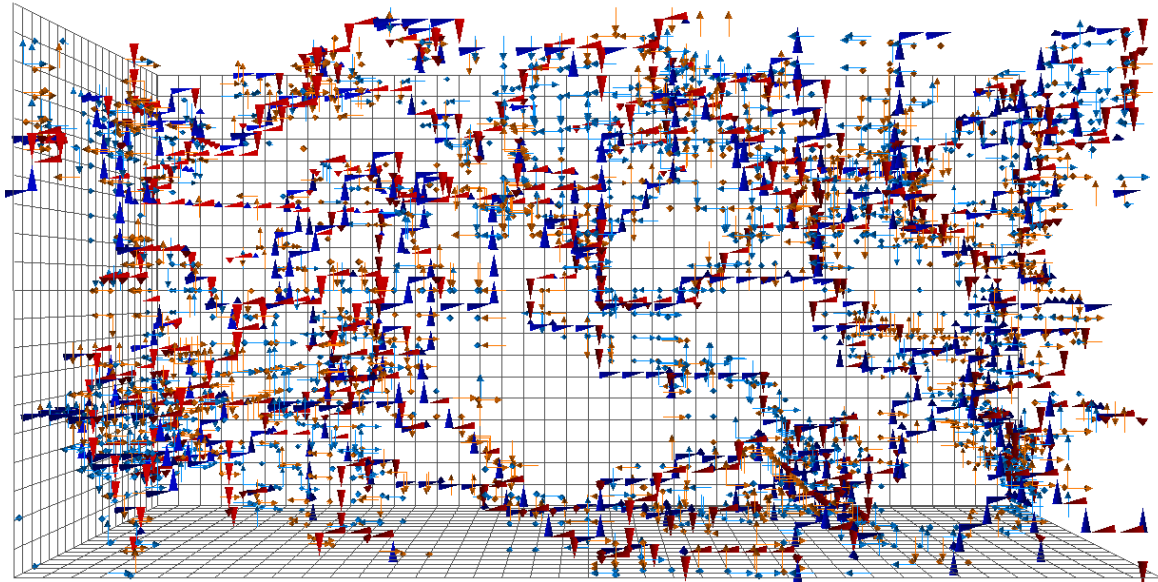


Fig. 7.7 The  $t = 1$  slice with all space-oriented and time-oriented vortices plotted.

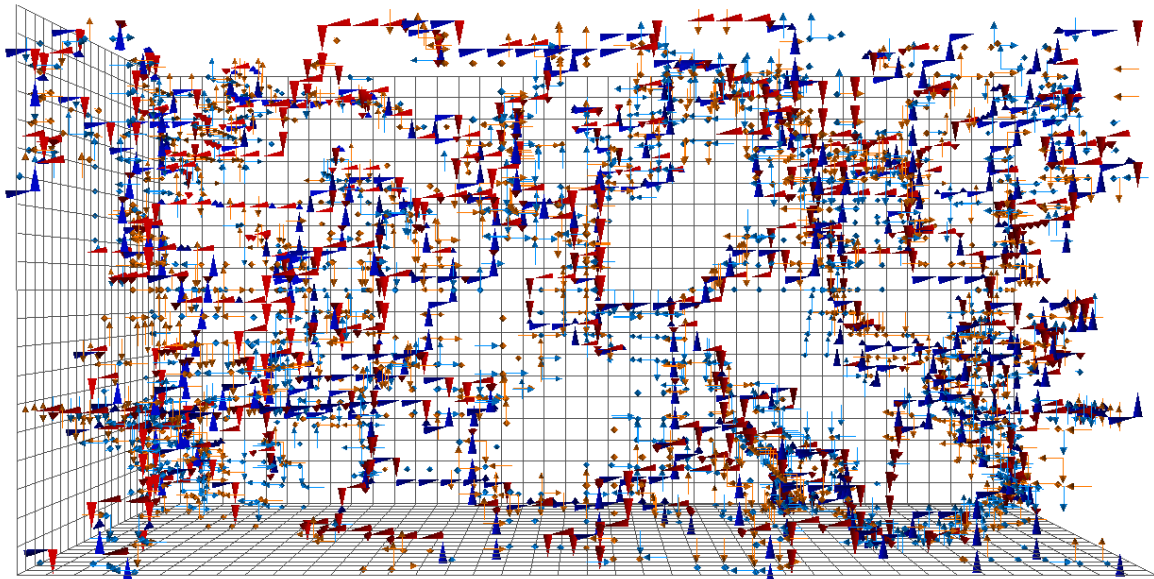


Fig. 7.8 The  $t = 2$  slice with all space-oriented and time-oriented vortices plotted.

As we step through time, we expect to see the positively oriented vortices retain their colour but swap direction as they transition from being forwards in time to backwards in time, as shown in Fig. 7.9. The time-oriented vortices act as predictors of vortex motion between slices. To see this, consider Fig. 7.10. In Fig. 7.10a, we observe a line of four  $-1$  (red) space-oriented vortices with no time-oriented links associated with them, indicating that this line should remain fixed as we step through time. Alternatively, towards the top of the red line we observe a branching point with two associated  $-1$  time-oriented arrows, indicating that this branching point should move in the direction of the time-oriented vortices. Observing the same region at  $t = 2$  in Fig. 7.10b, we see that this is precisely what occurs. The vortex line has remained fixed, whereas the branching point has shifted one lattice spacing to the left, in accordance with the direction indicated by the time-oriented vortex.

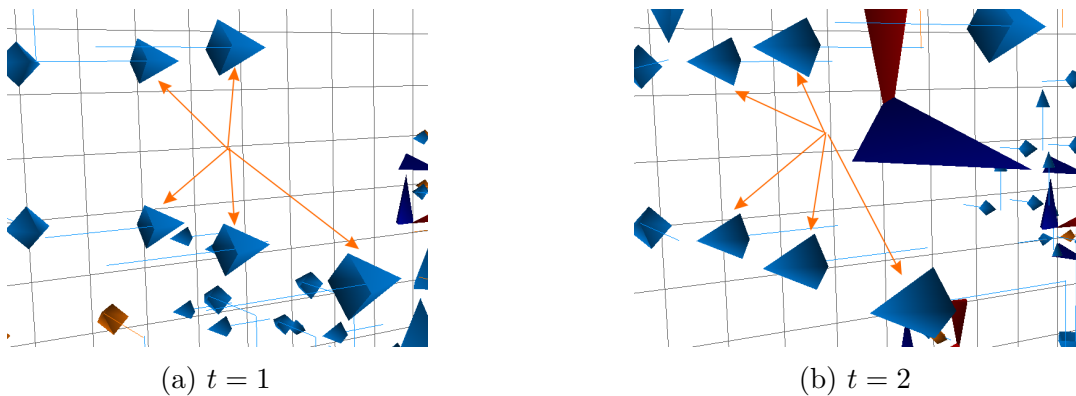


Fig. 7.9 As we step through time we observe the time-oriented arrows change direction, however the phase (colour) of the vortex remains the same.

Another example of time-oriented vortices predicting the motion of vortices is shown in Fig. 7.11. Here we see in Fig. 7.11a a line of three  $+1$  space-oriented vortices each with an associated  $-1$  time-oriented vortex below them. As we step to  $t = 2$  in Fig. 7.11b we observe the time-oriented arrows change direction as expected, and the space-oriented vortex line shifts one lattice spacing down such that the time-oriented vortices are now above them.

The cases presented in Fig. 7.10 and Fig. 7.11 are ideal, where the space-oriented vortex shifts only one lattice spacing between time slices. However, it is frequently the case where the space-oriented vortices shift multiple lattice spacings per time step. To see how this occurs diagrammatically, consider Fig. 7.12. The shaded red

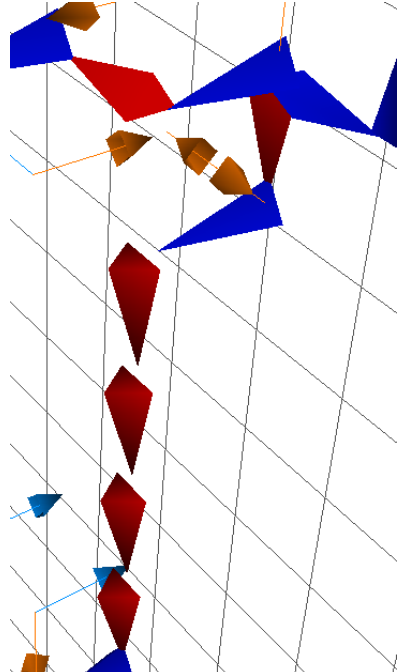
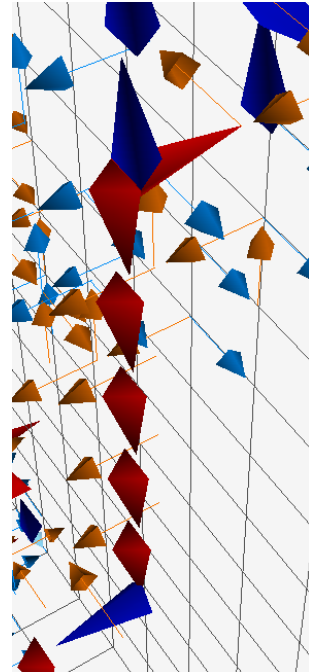
(a)  $t = 1$ (b)  $t = 2$ 

Fig. 7.10 An example of time-oriented vortices predicting the motion of the space-oriented vortices. We observe the  $-1$  (red) vortex line with no associated time-oriented vortices remain stationary as we transition from  $t = 1$  to  $t = 2$ .

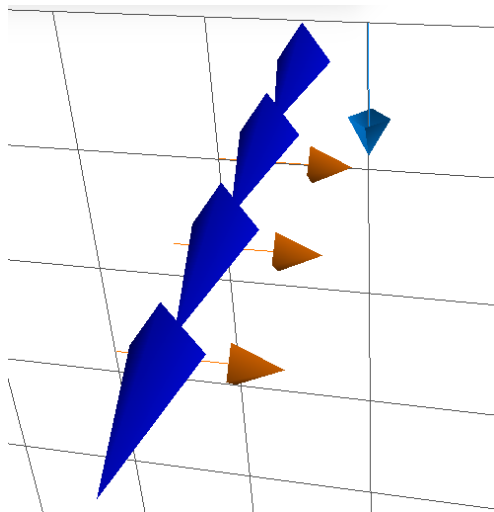
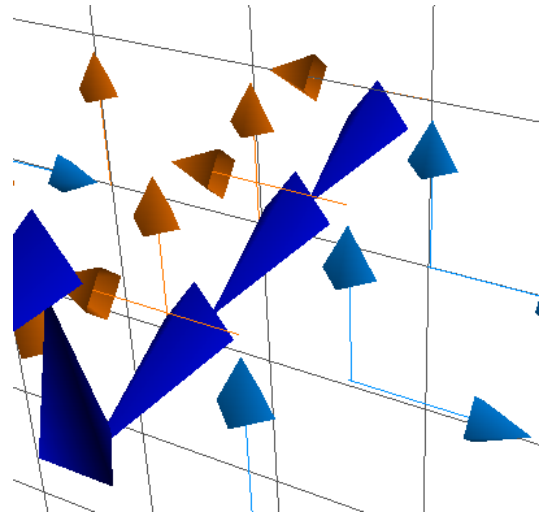
(a)  $t = 1$ (b)  $t = 2$ 

Fig. 7.11 A second example of time-oriented vortices predicting the motion of the space-oriented vortices. Here we see the  $+1$  (blue) vortex line transition one lattice spacing down as we step from  $t = 1$  to  $t = 2$ .

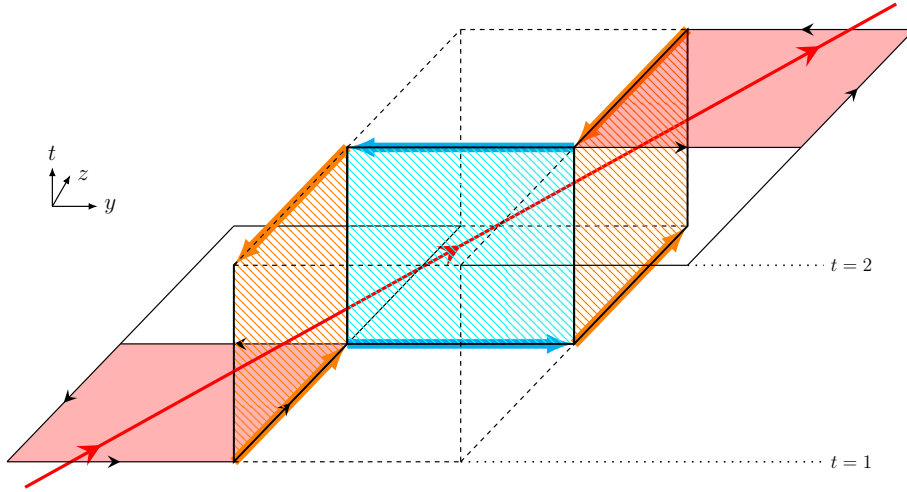


Fig. 7.12 A demonstration of how space-oriented vortices can transition multiple lattice spacings in a single time step.

plaquettes indicate the location of a space-oriented vortex which would be plotted in the suppressed  $\hat{x}$  direction. The red line demonstrates how the vortex line pierces between the two time slices. Within each slice we would observe the time-oriented links shown, however the space-oriented vortex appears to move three plaquettes in one time step. These multiple transitions make it harder to track the motion of vortices between time slices; nevertheless, the time-oriented vortices are a useful tool for understanding how centre vortices evolve with time. It is worth making clear that if a space-oriented vortex has no associated time-oriented vortices then it is guaranteed to remain stationary. In this respect, the lack of time-oriented vortices is a clear and valuable indicator of vortex behaviour.

### 7.3 Topological Charge

We now wish to observe the relationship between vortices and topological charge. As stated in Sec. 3.3.1, the topological charge density is given by

$$q(x) = \frac{1}{32\pi^2} \epsilon_{\mu\nu\rho\sigma} \text{Tr} (F_{\mu\nu}(x) F_{\rho\sigma}(x)) . \quad (7.1)$$

Given the presence of the antisymmetric tensor, it is clear that for there to be non-trivial topological charge present on the projected vortex configurations, we require that the tangent vectors of the vortex surface span all four dimensions. This condition is met at *singular points*, which can be broken into three categories [107, 111]

1. Intersection points.
2. Touching points.
3. Writhing points.

The contribution to the topological charge from these singular points is discussed in detail in Refs. [107, 108, 111, 112]. In our visualisations, these singular points appear as a space-oriented vortex running parallel to a time-oriented vortex, as shown in Fig. 7.13.

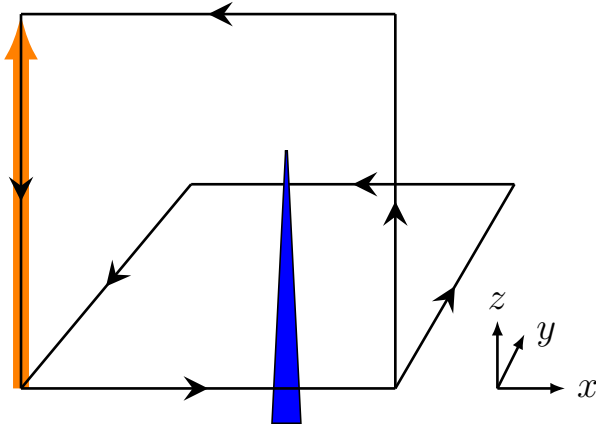


Fig. 7.13 The signature of a singular point, in which the vortex surface spans all four directions. The colour and orientation of the vortices is irrelevant, so long as they are parallel.

We calculate the topological charge via the method outlined in Sec. 3.3.1 on a lattice configuration after eight sweeps of cooling. This cooling is necessary to remove short-range fluctuations, but is a sufficiently low number of sweeps so as to minimally perturb the configuration. We plot regions of positive topological charge in blue, and regions of negative topological charge in red, with a colour gradient to indicate the magnitude. Only topological charge of sufficient magnitude is plotted to better emphasise regions of significant topological charge. Overlaying the topological charge visualisation onto Figs. 7.7, 7.8, we obtain Figs. 7.14, 7.15. By studying the regions of high topological charge, we note that we can indeed observe their relationship with singular points, as shown in Fig. 7.16.

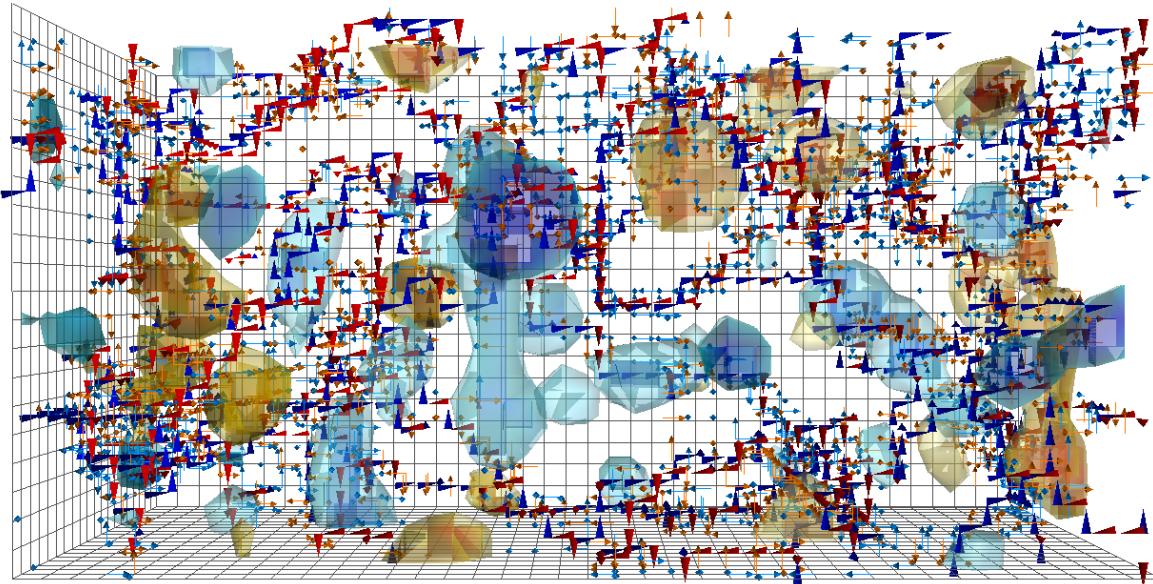


Fig. 7.14 Topological charge density overlaying the  $t = 1$  slice.

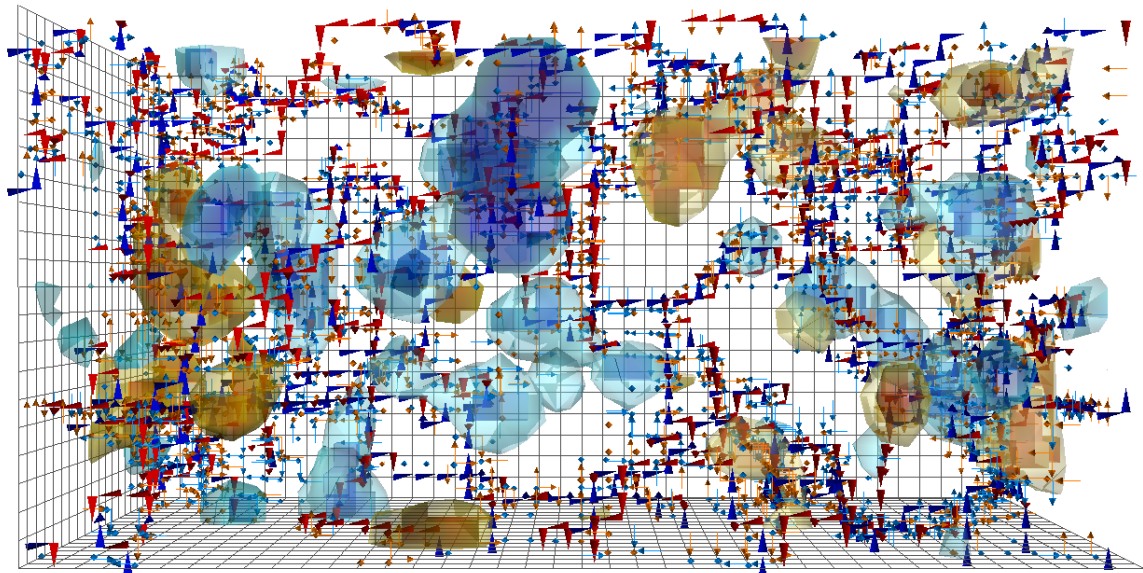


Fig. 7.15 Topological charge density overlaying the  $t = 2$  slice.

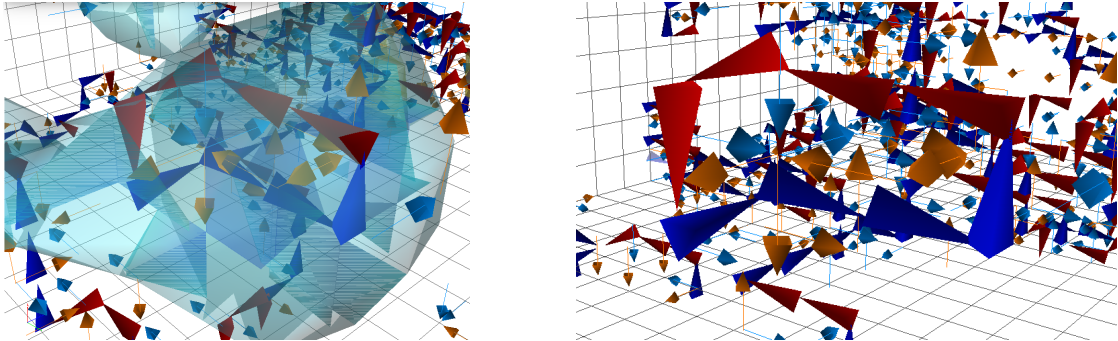


Fig. 7.16 A collection of singular points shown with (left) and without (right) topological charge overlaid.

To quantify the correlation between vortex locations and topological charge, we use the following measure

$$C = V \frac{\sum_x |q(x)| L(x)}{\sum_x |q(x)| \sum_x L(x)}, \quad (7.2)$$

where  $V$  is the lattice volume, and

$$L(x) = \begin{cases} 1, & \text{Vortex associated with any plaquette touching } x \\ 0, & \text{No vortex associated with any plaquette touching } x. \end{cases} \quad (7.3)$$

In the case of no correlation,  $C = 1$ . If there is correlation or anti-correlation, then  $C > 1$  or  $C < 1$  respectively. The value of  $C$  for our configurations is shown in Fig. 7.17, with an average over all 100 configurations of  $\bar{C} = 1.46$ . This indicates a correlation between vortex locations and regions of high topological charge. Further work to investigate the precise nature of this correlation and its relationship to singular points is planned.

Finally, it is also interesting to study the vortex structure of the lattice after cooling. After eight sweeps of cooling, we obtain Fig. 7.18. We clearly see that the complexity of the vortex structure has been greatly reduced, however the regions associated with topological charge have been less affected by the smoothing process. We can see this by recalculating the topological charge, shown in Fig. 7.19. The average correlation has increased to a new average of  $\bar{C} = 1.76$ , indicating that the residual vortices show a stronger correlation to the regions of high topological charge than those on the un-cooled configurations. This further supports the previously mentioned notion that cooling serves to isolate ‘genuine’ topological objects and filter out those arising from fluctuations during the monte-carlo lattice generation process.

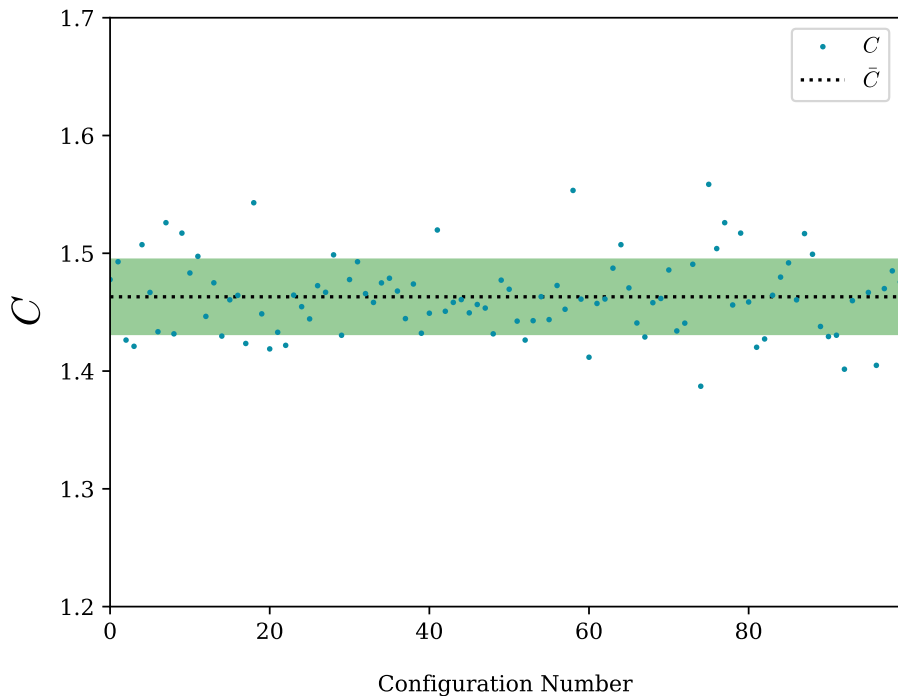


Fig. 7.17 The correlation measure for each configuration is shown. The dashed line indicates the average value across all 100 configurations, with the one standard deviation region shown in green.

## 7.4 Summary

In this chapter we have presented a new way to visualise the four-dimensional structure of centre vortices on the lattice through the use of 3D visualisation techniques. These visualisations give new insight into the geometry and time-evolution of vortices, as well as revealing a direct connection to topological charge. The work presented here is preliminary, and in future it would be valuable to improve the ability to identify branching/monopole points and singular points such that they may be studied in a more quantitative way. Developing techniques to categorise the nature of singular points to further elucidate their connection to topological charge would also be another worthwhile avenue to pursue. From this work, it is clear that visualisations of centre vortices provide valuable information about the structure of the QCD vacuum that is otherwise not apparent through purely numerical results, and that visualisations elegantly complement more traditional calculation techniques.

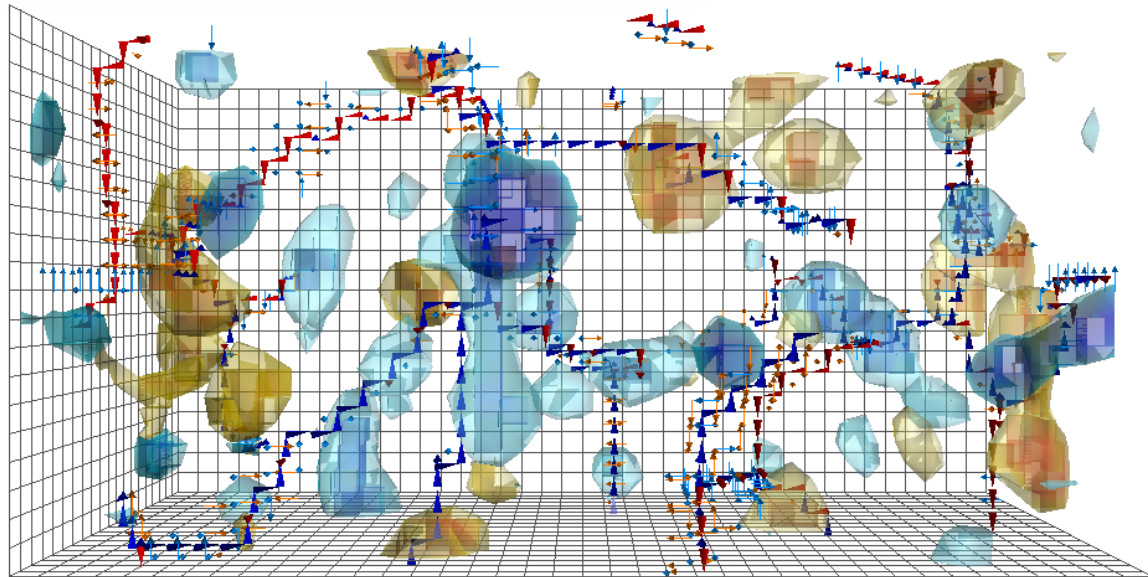


Fig. 7.18 The vortex structure and topological charge after eight sweeps of cooling, for  $t = 1$ .

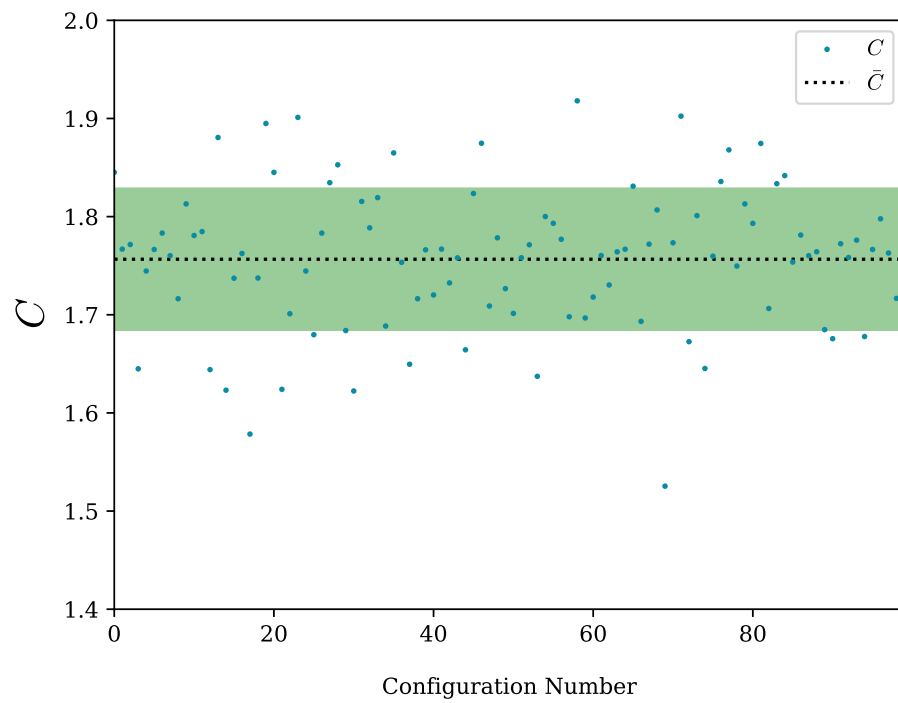


Fig. 7.19 The correlation measure for each configuration after eight sweeps of cooling is shown. The dashed line indicates the average value across all 100 configurations, with the one standard deviation region shown in green.

# Chapter 8

## Conclusion

In this work we have studied the impact of centre vortices on the Landau gauge gluon propagator by calculating the gluon propagator on original, vortex removed and vortex only lattice configurations. We observe that vortices effectively partition the propagator into long-distance and short-distance strength, with the vortex only configurations encapsulating much of the non-perturbative behaviour of the propagator. This partitioning is consistent with the vortex modified gauge potential representing orthogonal degrees of freedom. Although the vortex only propagator does not demonstrate the full infrared strength of the original propagator, it is clear that vortices are crucial to the long-range behaviour of the propagator.

We then investigated the effect of smoothing on the gluon propagator, determining that both three-loop cooling and over-improved stoutlink smearing produce similar amplification of infrared strength and suppression of high frequency modes. Indeed, we found that for each sweep of cooling, four sweeps of smearing produces a remarkably similar propagator when calculated on the original configurations. Using cooling as our smoothing method of choice, we found that cooling brings the gluon propagator on the untouched and vortex only configurations closer together. By using the average action as a measure of roughness, we see that it is possible to recover the infrared strength of the vortex-only propagator when compared to the untouched propagator. The accuracy to which it is possible to recreate the gluon propagator from vortex only configurations on similarly smooth original configurations is of particular note.

We then presented a novel method for visualising projected vortex configurations, allowing for analysis of vortex geometry in a highly interactive manner. From these visualisations we discover that, at low temperature, vortices tend to span the full

lattice extent. Furthermore, we observe an abundance of branching/monopole points present in the vortex structure. By overlaying the topological charge density, we note a distinct relationship between topological charge and singular points where the vortex sheets span all four dimensions. We also find an explicit correlation between vortex locations and regions of high topological charge. Under cooling, we find that the vortex structure of the lattice is considerably simplified, with the residual vortex matter showing a stronger correlation to regions of high topological charge. This indicates that cooling does indeed preserve genuine topological objects relevant to the long distance behaviour of QCD, whilst filtering out extraneous structures. Although many of our findings are somewhat qualitative, these visualisations open many new avenues for investigation of the vacuum structure of QCD and the significance of centre vortices.

These findings suggest many potential directions for future work. It would be valuable to investigate whether improved vortex identification allows us to account for the discrepancy between the untouched and vortex only propagators. It is also of interest to calculate the gluon propagator in full QCD, where it is anticipated that we would observe infrared screening due to the presence of fermions. The relevance of smoothing is currently poorly understood, and studying the behaviour of the gluon propagator in the continuum limit would clarify whether smoothing is essential to grow vortices to a physical size, or if it is simply necessary to remove high-frequency fluctuations present on the vortex-only configurations. Developing techniques to identify singular points within our visualisations and quantitatively assessing their relationship with topological charge would also be of great interest.

The centre vortex model has demonstrated remarkable success in recent years, and the work presented here continues to support the relevance of centre vortices to the essential properties of confinement and dynamical chiral symmetry breaking in QCD. It is increasingly apparent that centre vortices are an essential component in a complete understanding of QCD vacuum structure.

# References

- [1] K. G. Wilson, Phys. Rev. **D10**, 2445 (1974).
- [2] M. E. Peskin, *An introduction to quantum field theory* (CRC Press, 2018).
- [3] L. H. Ryder, *Quantum field theory* (Cambridge University Press, 1996).
- [4] T. Schäfer and E. V. Shuryak, Rev. Mod. Phys. **70**, 323 (1998), arXiv:hep-ph/9610451 [hep-ph] .
- [5] M. Lüscher and P. Weisz, Commun. Math. Phys. **97**, 59 (1985), [Erratum: Commun. Math. Phys. 98, 433 (1985)].
- [6] H. Bing and L. He, (1999), arXiv:hep-th/9912189 [hep-th] .
- [7] G. P. Lepage, in *Strong interactions at low and intermediate energies. Proceedings, 13th Annual Hampton University Graduate Studies, HUGS'98, Newport News, USA, May 26-June 12, 1998* (1998) pp. 49–90, arXiv:hep-lat/0506036 [hep-lat] .
- [8] D. B. Leinweber, J. I. Skullerud, A. G. Williams, and C. Parrinello (UKQCD), Phys. Rev. **D58**, 031501 (1998), arXiv:hep-lat/9803015 [hep-lat] .
- [9] B. Alles, D. Henty, H. Panagopoulos, C. Parrinello, C. Pittori, and D. G. Richards, Nucl. Phys. **B502**, 325 (1997), arXiv:hep-lat/9605033 [hep-lat] .
- [10] R. Gupta, in *Probing the standard model of particle interactions. Proceedings, Summer School in Theoretical Physics, NATO Advanced Study Institute, 68th session, Les Houches, France, July 28-September 5, 1997. Pt. 1, 2* (1997) pp. 83–219, arXiv:hep-lat/9807028 [hep-lat] .
- [11] M. G. Alford, W. Dimm, G. P. Lepage, G. Hockney, and P. B. Mackenzie, Phys. Lett. **B361**, 87 (1995), arXiv:hep-lat/9507010 [hep-lat] .
- [12] K. Symanzik, Nucl. Phys. **B226**, 187 (1983).
- [13] K. Symanzik, Nucl. Phys. **B226**, 205 (1983).

- [14] G. P. Lepage and P. B. Mackenzie, Phys. Rev. **D48**, 2250 (1993), arXiv:hep-lat/9209022 [hep-lat].
- [15] F. D. R. Bonnet, P. O. Bowman, D. B. Leinweber, A. G. Williams, and D. G. Richards, Austral. J. Phys. **52**, 939 (1999), arXiv:hep-lat/9905006 [hep-lat].
- [16] G. 't Hooft, Nucl. Phys. **B190**, 455 (1981).
- [17] J. Smit and A. van der Sijs, Nucl. Phys. **B355**, 603 (1991).
- [18] Y. Matsubara, S. Ejiri, and T. Suzuki, *LATTICE 93: 11th International Symposium on Lattice Field Theory Dallas, Texas, October 12-16, 1993*, Nucl. Phys. Proc. Suppl. **34**, 176 (1994), arXiv:hep-lat/9311061 [hep-lat].
- [19] T. Suzuki and I. Yotsuyanagi, Phys. Rev. **D42**, 4257 (1990).
- [20] S. Mandelstam, #DONE: *Phys. Rep.* **23** (1976) 245-249, In \*Gervais, J.L. (Ed.), Jacob, M. (Ed.): *Non-linear and Collective Phenomena In Quantum Physics\**, 12-16, *Phys. Rept.* **23**, 245 (1976).
- [21] A. S. Kronfeld, M. L. Laursen, G. Schierholz, and U. J. Wiese, Phys. Lett. **B198**, 516 (1987).
- [22] T. L. Ivanenko, A. V. Pochinsky, and M. I. Polikarpov, Phys. Lett. **B252**, 631 (1990).
- [23] M. N. Chernodub and F. V. Gubarev, JETP Lett. **62**, 100 (1995), arXiv:hep-th/9506026 [hep-th].
- [24] A. A. Belavin, A. M. Polyakov, A. S. Schwartz, and Yu. S. Tyupkin, Phys. Lett. **B59**, 85 (1975), [,350(1975)].
- [25] E. Witten, Nucl. Phys. **B149**, 285 (1979).
- [26] C. G. Callan, Jr., R. F. Dashen, and D. J. Gross, Phys. Rev. **D17**, 2717 (1978), [,36(1977)].
- [27] D. Trewartha, W. Kamleh, D. Leinweber, and D. S. Roberts, Phys. Rev. **D88**, 034501 (2013), arXiv:1306.3283 [hep-lat].
- [28] Y. Aharonov, A. Casher, and S. Yankielowicz, Nucl. Phys. **B146**, 256 (1978).
- [29] G. 't Hooft, Nucl.Phys. **B138**, 1 (1978).
- [30] G. 't Hooft, Nucl.Phys. **B153**, 141 (1979).

- [31] R. P. Feynman, Nucl. Phys. **B188**, 479 (1981).
- [32] J. M. Cornwall, Nucl. Phys. **B157**, 392 (1979).
- [33] H. B. Nielsen and P. Olesen, Nucl. Phys. **B160**, 380 (1979).
- [34] G. Mack and V. B. Petkova, Annals Phys. **123**, 442 (1979).
- [35] J. C. Biddle, W. Kamleh, and D. B. Leinweber, Phys. Rev. **D98**, 094504 (2018), arXiv:1806.04305 [hep-lat].
- [36] M. Faber, J. Greensite, and S. Olejnik, Phys. Rev. **D57**, 2603 (1998), arXiv:hep-lat/9710039 [hep-lat].
- [37] K. Langfeld, O. Tennert, M. Engelhardt, and H. Reinhardt, Phys. Lett. **B452**, 301 (1999), arXiv:hep-lat/9805002 [hep-lat].
- [38] P. O. Bowman, K. Langfeld, D. B. Leinweber, A. O' Cais, A. Sternbeck, L. von Smekal, and A. G. Williams, Phys. Rev. **D78**, 054509 (2008), arXiv:0806.4219 [hep-lat].
- [39] D. Trewartha, W. Kamleh, and D. Leinweber, Phys. Rev. **D92**, 074507 (2015), arXiv:1509.05518 [hep-lat].
- [40] D. Trewartha, W. Kamleh, and D. Leinweber, Phys. Lett. **B747**, 373 (2015), arXiv:1502.06753 [hep-lat].
- [41] D. Trewartha, W. Kamleh, and D. Leinweber, J. Phys. **G44**, 125002 (2017), arXiv:1708.06789 [hep-lat].
- [42] L. Del Debbio, M. Faber, J. Greensite, and S. Olejnik, Phys. Rev. **D55**, 2298 (1997), arXiv:hep-lat/9610005 [hep-lat].
- [43] J. Greensite, Prog. Part. Nucl. Phys. **51**, 1 (2003), arXiv:hep-lat/0301023 [hep-lat].  
.
- [44] L. Del Debbio, M. Faber, J. Giedt, J. Greensite, and S. Olejnik, Phys. Rev. **D58**, 094501 (1998), arXiv:hep-lat/9801027 [hep-lat].
- [45] E.-A. O'Malley, W. Kamleh, D. Leinweber, and P. Moran, Phys. Rev. **D86**, 054503 (2012), arXiv:1112.2490 [hep-lat].
- [46] K. Langfeld, Phys. Rev. **D69**, 014503 (2004), arXiv:hep-lat/0307030 [hep-lat].
- [47] P. O. Bowman, K. Langfeld, D. B. Leinweber, A. Sternbeck, L. von Smekal, and A. G. Williams, Phys. Rev. **D84**, 034501 (2011), arXiv:1010.4624 [hep-lat].

- [48] M. Gell-Mann, Phys. Lett. **8**, 214 (1964).
- [49] G. Zweig, in *DEVELOPMENTS IN THE QUARK THEORY OF HADRONS. VOL. 1. 1964 - 1978*, edited by D. Lichtenberg and S. P. Rosen (1964) pp. 22–101.
- [50] R. Hofstadter, Rev. Mod. Phys. **28**, 214 (1956).
- [51] E. D. Bloom *et al.*, Phys. Rev. Lett. **23**, 930 (1969).
- [52] M. Breidenbach, J. I. Friedman, H. W. Kendall, E. D. Bloom, D. H. Coward, H. C. DeStaeler, J. Drees, L. W. Mo, and R. E. Taylor, Phys. Rev. Lett. **23**, 935 (1969).
- [53] R. P. Feynman, Phys. Rev. Lett. **23**, 1415 (1969), [,494(1969)].
- [54] D. J. Gross and F. Wilczek, Phys. Rev. Lett. **30**, 1343 (1973), [,271(1973)].
- [55] K. D. Born, E. Laermann, R. Sommer, P. M. Zerwas, and T. F. Walsh, Phys. Lett. **B329**, 325 (1994).
- [56] F. D. R. Bonnet, D. B. Leinweber, A. G. Williams, and J. M. Zanotti, Submitted to: Phys. Rev. D (1999), arXiv:hep-lat/9912044 [hep-lat].
- [57] M. Creutz, Phys. Rev. **D23**, 1815 (1981).
- [58] A. Di Giacomo, M. Maggiore, and S. Olejnik, Nucl. Phys. **B347**, 441 (1990).
- [59] D. Zwanziger, Nucl. Phys. **D364**, 127 (1991).
- [60] Y. Iwasaki, K. Kanaya, S. Sakai, and T. Yoshie, Phys. Rev. Lett. **69**, 21 (1992).
- [61] G. 't Hooft, Phys. Rept. **142**, 357 (1986).
- [62] J. Greensite, *Proceedings, 12th Conference on Quark Confinement and the Hadron Spectrum (Confinement XII): Thessaloniki, Greece*, EPJ Web Conf. **137**, 01009 (2017), arXiv:1610.06221 [hep-lat].
- [63] Y. Makeenko, *12th International Moscow School of Physics and 37th ITEP Winter School of Physics Moscow, Russia, February 9-16, 2009*, Phys. Atom. Nucl. **73**, 878 (2010), arXiv:0906.4487 [hep-th].
- [64] H. G. Dosch and Yu. A. Simonov, Phys. Lett. **B205**, 339 (1988).
- [65] J. Greensite and M. B. Halpern, Phys. Rev. **D27**, 2545 (1983).
- [66] M. Engelhardt, K. Langfeld, H. Reinhardt, and O. Tennert, Phys. Rev. **D61**, 054504 (2000), arXiv:hep-lat/9904004 [hep-lat].

- [67] M. Faber, J. Greensite, S. Olejnik, and D. Yamada, JHEP **12**, 012 (1999), arXiv:hep-lat/9910033 [hep-lat].
- [68] A. Montero, Phys. Lett. **B467**, 106 (1999), arXiv:hep-lat/9906010 [hep-lat].
- [69] M. Faber, J. Greensite, and S. Olejnik, Phys. Lett. **B474**, 177 (2000), arXiv:hep-lat/9911006 [hep-lat].
- [70] I. L. Bogolubsky, E. M. Ilgenfritz, M. Muller-Preussker, and A. Sternbeck, Phys. Lett. **B676**, 69 (2009), arXiv:0901.0736 [hep-lat].
- [71] A. O'Cais, W. Kamleh, K. Langfeld, B. Lasscock, D. Leinweber, P. Moran, A. Sternbeck, and L. von Smekal, Phys. Rev. **D82**, 114512 (2010), arXiv:0807.0264 [hep-lat].
- [72] J. Ambjorn, P. Olesen, and C. Peterson, Nucl. Phys. **B240**, 189 (1984).
- [73] J. Ambjorn, P. Olesen, and C. Peterson, Nucl. Phys. **B240**, 533 (1984).
- [74] N. A. Campbell, I. H. Jorysz, and C. Michael, Phys. Lett. **167B**, 91 (1986).
- [75] K. Langfeld, H. Reinhardt, and J. Gattnar, Nucl. Phys. **B621**, 131 (2002), arXiv:hep-ph/0107141 [hep-ph].
- [76] M. Quandt, H. Reinhardt, and G. Burgio, Phys. Rev. **D81**, 065016 (2010), arXiv:1001.3699 [hep-lat].
- [77] F. Spengler, M. Quandt, and H. Reinhardt, Phys. Rev. **D98**, 094508 (2018), arXiv:1810.04072 [hep-th].
- [78] H. Reinhardt, Nucl. Phys. **B628**, 133 (2002), arXiv:hep-th/0112215 [hep-th].
- [79] P. J. Moran and D. B. Leinweber, Phys. Rev. **D77**, 094501 (2008), arXiv:0801.1165 [hep-lat].
- [80] C. Alexandrou, A. Athenodorou, K. Cichy, A. Dromard, E. Garcia-Ramos, K. Jansen, U. Wenger, and F. Zimmermann, (2017), arXiv:1708.00696 [hep-lat].  
.
- [81] S. O. Bilson-Thompson, F. D. R. Bonnet, D. B. Leinweber, and A. G. Williams, *Lattice Hadron Physics. Proceedings: Workshop, LHP 2001, Cairns, Australia, Jul 9-18, 2001*, Nucl. Phys. Proc. Suppl. **109A**, 116 (2002), [,116(2001)], arXiv:hep-lat/0112034 [hep-lat].
- [82] P. J. Moran and D. B. Leinweber, Phys. Rev. **D78**, 054506 (2008), arXiv:0801.2016 [hep-lat].

- 
- [83] A. Cucchieri, Phys. Rev. **D60**, 034508 (1999), arXiv:hep-lat/9902023 [hep-lat] .
  - [84] F. D. R. Bonnet, P. O. Bowman, D. B. Leinweber, A. G. Williams, and J. M. Zanotti, Phys. Rev. **D64**, 034501 (2001), arXiv:hep-lat/0101013 [hep-lat] .
  - [85] P. Weisz, Nucl. Phys. **B212**, 1 (1983).
  - [86] P. Weisz and R. Wohlert, Nucl. Phys. **B236**, 397 (1984), [Erratum: Nucl. Phys.B247,544(1984)].
  - [87] M. Luscher and P. Weisz, Phys. Lett. **158B**, 250 (1985).
  - [88] P. Marenzoni, G. Martinelli, and N. Stella, Nucl. Phys. **B455**, 339 (1995), arXiv:hep-lat/9410011 [hep-lat] .
  - [89] F. D. R. Bonnet, P. Fitzhenry, D. B. Leinweber, M. R. Stanford, and A. G. Williams, Phys. Rev. **D62**, 094509 (2000), arXiv:hep-lat/0001018 [hep-lat] .
  - [90] B. Berg, Phys. Lett. **104B**, 475 (1981).
  - [91] N. Cabibbo and E. Marinari, Phys. Lett. **119B**, 387 (1982).
  - [92] M. Creutz, Phys. Rev. **D21**, 2308 (1980).
  - [93] S. O. Bilson-Thompson, D. B. Leinweber, and A. G. Williams, Annals Phys. **304**, 1 (2003), arXiv:hep-lat/0203008 [hep-lat] .
  - [94] M. Albanese *et al.* (APE), Phys. Lett. **B192**, 163 (1987).
  - [95] M. Falcioni, M. L. Paciello, G. Parisi, and B. Taglienti, Nucl. Phys. **B251**, 624 (1985).
  - [96] C. Morningstar and M. J. Peardon, Phys. Rev. **D69**, 054501 (2004), arXiv:hep-lat/0311018 [hep-lat] .
  - [97] M. Garcia Perez, A. Gonzalez-Arroyo, J. R. Snippe, and P. van Baal, Nucl. Phys. **B413**, 535 (1994), arXiv:hep-lat/9309009 [hep-lat] .
  - [98] S. D. Thomas, W. Kamleh, and D. B. Leinweber, Phys. Rev. **D92**, 094515 (2015), arXiv:1410.7105 [hep-lat] .
  - [99] J. D. Stack, W. W. Tucker, and R. J. Wensley, Nucl. Phys. **B639**, 203 (2002), arXiv:hep-lat/0110196 [hep-lat] .
  - [100] T. van Ritbergen, J. A. M. Vermaseren, and S. A. Larin, Phys. Lett. **B400**, 379 (1997), arXiv:hep-ph/9701390 [hep-ph] .

- [101] P. O. Bowman, U. M. Heller, D. B. Leinweber, M. B. Parappilly, and A. G. Williams, Phys. Rev. **D70**, 034509 (2004), arXiv:hep-lat/0402032 [hep-lat].
- [102] D. B. Leinweber, J. I. Skullerud, A. G. Williams, and C. Parrinello (UKQCD), Phys. Rev. **D60**, 094507 (1999), [Erratum: Phys. Rev.D61,079901(2000)], arXiv:hep-lat/9811027 [hep-lat].
- [103] P. Boucaud, T. Bruntjen, J. P. Leroy, A. Le Yaouanc, A. Y. Lohkov, J. Michel, O. Pene, J. Rodriguez-Quintero, and C. Roiesnel, (2006), arXiv:hep-lat/0602006 [hep-lat].
- [104] R. Bertle, M. Engelhardt, and M. Faber, Phys. Rev. **D64**, 074504 (2001), arXiv:hep-lat/0104004 [hep-lat].
- [105] M. Engelhardt, M. Quandt, and H. Reinhardt, Nucl. Phys. **B685**, 227 (2004), arXiv:hep-lat/0311029 [hep-lat].
- [106] R. Bertle, M. Faber, J. Greensite, and S. Olejnik, JHEP **03**, 019 (1999), arXiv:hep-lat/9903023 [hep-lat].
- [107] M. Engelhardt, Phys. Rev. **D83**, 025015 (2011), arXiv:1008.4953 [hep-lat].
- [108] M. Engelhardt and H. Reinhardt, Nucl. Phys. **B567**, 249 (2000), arXiv:hep-th/9907139 [hep-th].
- [109] J. M. Cornwall, Phys. Rev. **D61**, 085012 (2000), arXiv:hep-th/9911125 [hep-th].
- [110] J. M. Cornwall, Phys. Rev. **D58**, 105028 (1998), arXiv:hep-th/9806007 [hep-th].
- [111] M. Engelhardt, Nucl. Phys. **B585**, 614 (2000), arXiv:hep-lat/0004013 [hep-lat].
- [112] F. Bruckmann and M. Engelhardt, Phys. Rev. **D68**, 105011 (2003), arXiv:hep-th/0307219 [hep-th].



# Appendix A

## Gell-Mann matrices

The Gell-Mann matrices  $\lambda_a$  are related to the generators of  $SU(3)$ ,  $t_a$ , by

$$t_a = \frac{\lambda_a}{2}. \quad (\text{A.1})$$

The matrices are given by

$$\begin{aligned} \lambda_1 &= \begin{pmatrix} 0 & 1 & 0 \\ 1 & 0 & 0 \\ 0 & 0 & 0 \end{pmatrix} & \lambda_2 &= \begin{pmatrix} 0 & -i & 0 \\ i & 0 & 0 \\ 0 & 0 & 0 \end{pmatrix} & \lambda_3 &= \begin{pmatrix} 1 & 0 & 0 \\ 0 & -1 & 0 \\ 0 & 0 & 0 \end{pmatrix} \\ \lambda_4 &= \begin{pmatrix} 0 & 0 & 1 \\ 0 & 0 & 0 \\ 1 & 0 & 0 \end{pmatrix} & \lambda_5 &= \begin{pmatrix} 0 & 0 & -i \\ 0 & 0 & 0 \\ i & 0 & 0 \end{pmatrix} \\ \lambda_6 &= \begin{pmatrix} 0 & 0 & 0 \\ 0 & 0 & 1 \\ 0 & 1 & 0 \end{pmatrix} & \lambda_7 &= \begin{pmatrix} 0 & 0 & 0 \\ 0 & 0 & -i \\ 0 & i & 0 \end{pmatrix} & \lambda_8 &= \frac{1}{\sqrt{3}} \begin{pmatrix} 1 & 0 & 0 \\ 0 & 1 & 0 \\ 0 & 0 & -2 \end{pmatrix}. \end{aligned}$$



## Appendix B

### Taylor expansion of $P_{\mu\nu}$

First, we recall the definitions of the gauge link in the continuum

$$U_\mu(x) = \mathcal{P} \exp \left( ig \int_x^{x+a\hat{\mu}} dx' A_\mu(x') \right), \quad (\text{B.1})$$

and the plaquette formed from the product of the gauge links around a  $1 \times 1$  loop

$$P_{\mu\nu} = U_\mu(x) U_\nu(x + a\hat{\mu}) U_\mu^\dagger(x + a\hat{\nu}) U_\nu^\dagger(x). \quad (\text{B.2})$$

We can approximate the integral in Eq. B.1 by Taylor expanding  $A_\mu(x')$  around  $x' = x$  and explicitly evaluating the integral. Note that once we have Taylor expanded  $A_\mu(x')$ , the term within the integral becomes Abelian for all values of  $x'$ , allowing us to omit the path ordering from Eq. B.1. Performing the expansion, we find that

$$\begin{aligned} U_\mu(x) &= \exp \left( ig \int_x^{x+a\hat{\mu}} dx' A_\mu(x) + \sum_\sigma (\partial'_\sigma A_\mu(x')) \Big|_{x'=x} (x'^\sigma - x^\sigma) + \mathcal{O}(a^3) \right) \\ &= \exp \left( iagA_\mu(x) + \frac{1}{2}ia^2g \partial_\mu A_\mu(x) \right). \end{aligned} \quad (\text{B.3})$$

Note that whilst the  $\sigma$  index is summed over only the  $x^\mu$  term survives the integration, as for all  $x^\sigma$ ,  $\sigma \neq \mu$ ,  $(x'^\sigma - x^\sigma) = 0$ . Similarly, we evaluate

$$\begin{aligned} U_\nu(x + a\hat{\mu}) &= \exp \left( ig \int_{x+a\hat{\mu}}^{x+a\hat{\mu}+a\hat{\nu}} dx' A_\nu(x) + \sum_\sigma (\partial'_\sigma A_\nu(x')) \Big|_{x'=x} (x'^\sigma - x^\sigma) + \mathcal{O}(a^3) \right) \\ &= \exp \left( iagA_\nu(x) + iag \partial_\mu A_\nu(x) + ig \int_{x_\nu}^{x_\nu+a} dx'_\nu \partial_\nu A_\nu(x) (x'^\nu - x^\nu) \right) \\ &= \exp \left( iagA_\nu(x) + ia^2g \partial_\mu A_\nu(x) + \frac{1}{2}ia^2g \partial_\nu A_\nu(x) \right). \end{aligned} \quad (\text{B.4})$$

The  $\partial_\mu A_\nu(x)$  term is retained because for  $\sigma = \mu$  we have  $(x'^\mu - x^\mu) = (x^\mu + a\hat{\mu} - x^\mu) = a\hat{\mu}$ .

We will also require the Baker-Campbell-Hausdorff identity for non-Abelian matrix exponentials

$$\exp(A) \exp(B) = \exp\left(A + B + \frac{1}{2}[A, B]\right). \quad (\text{B.5})$$

Substituting Eq. B.3 and Eq. B.4 into Eq. B.2 and retaining only terms up to  $\mathcal{O}(a^2)$  we have

$$\begin{aligned} P_{\mu\nu} &= \exp\left(ig\left(a A_\mu(x) + \frac{1}{2}a^2 \partial_\mu A_\mu(x)\right)\right) \\ &\quad \times \exp\left(ig\left(a A_\nu(x) + \frac{1}{2}a^2 \partial_\nu A_\nu(x) + a^2 \partial_\mu A_\nu(x)\right)\right) \\ &\quad \times \exp\left(-ig\left(a A_\mu(x) + \frac{1}{2}a^2 \partial_\mu A_\mu(x) + a^2 \partial_\nu A_\mu(x)\right)\right) \\ &\quad \times \exp\left(-ig\left(a A_\nu(x) + \frac{1}{2}a^2 \partial_\nu A_\nu(x) + \dots\right)\right) \\ &= \exp\left(ia^2 g \partial_\mu A_\nu(x) - ia^2 g \partial_\nu A_\mu(x) - \frac{a^2 g^2}{2} [A_\mu(x), A_\nu(x)] + \frac{a^2 g^2}{2} [A_\nu(x), A_\mu(x)]\right) \\ &= \exp\left(ia^2 g F_{\mu\nu}(x)\right) \\ &\approx I + ia^2 g F_{\mu\nu} - \frac{a^4 g^2}{2} F_{\mu\nu}^2. \end{aligned}$$

# Appendix C

## Wilson line gauge transformation

We wish to show that the Wilson line obeys the gauge transformation property

$$U(z, y) \rightarrow \Omega(z) U(z, y) \Omega^\dagger(y). \quad (\text{C.1})$$

to show this, first recall the parallel transport equation

$$\frac{dx^\mu}{dt} (\partial_\mu - ig A_\mu(x)) U(x, y) = 0 \quad (\text{C.2})$$

If we apply a gauge transformation to  $A_\mu(x)$  and our proposed transformation to  $U(x, y)$ , Eq. C.2 becomes

$$\begin{aligned} & \frac{dx^\mu}{dt} \left( \partial_\mu - ig \left[ \Omega(x) A_\mu(x) \Omega^\dagger(x) - \frac{i}{g} (\partial_\mu \Omega(x)) \Omega(x)^\dagger \right] \right) \Omega(x) U(x, y) \Omega(y)^\dagger \\ &= \frac{dx^\mu}{dt} \left( (\partial_\mu \Omega(x)) U(x, y) \Omega(y)^\dagger + \Omega(x) (\partial_\mu U(x, y)) \Omega(y)^\dagger + \Omega(x) U(x, y) (\partial_\mu \Omega(y))^\dagger \right. \\ &\quad \left. - ig \left[ \Omega(x) A_\mu(x) - \frac{i}{g} (\partial_\mu \Omega(x)) \right] U(x, y) \Omega(y)^\dagger \right) \\ &= \frac{dx^\mu}{dt} \Omega(x) (\partial_\mu U(x, y) - ig A_\mu(x) U(x, y)) \Omega(y)^\dagger \\ &= 0. \end{aligned}$$

We therefore see that  $\Omega(x) U(x, y) \Omega^\dagger(y)$  is a solution to the parallel transport equation under a gauge transformation, and furthermore it satisfies the boundary condition  $\Omega(y) U(y, y) \Omega^\dagger(y) = I$ . Therefore, by the existence and uniqueness theorem, we find that Eq. C.1 is the gauge transformation for the Wilson Line.



## Appendix D

# Properties of the adjoint representation

Consider the mapping  $D : SU(3)^F \rightarrow SU(3)^A$  defined by

$$[D(U)]_{ij} = \frac{1}{2} \text{Tr} (\lambda_i U \lambda_j U^\dagger) . \quad (\text{D.1})$$

We want to show that for  $U, V \in SU(3)^F$

$$[D(U)]_{ij} [D(V)]^{jk} = [D(UV)]_i^k . \quad (\text{D.2})$$

To do this, we will need to make use of the following Fierz completeness relations for the  $SU(3)$  generators

$$\lambda_b^b \cdot \lambda_c^d = 2 \delta_c^a \delta_b^d - \frac{2}{3} \delta_b^a \delta_c^d . \quad (\text{D.3})$$

Substituting Eq. D.1 into Eq. D.2 and noting that repeated indicies are summed over, we have

$$\begin{aligned} [D(U)]_{\alpha\beta} [D(V)]^{\beta\gamma} &= \frac{1}{2} \lambda_{ab}^\alpha U_{bc} \lambda_{cd}^\beta U_{da}^\dagger \times \frac{1}{2} \lambda_{ef}^\beta V_{fg} \lambda_{gh}^\gamma V_{he}^\dagger \\ &= \frac{1}{2} U_{bc} U_{da}^\dagger V_{fg} V_{he}^\dagger \lambda_{ab}^\alpha \lambda_{gh}^\gamma \left( \delta_{cf} \delta_{de} - \frac{1}{3} \delta_{cd} \delta_{ef} \right) \\ &= \frac{1}{2} U_{bc} V_{cg} \lambda_{gh}^\gamma V_{hd}^\dagger U_{da}^\dagger \lambda_{ab}^\alpha - \frac{1}{6} U_{bc} U_{ca}^\dagger V_{he}^\dagger V_{eg} \lambda_{ab}^\alpha \lambda_{gh}^\gamma \\ &= \frac{1}{2} U_{bc} V_{cg} \lambda_{gh}^\gamma V_{hd}^\dagger U_{da}^\dagger \lambda_{ab}^\alpha - \frac{1}{6} \delta_{ba} \delta_{hg} \lambda_{ab}^\alpha \lambda_{gh}^\gamma \\ &= \frac{1}{2} \text{Tr} (UV \lambda^\gamma (UV)^\dagger \lambda^\alpha) - \frac{1}{6} \text{Tr} (\lambda^\alpha) \text{Tr} (\lambda^\gamma) . \end{aligned}$$

Making use of the cyclic property of the trace and the fact that the Gell-Mann matrices are traceless, we find the desired result,

$$\begin{aligned} [D(U)]_{\alpha\beta} [D(V)]^{\beta\gamma} &= \frac{1}{2} \text{Tr} (\lambda^\alpha U V \lambda^\gamma (U V)^\dagger) \\ &= [D(UV)]_{\alpha\gamma}. \end{aligned}$$

We also wish to show that for  $U^A \in SU(3)^A$  and  $U \in SU(3)^F$  that

$$\text{Tr}(U^A) = |\text{Tr}(U)|^2 - 1. \quad (\text{D.4})$$

Making use of Eq. D.1, we have

$$\begin{aligned} \text{Tr}(U^A) &= \sum_{\alpha=1}^8 \frac{1}{2} \text{Tr} (\lambda^\alpha U_\mu(x) \lambda^\alpha U_\mu^\dagger(x)) \\ &= \frac{1}{2} U_{bc} U_{da}^\dagger \lambda_{ab}^\alpha \lambda_{cd}^\alpha \\ &= U_{bc} U_{da}^\dagger \left( \delta_{ad} \delta_{bc} - \frac{1}{3} \delta_{ab} \delta_{cd} \right) \\ &= \text{Tr}(U) \text{Tr}(U^\dagger) - \frac{1}{3} \text{Tr}(U U^\dagger) \\ &= |\text{Tr}(U)|^2 - 1 \end{aligned}$$

## Appendix E

### Evaluation of $\text{Re} \text{Tr}(F_1(U)^\dagger U)$

It is apparent that we can write Eq. 5.7 in the form

$$\text{Re} \text{Tr}(F_1(U)^\dagger U), \quad (\text{E.1})$$

where  $U = U_\mu \bar{U}$ . Expanding this, we have

$$\begin{aligned} \text{Re} \text{Tr}(F_1(U)^\dagger U) &= \text{Re} \left( \frac{1}{k_1} \left[ \frac{1}{2} U_{11} (U_{22} + U_{11}^*) - \frac{1}{2} U_{21} (U_{12} - U_{21}^*) \right. \right. \\ &\quad \left. \left. + \frac{1}{2} U_{22} (U_{11} + U_{22}^*) - \frac{1}{2} U_{12} (U_{21} - U_{12}^*) + k_1 U_{33} \right] \right) \\ &= \frac{1}{k_1} \text{Re} \left( \frac{|U_{11}|^2}{2} + \frac{|U_{22}|^2}{2} + \frac{|U_{12}|^2}{2} + \frac{|U_{21}|^2}{2} + U_{11} U_{22} - U_{12} U_{21} + k_1 U_{33} \right). \end{aligned}$$

Where we have used the fact that by the construction of  $F_1(U)$ ,  $k_1$  is real. We now wish to make use of the known determinant of  $F_1(U)$  to simplify this expression.

$$\begin{aligned} \det(F_1(U)) &= \frac{1}{4 k_1^2} ((U_{11} + U_{22}^*) (U_{11}^* + U_{22}) - (U_{12} - U_{21}^*) (U_{21} - U_{12}^*)) \\ &= \frac{1}{4 k_1^2} \left( |U_{11}|^2 + |U_{22}|^2 + |U_{12}|^2 + |U_{21}|^2 \right. \\ &\quad \left. + U_{11} U_{22} + U_{11}^* U_{22}^* + U_{12} U_{21} + U_{12}^* U_{21}^* \right) \\ &= \frac{1}{2 k_1^2} \text{Re} \left( \frac{|U_{11}|^2}{2} + \frac{|U_{22}|^2}{2} + \frac{|U_{12}|^2}{2} + \frac{|U_{21}|^2}{2} + U_{11} U_{22} - U_{12} U_{21} \right) \\ &= 1. \end{aligned}$$

This gives the desired result,

$$\begin{aligned}\text{Re} \operatorname{Tr}(F_1(U)^\dagger U) &= \text{Re} \left( \frac{1}{k_1} (2k_1^2 + k_1 U_{33}) \right) \\ &= 2k_1 + \text{Re}(U_{33})\end{aligned}$$